STEAM REFORMING OF METHANE ON A Ni CATALYST SUSPENDED IN MOLTEN SODIUM PHOSPHATES

Thesis by

Nicholas A. Kaffes

In Partial Fulfillment of the Requirements

for the Degree of

Doctor of Philosophy

California Institute of Technology

Pasadena, California

1982

(Submitted April, 1981)

Dedicated to my wife, Constance,

for her love and support.

ACKNOWLEDGEMENT

I would like to thank Professor George R. Gavalas for his guidance, advice and suggestions during the course of this work. I am also thankful to the California Institute of Technology and the Department of Energy for their financial support.

I would like to acknowledge the help of, and to thank, my colleagues Dr. Basil Iatrides, Mr. Mark Siddoway and Mr. Charunya Phichitkul.

Mr. George Griffith constructed most of the experimental equipment and his help and suggestions are greatly appreciated. Finally, I would like to thank Ms. Jan Sorenson for skillfully typing this thesis.

ABSTRACT

A molten salt bath was used to carry out the methane steam reforming reaction in the 800-1000^{o}C range. The rate of methane pyrolysis was also determined under the same conditions to compare it to the rate of steam reforming. The molten salt baths used included a eutectic mixture of sodium pyrophosphate and sodium metaphosphate, a eutectic mixture of potassium pyrophosphate and potassium metaphosphate, a mixture of Na_2O, P_2O_5 and V_2O_5 and a mixture of Na_2O, P_2O_5 and NiO. Additional experiments were conducted in empty reactors.

It was found that the rate of pyrolysis was not affected by any of the salt systems.The rate of the steam reforming reaction was low, about 10% of the pyrolysis rate, for the empty reactors and for all the salt systems except the system Na_2O-P_2O_5-NiO under reducing conditions. Under reducing conditions, the nickel of this system was reduced to metallic Ni which catalyzed the CH_4-H_2O reaction.

X-ray diffraction, electron microscope and electron microprobe analysis studies confirmed the hypothesis that under oxidizing conditions nickel was dissolved in the melt and under reducing conditions solid nickel particles were formed which were suspended in the melt. These particles were exposed to the reactant gases on bubble surfaces.

This novel catalytic steam reforming system is especially suitable for handling residual oils of high sulfur and heavy metal content. The sulfur is captured by the salt melt whereas

the nickel catalyst is regenerated by repeated cycles of dissolution into and reduction from the melt.

TABLE OF CONTENTS

TABLE OF CONTENTS (Cont.)

TABLE OF CONTENTS (Cont.)

CHAPTER ONE

INTRODUCTION

SECTION 1.1: GENERAL

Carbonaceous materials provide the major source of energy in the world today as well as the basis for the manufacture of a great variety of products. The gradual decrease in the availability of more preferred kinds of such materials, like natural gas and high quality crude oil, has led to a world-wide research and development effort to make possible the more extensive use of less preferred materials, such as coal, shale oil, residual oils and heavy crudes. Most of the latter materials are plentiful, but have some undesirable properties when used as fuels or raw materials. They are, in general, more difficult to handle and more harmful to the environment.

Extensive research and development is currently addressed to improving the handling properties of these materials and controlling sulfur and other emissions. One approach pursued is the conversion of dirty fuels to products similar to natural gas or light petroleum fractions. Coal gasification has been used in the past in the production of water gas, producer gas, etc. In the newer processes, modern contacting methods (e.g. fluidization) and catalysts are employed to increase efficiency and to yield gases with high heating value or gases suitable for the synthesis of ammonia or methanol.

Atmospheric and vacuum residual oils are polluting fuels and current treatment methods are expensive. Non-catalytic partial oxidation, like the Texaco or Shell processes, is an alternative to costlier treatments. Partial oxidation leads to $CO-H_2$ synthesis gas mixtures or to hydrogen gas for hydrotreating.

New steam reforming catalysts could also be used to obtain synthesis gas from residual oil.

In addition to other types of reactors, the fuel conversions mentioned above can be performed in a molten salt bath. The bath is used to suspend the reactants and as a heat transfer medium. Furthermore, if the salt constituents are properly selected, the melt bath can catalyze the conversion reactions.

The present thesis examines the molten sodium phosphate bath as a medium for fuel conversion reactions. Nickel was added to this bath to catalyze the reactions. The reaction rates obtained under different conditions were related to the different solid and molten phases present in the reactor during the experiments.

SECTION 1.2: COAL GASIFICATION

Coal gasification involves the conversion of coal to fuel gases such as CO, H_2 and CH_4. This is accomplished by pyrolyzing coal and by further reacting it with O_2, H_2O, CO_2, or H_2. The transformations involved can be written in the form of the chemical reactions:

$$\text{Coal} \xrightarrow{(500^{\circ}-700^{\circ})} H_2,\ CO,\ CO_2,\ CH_4,\ H_2O,\ H_2S,\ldots,\text{tar, char} \qquad (1.2.1)$$

$$C(\text{graphite})+\tfrac{1}{2}O_2(g)\rightarrow CO(g),\quad \Delta H^{\circ}_{298.15^{\circ}K}= -26.42 \text{ kcal/mol}$$
$$\Delta G^{\circ}_{1000^{\circ}K} = -47.859 \text{ kcal/mol}$$
(JANAF, 1971) (1.2.2)

$$C(\text{graphite})+H_2O(g)\rightarrow CO(g)+H_2(g),\quad \Delta H^{\circ}_{298.15^{\circ}K}= +31.38 \text{ kcal/mol}$$
$$\Delta G^{\circ}_{1200^{\circ}K} = -8.678 \text{ kcal/mol} \qquad (1.2.3)$$

$$C(\text{graphite})+CO_2(g)\rightarrow 2CO(g),\quad \Delta H^{\circ}_{298.15^{\circ}K}= +41.21 \text{ kcal/mol}$$
$$\Delta G^{\circ}_{1200^{\circ}K}= -9.42 \text{ kcal/mol} \qquad (1.2.4)$$

$$C(\text{graphite})+2H_2(g)\rightarrow CH_4(g),\quad \Delta H^{\circ}_{298.15^{\circ}K}= -17.895 \text{ kcal/mol}$$
$$\Delta G^{\circ}_{1200^{\circ}K}= 9.887 \text{ kcal/mol} \qquad (1.2.5)$$

Since some of the above reactions are endothermic at process temperatures, part of the coal is combusted to provide the necessary heat:

$$C(\text{graphite})+O_2(g)\rightarrow CO_2(g),\quad \Delta H^{\circ}_{298.15^{\circ}K}= -94.054 \text{ kcal/mol}$$
$$\Delta G^{\circ}_{1000^{\circ}K}= -94.628 \text{ kcal/mol} \qquad (1.2.6)$$

Reactions (1.2.3) and (1.2.4) are favored by higher temperatures and lower pressures, whereas reaction (1.2.5) is favored by lower temperatures and higher pressures. These opposing requirements have to be balanced in any given process. Moreover, these three reactions are slow in the absence of appropriate catalysts. Because coal is a solid reactant, containing many catalyst poisons, catalysis in gasification is a difficult task. The initial gas products of gasification can undergo further reaction, either in the gasifier or in downstream reactors. The water-gas shift reaction,

$$CO(g)+H_2O(g)\rightleftarrows CO_2(g)+H_2(g),\quad \Delta H^{o}_{298.15^{o}K}= -9.839 \text{ kcal/mol}$$
$$\Delta G^{o}_{1000^{o}K}= -0.729 \text{ kcal/mol} \qquad (1.2.7)$$

is easily catalyzed by Fe_2O_3 (Taylor, 1921) and can proceed in the gasifier or downstream to achieve the desired CO : H_2 ratio. Since CH_4 is a valuable constituent because of its high heating value, (1013 BTU/scf), methanation is also carried out. It takes place in a separate reactor to avoid poisoning the Ni catalyst:

$$CO(g)+3H_2(g)\rightarrow CH_4(g)+H_2O(g),\quad \Delta H^{o}_{298.15^{o}K}= -49.276 \text{ kcal/mol}$$
$$\Delta G^{o}_{800^{o}K}= -5.567 \text{ kcal/mol} \qquad (1.2.8)$$

If air is used in coal-oxygen gasification, the product has a heating value of about 150 BTU/scf and is referred to as low-BTU gas. If oxygen only is used, a medium-BTU gas (about 300 BTU/scf) is obtained because the product is not diluted by atmospheric nitrogen; of course, there is the added cost of an oxygen

plant. With methanation (reaction 1.2.8), a gasification product can reach a heating value of 900-1000 BTU/scf. Low- and medium-BTU gases are not economically suitable for transportation over long distances but they are rather intended for local use by industry. A high-BTU gas, however, can serve as synthetic or substitute natural gas (SNG).

Sulfur removal is accomplished either in the gasifier or by stripping the product gas downstream. Diethanolamine (DEA) can be used as the absorbing liquid for H_2S as well as for CO_2. Most processes complete sulfur removal with a Claus plant.

A process involving fluidization and using catalysis to promote coal-steam gasification and gas phase methanation is the Exxon Catalytic Coal Gasification (CCG)process (Eakman, 1980). This process utilizes an alkali metal catalyst, K_2CO_3(Nahas, 1978). Coal is gasified with steam in a fluid bed gasifier at a relatively low temperature (770^{o}C) and moderate pressure (35 atm). The product CH_4 is cryogenically separated from CO and H_2 which are recycled to the gasifier. The K_2CO_3 catalyst is recovered from the ash/char residue from the gasifier by water leaching. The recovered catalyst solution, supplemented by needed makeup catalyst, is used to impregnate fresh coal. At reactor temperatures, this catalytic salt is a solid (m.p. of K_2CO_3 : 891^{o}C).

Coal gasification processes now in operation are the Lurgi and the Kopper-Totzek processes. Second generation processes are still in the development stage. Although large pilot plants

are currently in operation, no commercial applications exist in the U.S. This suggests the need for improved gasification technology.

SECTION 1.3: STEAM REFORMING OF HYDROCARBONS (METHANE, LIGHT HCs, RESIDUAL OIL)

When hydrocarbons and steam are contacted at high temperature (>500°C), lighter gases are produced:

$$C_xH_y + xH_2O \rightarrow xCO + (y/2+x)\ H_2 \qquad (1.3.1)$$

This fundamental reaction is accompanied by the water-gas shift reaction (1.2.7), and the methanation reaction (1.2.8). Additionally, coking on reactor walls or catalyst surfaces is possible:

$$C_xH_y \rightarrow xC + y/2\ H_2 \qquad (1.3.2)$$

$$2CO \rightleftarrows CO_2 + C \qquad (1.3.3)$$

$$CO + H_2 \rightleftarrows C + H_2O \qquad (1.3.4)$$

Reactions (1.3.3) and (1.3.4) are the reverse of the Boudouard reaction (1.2.4) and the carbon-steam reaction (1.2.3), respectively. Supported Ni catalysts are the most effective in carrying out reaction (1.3.1) (Rostrup-Nielsen, 1975).

Operating conditions depend on the desired product composition. The useful product gas constituents, H_2, CO, and CH_4, can be used in ammonia and methanol synthesis, in hydrotreating or as substitute natural gas. High temperatures and low pressures favor CO and H_2, while low temperatures and high pressures favor CH_4, as in coal gasification.

In addition to the reactions listed above, many others occur simultaneously, such as hydrocarbon cracking, polymerization, hydrocracking (hydrogenolysis), dehydrogenation, etc. Many take place on the catalyst surface adding to, or depleting, the carbonaceous deposits on the catalyst. Therefore, it is import-

ant to consider such reactions along with the simpler coking reactions (1.3.2), (1.3.3), (1.3.4) in order to avoid excessive coking and subsequent catalyst deactivation. Coking is usually controlled by setting the steam to carbon ratio high enough to reverse reaction (1.3.4).

Feed streams containing sulfur compounds have a poisoning effect on the catalyst. Other poisons are nitrogen compounds and metals (Ni and V) found in heavier crude fractions. Catalysts deactivated by sulfur poisoning (H_2S adsorption) can be regenerated by flow of steam or a steam-hydrogen mixture at operating temperatures (Rostrup-Nielsen, 1975).

Among various petroleum fuels, atmospheric and vaccum residual oils are the least attractive on account of their high sulfur and heavy metal content. The direct combustion of residual oil in utility boilers in most cases requires sulfur removal before or after combustion. Catalytic hydrodesulfurization, essentially the only commercial process for sulfur removal before combustion, is expensive, not only because of high pressure and hydrogen consumption, but also because of catalyst deactivation by deposition of nickel and vanadium contained in the fuel.

The conversion to synthesis gas for ammonia or methanol production is an alternative use of residual oil. The conventional nickel catalyst used in steam reforming of methane and naphtha is unsuitable because of rapid deactivation by sulfur poisoning and coke deposition. Certain more rugged catalysts are being developed in Japan for reforming residual oils as well as lighter feedstocks (EPRI, 1977).

Non-catalytic processes that are available commercially for the conversion of residual oil are the Texaco and Shell partial oxidation processes. In the production of synthesis gas for ammonia or methanol, the partial oxidation is conducted with oxygen and the required oxygen plant increases capital costs. When the partial oxidation is conducted with air, a low-BTU gas is produced suitable as a fuel for base-load electricity generation and, in fact, the Texaco coal gasifier is considered one of the most viable low-BTU gas generators (EPRI, 1974).

New processes to steam-reform residual oils and other high sulfur hydrocarbon feeds need to be developed. Such processes should incorporate resistant catalysts and flexible feed specifications.

SECTION 1.4: USE OF MOLTEN SALTS IN COAL GASIFICATION AND STEAM REFORMING REACTIONS

Molten salts have been utilized in the past as heat transfer media and catalysts. The first application is based on their high thermal conductivity and the stability of some salts at high temperatures. The catalytic applications of molten salts, which have been reviewed by Kenney (1975), include molten Lewis acids $ZnCl_2$ and $AlCl_2$ as catalysts for hydrocarbon isomerization and cracking, $CuCl_2$ for chlorination and oxychlorination, and $V_2O_5 + K_2SO_4$ for SO_2 to SO_3 conversion. While in the last case, the catalytic melt is supported on a porous inert solid, in other cases, the molten catalyst is a free liquid. The fluid nature of the catalyst provides good heat transfer properties and allows continuous regeneration. These advantages are diminished by the small interfacial area between the reacting fluid and the catalyst (especially in the case of an unsupported liquid catalyst) and by the corrosive nature of most molten salts.

Molten salts have also been studied as media for coal liquefaction (Green, 1980) and gasification. M. W. Kellogg Co. have developed a process for coal gasification in a molten carbonate bath (Le Francois, 1967; Cover, 1973), Fig. 1.4.1. The molten alkali carbonate catalyzes the steam-char reaction in accord with the well-known catalytic behavior of alkali metal and alkaline earth carbonates and oxides (Taylor, 1921; Blayden, 1943; Walker, 1968; Wilks, 1974; Johnson, 1976). The coal or char suspended in the melt recirculates between two vessels; in the first vessel the carbonaceous matter is gasified with steam,

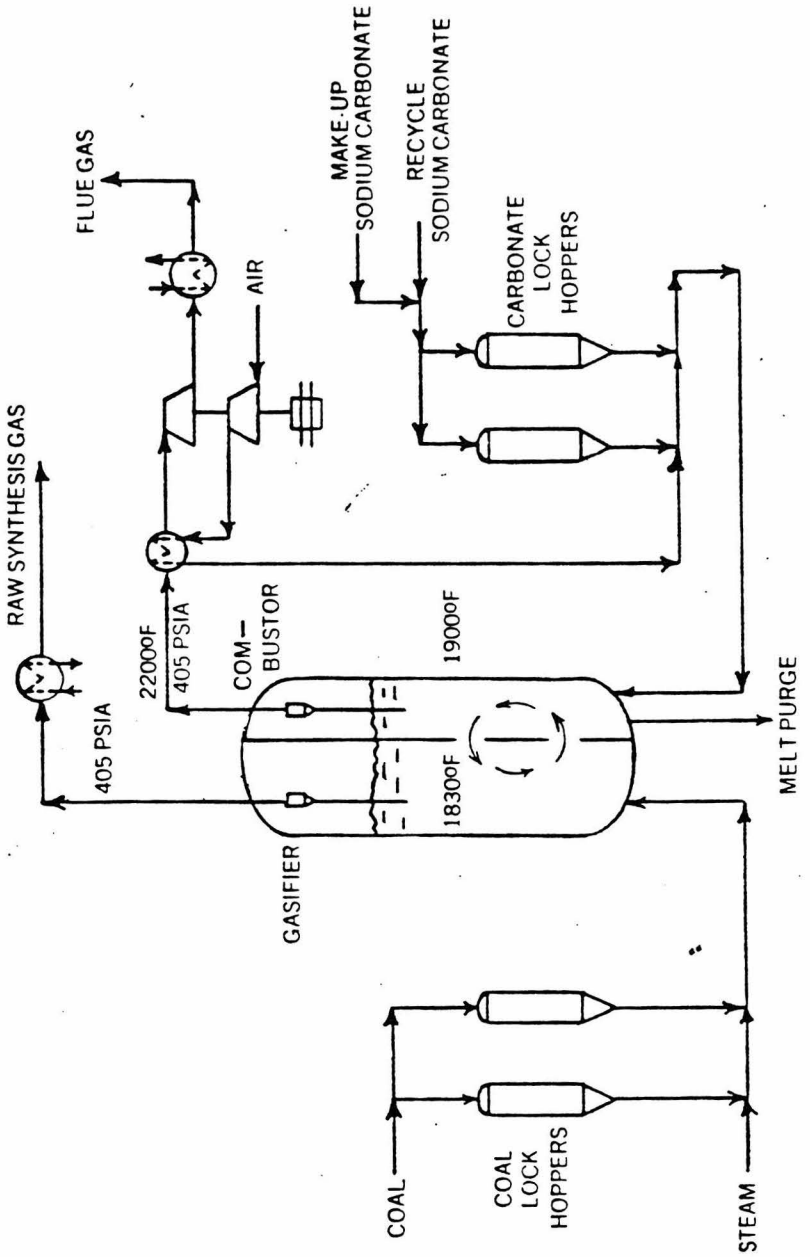

FIG. 1.4.1: KELLOGG MOLTEN SALT PROCESS

(Cover, 1973)

and in the second it is burned with air. A thermal balance is thus achieved between the exothermic combustion reactions and the endothermic gasification reactions while keeping the product gases separate. This allows the use of air rather than oxygen in the production of high-BTU gas. A side stream of salt is withdrawn and purified of the accumulating coal ash components by solution in water and filtration. The filtrate is subsequently carbonated to precipitate sodium bicarbonate which is calcined and returned to the reactor. In addition to the use of air rather than oxygen, the process has the advantage of handling coking coals without prior treatment. The disadvantages of the process are due to the corrosiveness of the molten carbonate, necessitating the use of high purity alumina reactor vessels, and the additional process steps involved in melt purification. Another disadvantage is inherent in the reversible hydrolytic reaction:

$$Na_2CO_3(l)+H_2O(g)\rightleftarrows 2NaOH(l)+CO_2(g) \quad \Delta G^{o}_{1200^{o}K} = -17.276 \text{kcal/mol} \qquad (1.4.1)$$

The reaction proceeds in the forward direction in the gasifier vessel and in the reverse direction in the combustor where the CO_2 pressure is higher. As a result, a certain amount of CO_2 is transferred from the combustor to the gasifier, diluting the product fuel gas and partly offsetting the advantage of the two-vessel system. The production of NaOH in the gasifier is also disadvantageous because of the volatility of this compound at reaction temperatures. A later version of the Kellogg pro-

ess abandoned the two-vessel concept and combined the steam-char and oxygen-char reactions in a single vessel.

More recently, the Atomics International Division of Rockwell International has been developing,under contract with the U.S. Department of Energy, a molten carbonate coal gasification process using a single reactor vessel (Trilling, 1977). The process temperature and pressure are similar to those of the Kellogg process. A great deal of attention is paid to the salt purification stage where coal ash and sulfur compounds are removed. The product gases from the main reactor have been reported to be essentially sulfur-free. The Atomics International program included bench-scale and pilot plant studies (Kohl, 1978). Recently, Rockwell has completed runs of their process development unit at 2000 lbs. of coal per hour and 10 atm of pressure (Kohl, 1980).

The initial interest of the present study in molten salt media was directed at coal gasification with the idea of using a salt which is stable with respect to hydrolysis and, thus, revive the two-vessel concept. An extensive survey was undertaken to identify molten salts that meet the following requirements:

(i) sufficiently low melting point,

(ii) low volatility,

(iii) stability at high temperatures in the presence of O_2, H_2O, CO, CO_2, and

(iv) low cost and low toxicity.

The need to simultaneously satisfy these requirements eliminated almost all molten salts. For example, NaF-KF melts have low melting points, low volatility and are non-corrosive towards metals. However, in the presence of steam, they hydrolyze readily, producing HF and the corresponding hydroxides (see subsection 2.2.1). Sodium carbonate, which is used in the Kellogg and the Rockwell processes, satisfies the above specifications. While it does hydrolyze, the presence of CO_2 in the products ensures an equilibrium mixture of NaOH and Na_2CO_3, which is acceptable. Its melting point, 851°C, is somewhat high, but still lower than the usual gasification temperature and the use of a eutectic Na_2CO_3-K_2CO_3 composition can bring it still lower.

Another salt that was found to be promising is (non-stoichiometric) sodium phosphate ($xNa_2O \cdot yP_2O_5$). Molten sodium phosphates have been proposed as media for the thermal cracking of petroleum fractions to olefins and for the gasification of carbonaceous materials (Dugan, 1974). They have several attractive properties: they are nonvolatile and have a low melting point of 552°C at a eutectic composition of 56% Na_2O and 44% P_2O_5 (molar). The melt is a mixture of phosphate chains and sodium ions acting as flux (Van Wazer, 1958). The degree of phosphate chain polymerization is low at this composition (about seven P atoms per molecule) and the viscosity is about 100 centipoises at 900°C. Under steam pressure, the phosphate chains are cleaved and incorporate water as hydroxyl groups:

$$\begin{array}{c} \overline{O} \quad \overline{O} \\ \ldots\text{-O-P-O-P-O-}\ldots \\ \underline{O} \quad \underline{O} \end{array} + H_2O \rightleftarrows \ldots\text{-O-P-OH} + \text{HO-P-O-}\ldots \qquad (1.4.2)$$

This is a useful feature because the hydroxyl groups could contribute to the gasification reactions. A disadvantage in the use of the phosphate melt is difficulty in salt purification. When the phosphate melt is cooled, an essentially insoluble, dehydrated glassy material is obtained. By cooling the phosphate melt in the presence of steam, the resulting solid has a reasonable solubility. Nevertheless, the purification of the phosphate is tedious and costly in terms of an industrial process. However, molten phosphates would be an attractive gasification media for fuels which are essentially free of mineral matter. Such materials as residual oil could be treated in this salt system. Dugan (1974) proposed a two-vessel process for the pyrolysis and gasification of heavy petroleum fractions suspended in molten alkali or alkaline earth phosphates. The first vessel is a cracker where the salt serves as the heat carrier. The lighter cracking products are removed overhead while extensive coking takes place in the phosphate bed. The bed tends to suspend these carbonaceous deposits and a stream of salt with suspended coke is fed to the second vessel. There an oxidizing gas (air/O_2, H_2O, or CO_2) gasifies the carbonaceous matter producing a mixture of CO, H_2, CH_4, CO_2, etc., and regenerating the melt. The alkali or alkaline earth metal serves as the catalyst in this gasification step. Regenerated melt is led back to the cracking reactor. Sulfur compounds and Ni and V from trace organometallic compounds dissolve in the melt.

A bleed stream of melt is taken through a purification process to remove these contaminants and to recover the salt.

This study was addressed to sodium phosphate melt as a system for the pyrolysis and steam reforming of carbonaceous materials. The results could find use in the major commercial molten salt developments, e.g. Rockwell's, and could be adapted to either a one- or a two-vessel process. The characteristics of this medium were investigated with respect to methane pyrolysis and steam reforming. Pyrolysis was not studied in detail but as an integral part of high temperature steam reforming. In addition to the plain phosphate melt, a melt containing nickel was studied as a medium for the steam-methane reaction. Under reducing conditions, the nickel in metallic form is suspended in the melt and catalyzes the reforming reaction. Such a reactor is well suited to handle feeds like residual oils which are prone to coking and cannot be used with the customary supported nickel catalyst.

CHAPTER TWO

PROPERTIES OF MOLTEN SODIUM PHOSPHATES AS GASIFICATION MEDIA

SECTION 2.1: PROPERTIES OF THE Na_2O-P_2O_5 SYSTEM

Phosphate salts ($mM_2O \cdot nP_2O_5$, M=metal or H) occur in many different compositions because of the possibility of condensation:

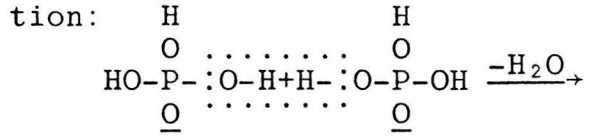

(orthophosphoric acid, H_3PO_4)

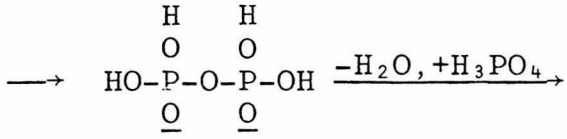

(pyrophosphoric acid, $H_4P_2O_7$)

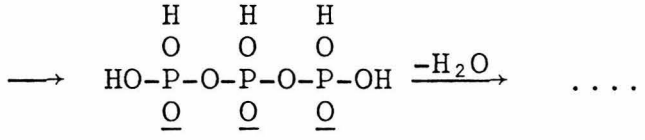

(tripolyphosphoric acid, $H_5P_3O_{10}$)

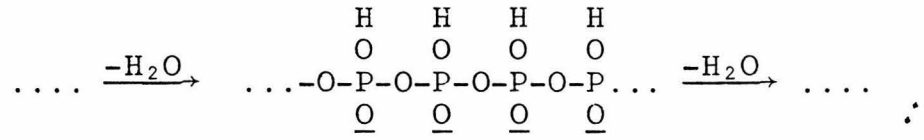

(metaphosphoric acid, $(HPO_3)n$)

.... $\xrightarrow{-H_2O}$ $(P_4O_{10})_n$

(phosphorus pentoxide) (2.1.1)

The heat of reaction for every H_2O elimination is about $\Delta H = +7$ kcal/mol (Nebergall, 1968). The composition $mM_2O \cdot nP_2O_5$ with $m/n = 3$ is called the orthophosphate, $m/n = 2$ is the pyrophosphate and $m/n = 1$ is the metaphosphate. The region $1<m/n<2$ is the so-called polyphosphate region and the region $m/n<1$ is called the ultraphosphate region.

The phosphate chain of equation (2.1.1) resembles hydrocarbon chains. The PO_4 units form tetrahedra with P at the center bonded to O atoms at the corners with sp^3 hybridization bonds. The similarity extends to the fact that cyclic phosphate compounds also occur:

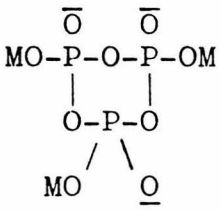

(Trimetaphosphate ring) (2.1.2)

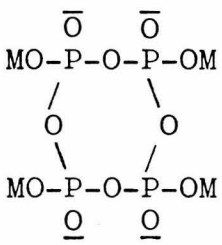

(Tetrametaphosphate ring) (2.1.3)

Another possibility is branched and, ultimately, cross-linked phosphate networks. Among the alkali phosphates, the orthophosphate M_3PO_4 (or $3M_2O \cdot P_2O_5$) and the pyrophosphate $M_4P_2O_7$ (or $2M_2O \cdot P_2O_5$) are crystalline compounds. The polyphosphates can also be obtained crystalline, constituting the series tripolyphosphate ($5M_2O \cdot 3P_2O_5$), tetrapolyphosphate, pentapolyphosphate, etc. The limiting member of this series of long, straight-chain phosphates is the metaphosphate, $(MPO_3)_n$, or $M_2O \cdot P_2O_5$, which can be obtained in a variety of crystalline modifications: Kurrol's salt, Maddrell's salt. The cyclic trimetaphosphate and tetrametaphosphate are also crystalline. However, rapid cooling of polyphosphate melts with $m/n<1.67$ leads

to glass formation. The glass of the metaphosphate composition, e.g. $(NaPO_3)_n$, is known as Graham's salt. Ultraphosphates, too, can form either glasses or crystalline solids. Solid P_4O_{10} can exist as a crystal composed of cross-linked phosphate plates.

The reverse of condensation, hydrolysis, is exothermic:

$$\begin{array}{l} \quad\quad M \quad M \\ \quad\quad O \quad O \\ ...\text{-}O\text{-}P\text{-}O\text{-}P\text{-}O\text{-}... + H_2O \longrightarrow \\ \quad\quad \underline{O} \quad \underline{O} \\ \quad\quad M \qquad\quad M \\ \quad\quad O \qquad\quad O \\ \longrightarrow \quad ...\text{-}O\text{-}P\text{-}O\text{-}H + H\text{-}O\text{-}P\text{-}O\text{-}... \\ \quad\quad \underline{O} \qquad\quad \underline{O} \end{array} \qquad (2.1.4)$$

The activation energy of hydrolysis is in the range of 20-40 kcal/mol (Van Wazer, 1958), depending on the environment. Factors such as acidic pH, enzymes (phosphatases), colloidal gels, etc. catalyze the reaction.

The crystalline salts up to the polyphosphate range are easily soluble in water. So are the cyclic trimeta- and tetrametaphosphates. On the other hand, the crystalline long-chain phosphates close to the metaphosphate range are less soluble.

Fig. 2.1.1 is a phase diagram of the system Na_2O-P_2O_5 for $1 \leq m/n \leq 2$. Three crystalline compositions are possible; pyrophosphate, $2Na_2O \cdot P_2O_5$; tripolyphosphate, $5Na_2O \cdot 3P_2O_5$; and metaphosphate, $Na_2O \cdot P_2O_5$. There is a eutectic at $m/n=1.28$ and 552^oC. If potassium is added to the system, still lower liquidus temperatures are possible.

Phosphates in the range $1 \leq m/n \leq 2$ are linear polymers. The degree of polymerization, $\bar{p}$, which is equal to the average number of P atoms in a chain is given by:

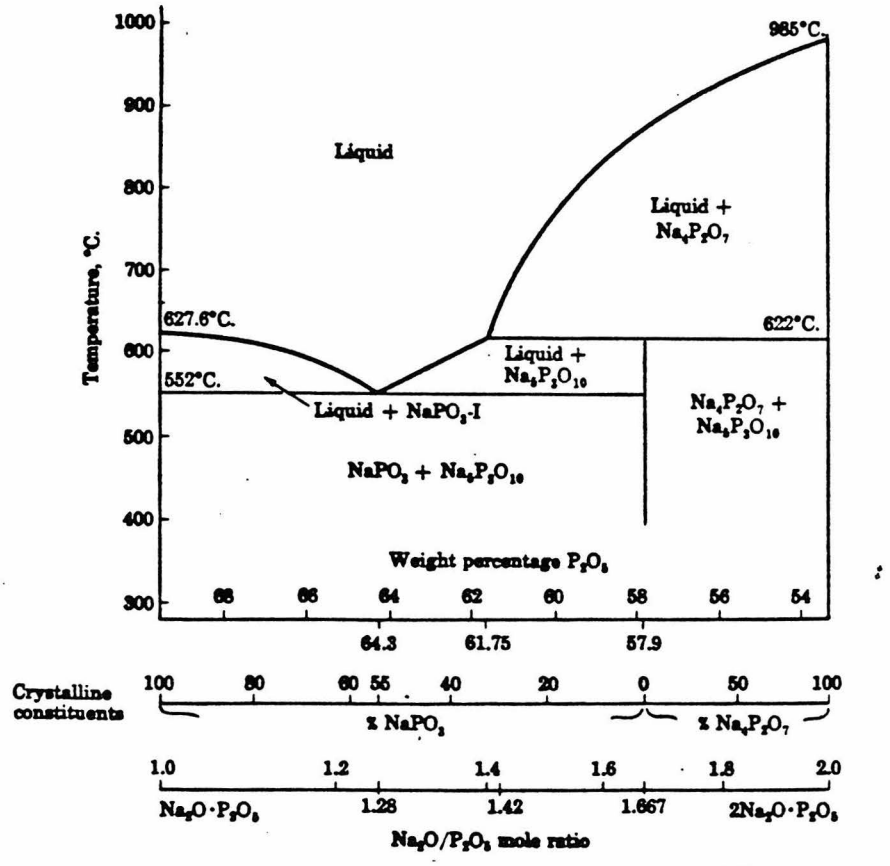

FIG. 2.1.1: THE SODIUM PHOSPHATE PHASE DIAGRAM BETWEEN $Na_2O \cdot P_2O_5$ AND $2Na_2O \cdot P_2O_5$ (Van Wazer, 1958)

$$\bar{p} = \frac{2}{m/n-1} \qquad (2.1.5)$$

At the pyrophosphate composition, m/n=2, and $\bar{p}$=2. As m/n→1, p→∞. At the eutectic composition, m/n=1.28, $\bar{p}$ is 7.14. This degree of polymerization is preserved in both the liquid and the solid (crystalline or amorphous) states. Absorption of water by a polyphosphate decreases $\bar{p}$ by increasing m/n:

$$m/n = \frac{M_2O+H_2O}{P_2O_5} \qquad (2.1.6)$$

In the molten state, the sodium phosphates exhibit Newtonian flow (Van Wazer, 1958). Their viscosity can be calculated from:

$$\mu = a_\mu \exp\left[E/RT\right] \quad \text{poise} \qquad (2.1.7)$$

where

$$a_\mu = 0.0298(m/n)^2 - 0.0522(m/n) + 0.0240 \quad \text{poise} \qquad (2.1.8)$$

and

$$\log_{10}E = -0.515(m/n) + 4.722 \qquad (2.1.9)$$

These are valid for 1<m/n<2. Over this range of compositions and for temperatures from 600° to 1000°C, the viscosity varies from 10 to 100 centipoises. At 900°C and m/n=1.28, the viscosity is 86 cp.

The density of the melt can be determined from (Van Wazer, 1958):

$$d = 2.372 + 0.089(m/n) - 0.000388t(^{\circ}C), \ g/cm^3 \qquad (2.1.10)$$

and its surface tension from:

$$\gamma = 150.6 - 0.0379t(^{\circ}C) + 67.7(m/n), \ dyne/cm \qquad (2.1.11)$$

SECTION 2.2: SODIUM PHOSPHATES IN GASIFICATION

The molten salts used in previous gasification studies were the alkali metal carbonates, especially Na_2CO_3 (Le Francois, 1967; Trilling, 1977). Dugan (1973) proposed the use of alkali metal or alkaline earth phosphates ranging from the metaphosphate to the orthophosphate composition as gasification media.

W.-Y. Wen (1980) reviewed proposed mechanisms of alkali metal catalysis in the gasification of coal, char or graphite. The activation energy of the graphite-steam reaction is reduced from up to 88 kcal/mol in the uncatalyzed reaction to 37 kcal/mol in the reaction catalyzed by 1 wt % of Li_2CO_3, the most active alkali carbonate (McKee, 1978). It seems that the alkali salt is reduced by carbon and the resulting alkali metal is finally oxidized by steam. In the case of K_2CO_3:

$$K_2CO_3(l) + 2C\ (s) \rightleftarrows 2K\ (g) + 3CO\ (g) \qquad (2.2.1)$$

$$2K\ (g) + 2nC\ (s) \rightleftarrows 2C_nK\ (s) \qquad (2.2.2)$$

$$2C_nK(s)+2H_2O(g)\rightleftarrows 2nC(s)+2KOH(l)+H_2(g) \qquad (2.2.3)$$

$$2KOH(l)+CO(g)\rightleftarrows K_2CO_3(l)+H_2(g) \qquad (2.2.4)$$

$$C(s) + H_2O\ (g) \rightleftarrows CO\ (g) + H_2\ (g) \qquad (2.2.5)$$

The species C_nK is a carbon-potassium compound(intercalate) with good electron donor ability. Reaction (2.2.1) has a high Gibb's free energy, $\Delta G^{o}_{1000^{o}K}$ = +61 kcal/mol and is considered to be the rate-determining step.

It has been found that alkali halides do not have catalytic properties (Veraa, 1976); the gasification reaction proceeds as in the uncatalyzed case. It is also known that P_2O_5 and boric

acid and its derivatives (McKee, 1981) inhibit gasification. Dugan (1973) found that the gasification rate for salts with high M_2O/P_2O_5 ratio was higher than for salts with low M_2O/P_2O_5 ratio. This is consistent with the expected catalytic effect of alkalis and the inhibitory effect of P_2O_5. A further enhancement of the gasification rate was obtained by treating the melt with CO_2. The melt absorbed some CO_2 to form carbonates at which point mechanism (2.2.1) to (2.2.4) could proceed. In the absence of any other source of carbonate, the carbonaceous matter is a source, producing CO_2 in the course of the reaction. Therefore, melt composition and reaction rate depend on p_{CO_2}.

2.2.1 Hydrolysis of Molten Salts

In steam gasification in molten salts, salt hydrolysis is an important consideration:

$$Na_2CO_3(l)+H_2O(g)\rightleftarrows 2NaOH(l)+CO_2(g) \qquad (1.4.1)$$

Hydrolysis forms NaOH which has a low but finite volatility resulting in salt losses and harmful emissions. In the case of reaction (1.4.1), a high p_{CO_2} is necessary to limit the extent of hydrolysis. Table 2.2.1 presents the hydrolysis equilibrium constants, K_h, for alkali carbonates and alkali halides. Hydrolysis is more extensive for the carbonates and, in general, decreases with increasing alkali metal or halogen atomic weight. In all cases, the extent of hydrolysis increases with temperature.

In the presence of steam and carbon dioxide, the composition

TABLE 2.2.1

HYDROLYSIS EQUILIBRIUM CONSTANT FOR DIFFERENT SALTS

Salt	$\log_{10} K_h$:	1000°K	1200°K	1400°K
Li_2CO_3		-3.009	-2.145	-1.526
LiF		-5.124	-4.053	-3.382
LiCl		-4.441	-3.731	-3.206
LiBr		-4.595	-3.887	-3.366
Na_2CO_3		-4.306	-3.146	-2.334
NaF		-5.387	-4.127	-3.349
NaCl		-6.611	-5.467	-4.654
NaBr		-7.189	-5.949	-5.071
K_2CO_3		-4.468	-3.055	-2.084
KF		-5.049	-3.893	-3.182
KCl		-7.776	-6.315	-5.314
KBr		-8.547	-7.013	-5.921

of a phosphate melt is determined by the equilibrium of the reactions:

$$2NaPO_3(l)+H_2O(g)\rightleftarrows 2NaOH(l)+P_2O_5(g) \qquad (2.2.6)$$

$$2NaPO_3(l)+CO_2(g)\rightleftarrows Na_2CO_3(l)+P_2O_5(g) \qquad (2.2.7)$$

$NaPO_3$ is chosen as a representative compound of the melt. Unfortunately, high temperature thermodynamic properties of phosphates are available only for magnesium orthophosphate, $Mg_3(PO_4)_2$. In this case, a comparison can be made of the relative equilibria of the reactions:

$$Mg_3(PO_4)_2(s)+3H_2O(g)\rightleftarrows 3Mg(OH)_2(s)+P_2O_5(g) \qquad (2.2.8)$$

$$MgCO_3(s)+H_2O(g)\rightleftarrows Mg(OH)_2(s)+CO_2(g) \qquad (2.2.9)$$

$$Mg_3(PO_4)_2+3CO_2(g)\rightleftarrows 3MgCO_3(s)+P_2O_5(s) \qquad (2.2.10)$$

Although $Mg(OH)_2$ is unstable above 350^oC, its thermodynamic properties are defined and can be used for comparison purposes. The Gibb's free energies of reactions (2.2.8), (2.2.9) and (2.2.10) are shown in Table 2.2.2. Taking as a basis p_{H_2O} = 1 atm and T = 1300^oK, the equilibrium of reaction (2.2.8) would give a negligible $p_{P_2O_5}$ ($<10^{-10}$ atm), while reaction (2.2.9) would produce p_{CO_2} = 190 atm! Under the same conditions, reaction (1.4.1) provides $p_{CO_2} = 3 \times 10^{-3}$ atm; hence, it is expected that the equilibrium $p_{P_2O_5}$ for reaction (2.2.6) would be negligible. In general, the alkaline earth carbonate salts hydrolyze to a larger extent than the alkali metal carbonates and, in turn, the alkali metal carbonates hydrolyze to a larger extent than the alkali metal halides or phosphates. Experimentally, it is known (Van Wazer, 1958) that sodium phosphate glasses can be made from NaCl and H_3PO_4 if steam is blown through the melt to

TABLE 2.2.2

T, ^{o}K	ΔG^{o} of Reaction (cal/mol)	(2.2.9)	(2.2.10)	(2.2.11)
298		92,659	6,856	29,133
1000		148,144	2,271	20,451
1300		138,300	-13,600	15,064

remove residual chloride as HCl; evidently, after NaCl hydrolyzes, the resulting $mNa_2O \cdot nP_2O_5$ melt is stable to further hydrolysis. The equilibrium of reaction (2.2.10) at 1300^oK yields $p_{P_2O_5}/p^3_{CO_2} = 2.9 \times 10^{-3}$. For example, when p_{CO_2}=0.2 atm, $p_{P_2O_5} = 2.3 \times 10^{-5}$atm.

The above calculations suggest that sodium polyphosphate glasses ($1 \leq m/n \leq 1.67$) do not hydrolyze appreciably. However, it is known that sodium ultraphosphate glasses with $m/n < 0.9$ exhibit appreciably high pressures of P_2O_5, as well as a tendency to absorb water while molten. The weak hydrolysis of sodium polyphosphates is advantageous in that it keeps the volatilization of P_2O_5at a minimum.

2.2.2 Experimental Considerations

A molten sodium phosphate gasifier can be operated with two vessels or compartments; the melt can be recirculated between the two compartments by a gas lift arrangement (Yoshida, 1973) without the need of mechanical pumps (Fig. 2.2.1). Residual oil or other carbonaceous matter (coal, char, petroleum black, etc.) can be treated with such an arrangement. In the case of residual oil suspended nickel particles could enhance the rate of steam reforming.

Molten phosphates are very good solvents for almost all metals, alloys, etc.; therefore they are very corrosive. Among metals, platinum can withstand this corrosive action. High quality alloys such as inconel can be used for a brief period. Among ceramics, zirconia offers the best protection, but some dissolution into the metal does occur. Porcelain crucibles are

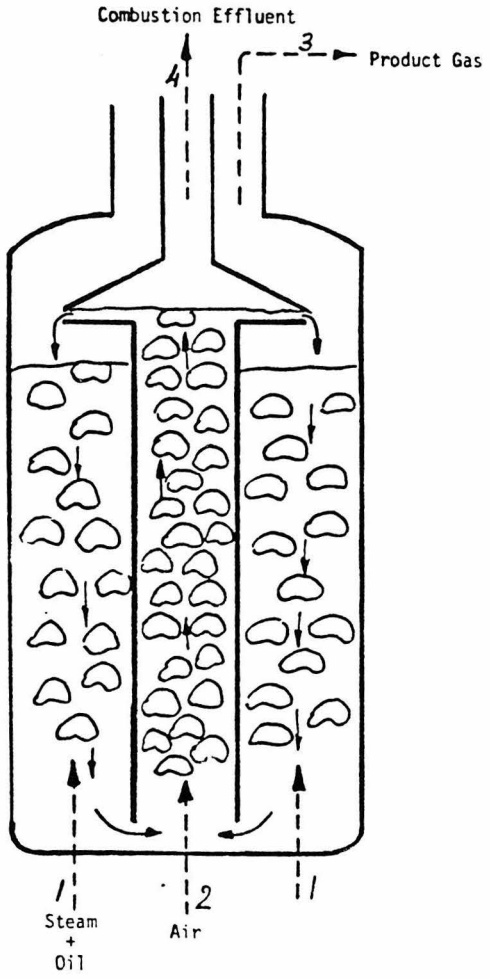

FIG. 2.2.1: A CONCEPTUAL COMMERCIAL PROCESS FOR GASIFICATION OF HYDROCARBONS IN MOLTEN PHOSPHATE.

also attacked. Alumina is soluble in sodium polyphosphates up to about 15 wt. % (Van Wazer, 1958). The best container for molten phosphates is a frozen lining of the salt itself. This is feasible for a thermally balanced process but is not convenient for small laboratory equipment. Another major operational difficulty is the thermal stress at the melting point where the salt volume changes by 10-20%. Cooling a container from a temperature above the melting point to room temperature often creates catastrophic stresses. A compromise between corrosion and cost of damaged reactors in laboratory studies is offered by the use of alumina crucibles.

In this study, experimental reactors were used to examine the behavior of a eutectic sodium phosphate melt for the pyrolysis and steam reforming of hydrocarbons. In a limited number of experiments, K_2O-P_2O_5 was used as the melt. In some experiments, nickel was added to the melt as a catalyst for the steam reforming reaction. A few experiments were carried out with V_2O_5 as an additive. Methane was chosen as a model hydrocarbon compound because of its simple structure and low reactivity. Ethylene was used as the reactant in a small number of experiments.

CHAPTER THREE

METHANE PYROLYSIS

SECTION 3.1: DESCRIPTION OF EXPERIMENTAL EQUIPMENT

3.1.0 General System Description

The study of methane pyrolysis in molten salt systems was carried out in the reactor flow system shown in Fig. 3.1.1.

The selected gas mixture was metered by Brooks flowmeters and heated in a preheating section consisting of Briskeat heating tapes and further brought to the reaction temperature by passing through the top section of the furnace. Several different reactor designs were employed as described in the next subsection. The furnace was a Hevi Duty Electric Co. model, Type 056-PT, 230V, 3400W, of maximum safe temperature of 1850^{o}F. The gas mixture entered the reactor as shown in the figure and left the reactor at a position near the top of the furnace. After flowing through a glass wool filter to remove entrained coke particles, solidified salt droplets and easily condensed hydrocarbon products, the gases passed through a water-cooled condenser. The gas line from the furnace exit to the condenser was kept at about 200^{o}C with the help of electric heating tapes. Steam condensate was collected at the bottom of the condenser while the gaseous products passed through a Drierite column to remove the water content corresponding to saturation conditions.

Gas chromatographs with thermal conductivity detectors (Loenco, Varian) were used to detect and analyze CH_4 and the major product, H_2. A gas chromatograph with a flame ionization detector (Hewlett-Packard) was used to determine the hydrocarbon products, C_2H_2, C_2H_4, and C_3 - C_5 hydrocarbons, as well as the reactant CH_4 and small amounts of $C_2H_6$and C_3H_8 derived from the

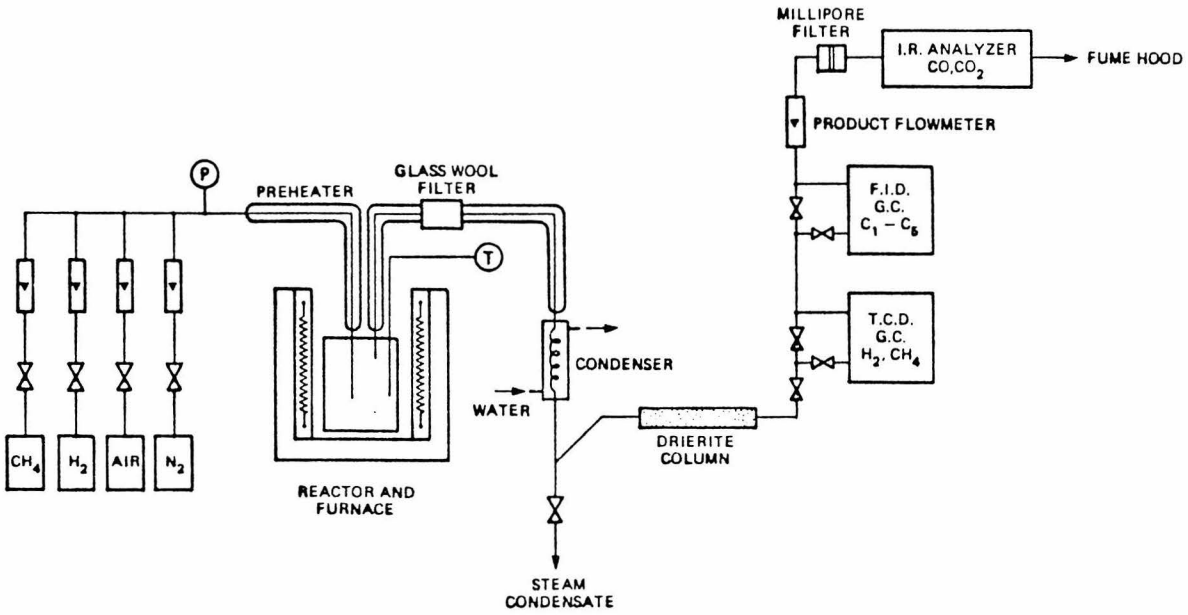

FIG. 3.1.1: REACTOR SYSTEM FOR METHANE PYROLYSIS

feed. The total product flowrate was measured by a Brooks flowmeter.

The gases leaving the condenser were then led through a Millipore filter to capture any remaining dust particles before entering the detector tube of an Infrared Industries non-dispersive IR analyzer. The analyzer continuously monitored the content of CO and CO_2 in the product gas; these two gases were obtained under reactor burn-off operation or in the methane-steam reforming studies described in the following chapters. When studying the steam reforming of methane, a steam-generator water flask was interposed between the gas mixing point and the preheater. This steam-generating system is described in detail in section 4.1.

3.1.1 Description of Reactors Used in Methane Pyrolysis

As discussed in the previous chapter, no readily available metal or alloy can withstand the corrosive action of molten sodium phosphates. Preliminary experiments with sodium phosphate melts (Kaffes, 1977) indicated that fused alumina crucibles (60-99 wt. % Al_2O_3) were able to withstand attack by the phosphate melt. After two to three hours at about 950°C, alumina crucibles containing the melt showed no visible corrosion of their 1/8" thick walls. On cooling, though, the crucibles tended to break with the freezing of the salt as a result of different thermal expansivities. Therefore, it was decided to use fused alumina tubes for containment but to reinforce them with an exterior wall of castable alumina. The castable alumina chosen for this purpose was Castolast G (a trademark of Harbison-Walker Refractories) with an analysis of 93.7 wt. % Al_2O_3, 5.6% CaO,

0.3% Fe_2O_3, 0.1% SiO_2. This material has a maximum service temperature of 3300°F (∿1800°C) and undergoes negligible permanent linear change (shrinking, etc.) after being fired to temperatures up to 1000°C. Castolast G is a blend of a tabular alumina aggregate and a high-strength, high-purity calcium aluminate cement. When properly cast, dried and fired, Castolast G exhibits a hardness comparable to that of a metal. Table 3.1.1 presents a list of properties of Castolast G.

The fused alumina parts used -- containment tubes and crucibles, gas inlet and outlet tubes, and thermocouple shields -- have ranged in alumina content from 60% Al_2O_3 for mullite ($2SiO_2 \cdot 3Al_2O_3$) MV-30 products to 99.8% Al_2O_3 for 998 products of McDanel Refractory Porcelain Company of Beaver Falls, Pennsylvania. Mullite, a refractory oxide material, proved satisfactory for one to two weeks continuous operation. However, chemical analyses of the salt after the runs by wet chemical analysis (Subsection 3.1.2), electron microprobe quantitative and qualitative elemental analysis (Section 5.2) showed considerable dissolution of the ceramic materials (e.g. Al_2O_3 and SiO_2) into the molten salt bath. The mechanical soundness of the reactors was not affected for the specified duration of the experimental runs. Table 3.1.2 presents a list of properties of MV-30 and Product 998. Although 998 is superior, MV-30 was satisfactory for all uses except as thermocouple protection tubes, the most sensitive parts, which were made of the higher quality 998 material.

Castolast G was used in the production of many cast items in order to gather experience about their mechanical behavior at

TABLE 3.1.1

PROPERTIES OF CASTOLAST® G, A HARBISON-WALKER

HIGH ALUMINA CASTABLE REFRACTORY

Source: Harbison-Walker Refractories (1977)

Max. Service Temperature, ^{o}F	3300
ASTM Class C-401	F
Approx. % by Wt. Water Added to Cast 100 lbs.	8-10
Lbs. Dry Mix Required/cu.ft.	163
Applications	Cast Trowelled Gunned
Bulk Density, lbs/cu.ft. After Drying at 230^{o}F	170
Modulus of Rupture (MOR), PSI After Drying at 230^{o}F	1700-2300
Hot MOR, PSI at 1500^{o}F	1880
Cold Crushing Strength, PSI After Drying at 230^{o}F	7000-12000
Permanent Linear Change, % After Drying at 230^{o}F	Negligible
Permanent Linear Change, % After Heating:	
at 1000^{o}F	Negligible
at 1500^{o}F	Negligible
at 3000^{o}F	0.0 to -0.2
at 3140^{o}F	0.0 to -0.5

Chemical Analysis (Wt. %)	Al_2O_3	SiO_2	Fe_2O_3	CaO
	93.7%	0.1%	0.3%	5.6%

TABLE 3.1.2

TYPICAL PHYSICAL PROPERTIES OF CERAMICS USED IN REACTOR ASSEMBLY

Source: McDanel Refractory Company (1979)

Product	MV-30	998
Composition	85% Mullite/15% Glass	99.8% Al_2O_3
Bulk Specific Gravity	2.8	3.85
Impenetrability	Gas Tight	Gas Tight
Flexural Strength	27,000psi	55,000psi
Compressive Strength	> 190,000psi	> 300,000psi
Tensile Strength	18,000psi	30,000psi
Hardness	7.5 Mohs	9.0 Mohs
Maximum Working Temp.	1750°C	1950°C
Max. Temp. Supported Tube	1700°C	1900°C
Likely Sag Temp., Unsupported Tube	1600°C	1750°C
Thermal Conductivity ($BTU/ft^2/hr/°F/inch$)	24°C 40 800°C 25	230 60
Dielectic Strength	24°C 250V/Mil	> 230V/Mil

Typical Chemical Analyses (Wt. %)

	Al_2O_3	SiO_2	Fe_2O_3	Ga_2O_3	TiO_2	MnO	Na_2O	K_2O	CaO	MgO
MV-30	60.0	38.0	.500	---	.500	---	.200	.700	.100	.200
998	99.8	.070	.025	.009	.004	.001	.005	---	.030	.050

high temperatures. Mullite tubes and crucibles were embedded in the casts and cast thickness was varied. Chromel metal wire was used to reinforce the castings; this practice did not prove successful since cracks were initiated at the points of contact between the wire and the castable ceramic. Furthermore, it was observed that the castable material (Castolast G) expands less than the fused parts (e.g. MV-30) on heating and as a result cracks. These cracks are avoided by using thicker and therefore stronger walls. Also, coating with wax before casting the fused ceramic surfaces in contact with the castable provides tolerance for expansion.

Using these techniques several ceramic reactors were designed, constructed and used in the study of methane pyrolysis. Three representative types are described in detail below. Reactor Type I is a cast reactor with an embedded mullite crucible. The water-cooled reactor, Type II, incorporates a cooling tube to keep part of the salt solidified and, thus, it partly avoids the problem of corrosion. Finally, the Annular Crucible and Tube (ACT) reactor is composed of fused parts combined with metal tube fittings. Even though cast reactors operated successfully, they were time-consuming to construct and less convenient than the ACT reactors.

Fig. 3.1.2 shows a Type I reactor. It consists of a mullite tube surrounded by a cast alumina (Castolast G) cylinder. The two internal parts, a reactant injection tube and a product exit tube, enter at the top of the reactor. During operation, the two-phase fluid (gas-melt) expands to occupy most of the mullite crucible below the castable. A baffle plate prevents the en-

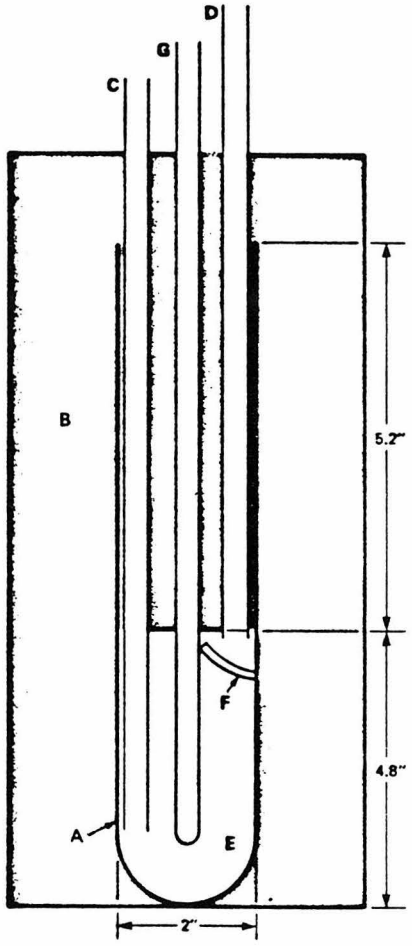

FIG. 3.1.2: REACTOR TYPE I

trainment of melt in the exit tube. This reactor type was used in preliminary studies of methane and ethylene pyrolysis (See Tables 3.3.1, .2, .3).

Fig. 3.1.3 shows a Type II reactor. Its main feature is a frozen salt layer created by the action of cooling water. The reactor consists of a mullite tube 2" I.D. and 30" long, with a 1/8" thick wall. The reactor is located vertically with its ends lying outside the furnace to maintain the stainless steel end plates and sealing surfaces (Viton gaskets) at a low temperature ($< 600^{\circ}F$). The furnace used with this reactor was of tubular design, Hevi Duty Electric Co. model MU-3024, operated with its axis in a vertical position. A short cylindrical plug of cast alumina (Castolast G) was placed at the lower end of the reactor tube with a cooling water coil embedded in the plug to keep the overlying layers of salt frozen. Above the frozen layer the salt is molten and its temperature is nearly uniform on account of the agitation by the reactant gases introduced through the alumina feed tube at the bottom. The frozen salt layer protects the alumina feed tube, the end steel plate and the gas inlet nozzle from the corrosive action of the melt. A movable thermocouple monitors the temperature profile in the reactor from just above the frozen salt layer to the upper end of the disengaging section. A disadvantage of the particular prototype constructed was its small wall thickness to diameter ratio, making the tube weak and unable to withstand the stresses created by the temperature gradient along the wall; this factor led to fracture of the mullite tube upon heating or cooling. Moreover, the control of the frozen salt layer through the cool-

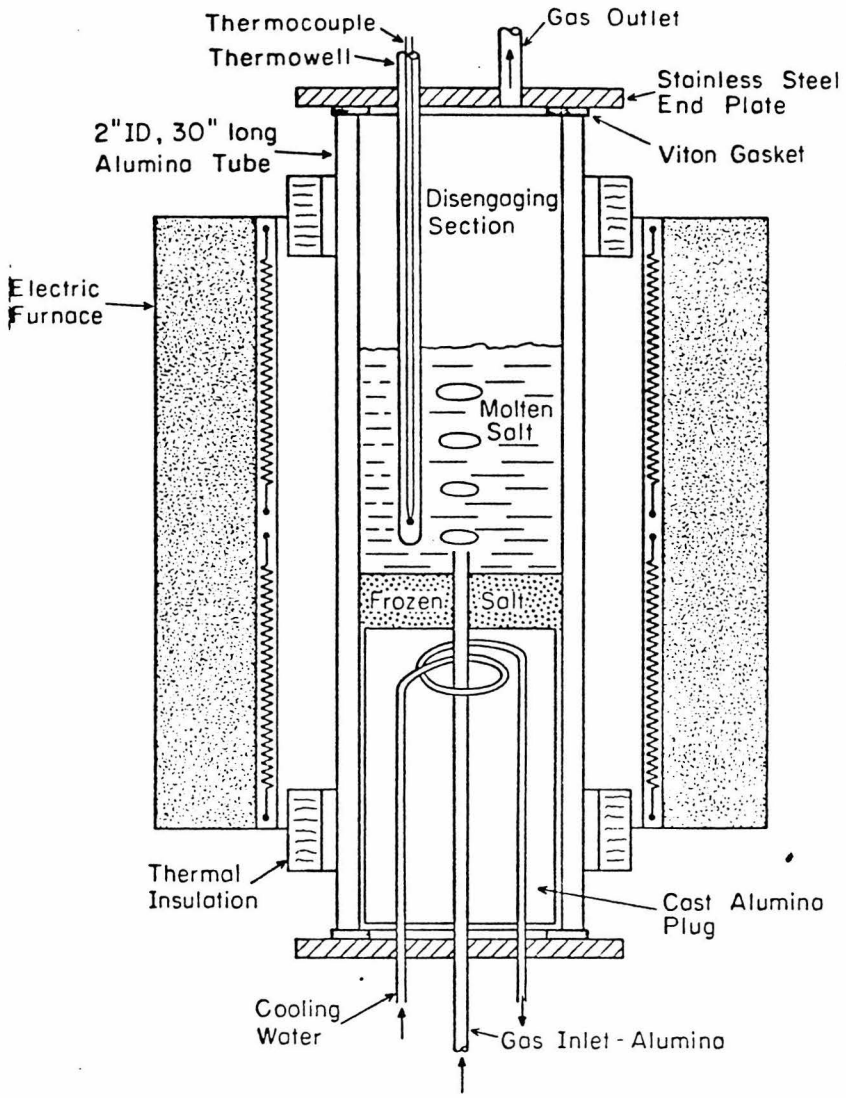

FIG. 3.1.3: WATER COOLED REACTOR, TYPE II.

ing water had to be very careful to avoid overcooling the salt and plugging the gas inlet. However, the concept of creating a frozen salt layer to avoid corrosion is a valid one in processes where the overall reaction is exothermic.

The most convenient reactor design used was that of the Annular Crucible and Tube (ACT) reactors. Fig. 3.1.4 shows the assembly of such a reactor and its positioning in the furnace. Fig. 3.1.5 shows the lowest part of the reactor. This type of reactor does not require using castable material. It is composed of fused alumina parts assembled with the use of stainless steel tube fittings. Three ceramic tubes are used in the reactor. The outer one is a closed-one-end tube (crucible), 3/4" I.D. x 1" O.D. x 12" long. The middle tube is open at both ends and has dimensions of 3/8" I.D. x 1/2" O.D. x 18" long. The innermost tube is closed at one end with dimensions of 3/16" I.D x 1/4" O.D. x 24" long and it serves as the thermocouple protection tube. The reactant gas mixture entered the reactor at the top of the middle tube and traveled downward in the annular space between the thermocouple tube and the middle tube. The gas was introduced at the bottom of the reactor and bubbled upwards through the melt. The depth of the salt bath was 1" to 2", depending on amount of salt used. After bubbling through the bath, the gases traveled upward in the annular space between the middle and outer tube. Finally, the gas exited at the top of the outer tube through the 1" tee.

The seal between steel fittings and ceramic parts consisted of Teflon ferrules. As can be seen in Fig. 3.1.4, all ferrules were protected from high temperatures by being placed above the

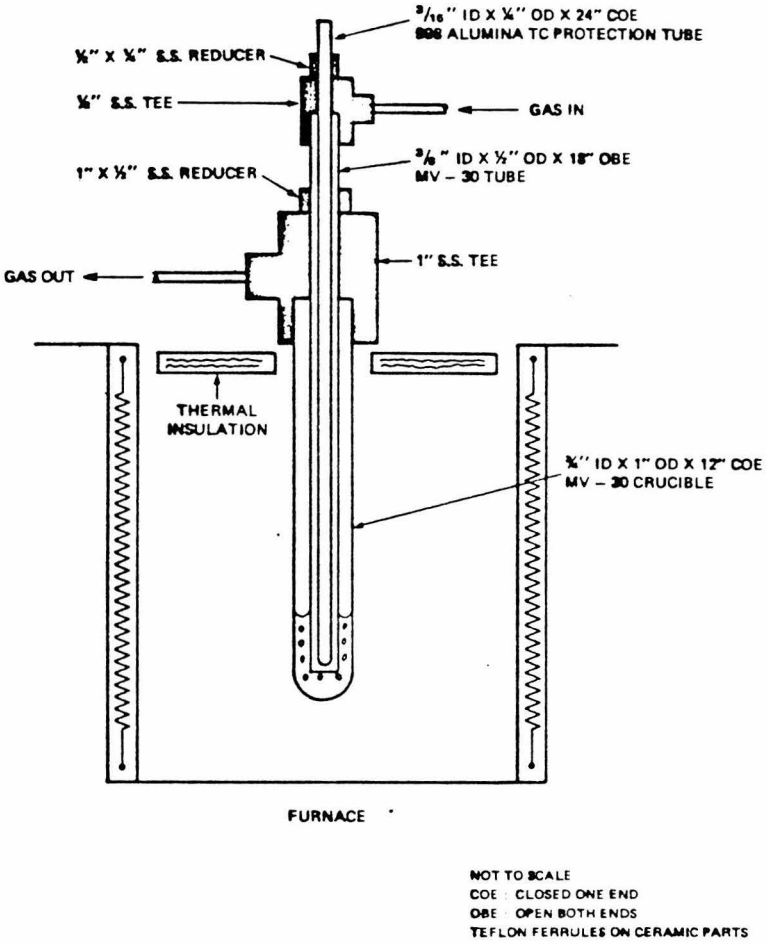

FIG. 3.1.4: ANNULAR CRUCIBLE AND TUBE (ACT) REACTOR

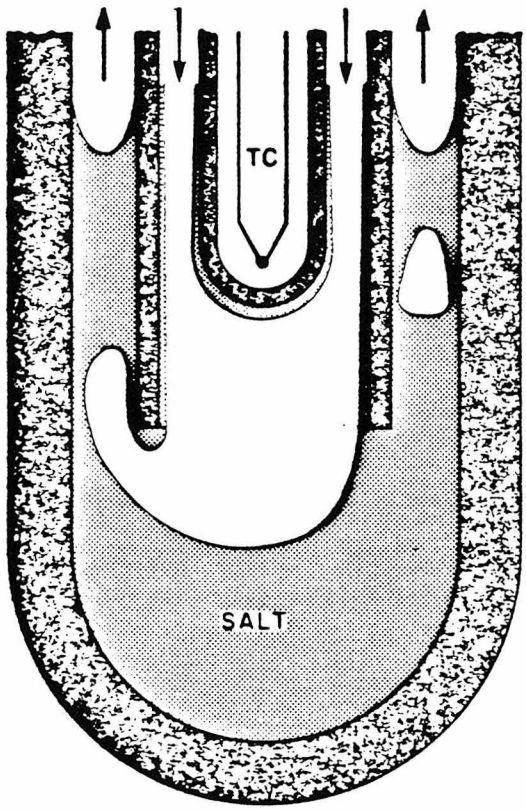

FIG. 3.1.5: ANNULAR CRUCIBLE AND TUBE (ACT) REACTOR BOTTOM SECTION

furnace. The section of the reactor lying above the furnace was wrapped with heating tape to preheat the gases and prevent condensation of vapors. At the beginning, there was concern about the temperature gradient at the point where the reactor emerges from the furnace (just below the 1" tee) causing the rupture of the outer crucible. Fortunately, the tube proved sufficiently strong to withstand this strain.

The reactor was prepared by the following procedure. First, the salt charge was placed in the reactor crucible before assembling the other parts. After that, crucible, middle tube and thermocouple tube were assembled and the reactor was placed in the furnace. The reactor was heated to the operating temperature at a rate of about 150^{o}C/hour. At the first stages of heating, the water of crystallization was removed from the salt. Above the melting point, the salt became fluid and heating continued until the desired operating temperature was reached.

A reactor prepared in this fashion lasted two to three weeks when used at temperatures between 800^{o} and 1000^{o}C. It eventually failed as the thermocouple tube corroded. This was the weakest part because it was exposed to the vigorously bubbling salt. The outer crucible and middle tube normally lasted longer. After failure or after completion of a set of experiments, the reactor was cooled to room temperature and opened to collect salt samples. The middle tube and the outer crucible were found to have sustained corrosion for a depth of about 1/16". No plugging problems because of solidified salt were experienced with this design. The annular space which serves as the outlet of the gas stream was wide enough to allow smooth disengagement between

salt and gases. Table 3.1.3 is a list of the ACT reactors used in the study of CH_4 pyrolysis.

The thermocouples inserted in the thermowells were provided by Wilcon Industries of South El Monte, CA. They were 30" long, chromel-alumel (Type K), ungrounded thermocouples, sheathed in inconel of .062" O.D.

The reactors discussed, Types I and II, and ACT, were not isothermal because of the distribution of heat losses in the reactor-furnace system. The hottest region of the reactors was at the bottom (salt bath) and the temperature decreased towards the top. This temperature gradient was recorded by moving the thermocouple along the thermowell. A discussion of the temperature gradient and its effect on the estimation of rate parameters is presented in Appendix I.

3.1.2 Materials and Analytical Methods

The sodium phosphate salts used were provided by Fisher Scientific Co. They were purified sodium metaphosphate, $(NaPO_3)_{13}$, and A.C.S. certified sodium pyrophosphate decahydrate, $Na_4P_2O_7 \cdot 10H_2O$. XRD analysis of the salts (See Figs. 5.2.1, 5.2.2) showed that the metaphosphate is amorphous, whereas the crystalline pyrophosphate contains many other sodium phosphates ($Na_4P_2O_7 \cdot 2H_2O_2 \cdot 8H_2O$, etc.). However, since the selected Na_2O: P_2O_5 ratio was chosen to be at a eutectic point for improved operability of the salt bath and not to optimize chemical properties, it was not of great concern that the component salts contained other sodium phosphates in small amounts.

The two salts were mixed at room temperature and added to the reactor crucibles. Near its melting point of 550°C, the mixture

TABLE 3.1.3

ANNULAR CRUCIBLE AND TUBE REACTORS

USED IN METHANE PYROLYSIS EXPERIMENTS

ACT	$NaPO_3$ (g)	$Na_4P_2O_7$ (g)	NiO (g)	TOTAL (g)	NiO (Wt.%)
1	---	---	---	0	---
2	2.5	1.5	---	4.0	---
3	8.8	5.6	---	14.4	---
4	---	---	---	0	---
5	---	---	---	0	---
6	8.5	5.4	---	13.9	---
8	---	---	---	0	---
9	8.5	5.4	---	13.9	---
19	9.0	5.3	.78	15.1	5.2
22	9.5	6.0	.50	16.0	3.1

is very viscous but becomes free-flowing above about 650°C. On cooling, the melt becomes colorless, transparent glass which after a few weeks at room temperature started becoming crystalline. The solidified salts -- glasses -- were analyzed chemically after the experiments to determine the effect of high temperature and exposure to reducing gases and H_2O on the melt composition. The analyses were performed by Analytical Research Labs, Inc. of Monrovia, CA. The glass samples were ground and dissolved in 4N HNO_3 solution after several hours of heating. The sodium content was determined by a flame ionization method. The phosphorus content was determined by titrating the acid phosphate (HPO_4^{--}) ions with NaOH solution. The interfering ions, e.g. Al^{+3}, were removed by an exchange method prior to the titration. After acid digestion, the solutions were found to contain considerable flocculant material that was presumed to be silica. As mentioned earlier, they also contained some aluminum ions. Both these components derive from the corrosion of the mullite crucibles. Table 3.1.4 presents the composition of two reactor baths before and after the experiments. It can be seen that the melt is enriched with Al and Si from the crucibles and depleted in Na and P. The depletion of Na is more pronounced as the decreasing Na/P ratio indicates. This may be due to vaporization of the volatile compounds Na, NaOH, while P_2O_5 was evidently less volatile under these conditions. Sample G 1 was exposed to a higher temperature; therefore, the extent of corrosion (Na, P concentrations less than in G 2) and Na volatilization (Na/P ratio less than in G 2) was more pronounced.

TABLE 3.1.4

EFFECT OF HIGH TEMPERATURES AND REACTOR ATMOSPHERE ON SALT BATH COMPOSITION

Reactor	Type I	Type I
Sample	G 1	G 2
Starting Composition:		
Na, mole %	24.09	24.09
P, mole %	18.25	18.25
Na/P	1.32	1.32
Balance	Oxygen	Oxygen
Treatment:		
Temperature Range:	800-1050°C	800-950°C
Duration:	∿1 wk.	∿1 wk.
Atmosphere:	CH_4	CH_4+H_2O
Chemical Analysis of Glass: (After experiments)		
Na, mole %	16.82	21.31
P, mole %	14.03	16.85
Na/P	1.20	1.26
Balance	Al, Si, O	Al, Si, O

Purified potassium metaphosphate and potassium pyrophosphate were obtained from Research Organic/Inorganic Chemical Corp. of Sun Valley, CA. They were used in some CH_4 - H_2O reforming runs (See Section 4.3) in the place of Na_2O - P_2O_5. NiO was provided by Matheson, Coleman and Bell Co. of Norwood, Ohio, in the form of a black-green reagent powder. When used, it was mixed with the other salts at room temperature. V_2O_5, used in some CH_4 - H_2O reforming runs (Section 4.4) with Na_2O - P_2O_5, was provided by Research Organic/Inorganic Chemical Co. as a yellow-black powder of 99.8% purity. It,too, was added and mixed with the other salts at room temperature.

The gases used were CH_4, C_2H_4 as reactants, and H_2, N_2, air CO - CO_2 mixtures, and hydrocarbon mixtures as diluents, reactants and/or calibration standards:

- Methane was provided by Matheson in a C.P. grade (99.0% CH_4 min.). It was analyzed by F.I.D. gas chromatography and found to contain 99.63% CH_4, .36% C_2H_6 and .001% C_3H_8.

- Ethylene was provided by Matheson as ethylene, C.P., 99.5% C_2H_4 minimum.

- Hydrogen and nitrogen were obtained in prepurified form (99.95%). Compressed air was supplied in pressurized cylinders by the Caltech Physical Plant Department.

- A certified CO - CO_2 mixture provided by Matheson was used to calibrate the IR instrument; its analysis was .98% CO_2, 5.82% CO, with N_2 as the balance.

- A certified hydrocarbon mixture provided by Matheson was used to calibrate the Hewlett-Packard F.I.D. G.C. It was com-

posed of H_2, CO, CO_2, CH_4, C_2H_2, C_2H_4, C_2H_6, C_3H_8, C_4H_{10}, C_5H_{12}.

Three gas chromatographs and an infrared analyzer were used to analyze samples in real time.

-A Varian Aerograph (Series 1400) G.C. fitted with a thermal conductivity detector was used to analyze H_2 and CH_4.

-A Loenco Model 15B thermal conductivity detector G.C. was used most extensively for the monitoring of CH_4 conversion to H_2. The column used was a ¼"x10' S.S. tube packed with 30% molecular sieve 5A and 70% molecular sieve 13X. The conditions were: N_2 carrier with an inlet pressure of 60psig, injection block temperature of 200°C, oven temperature of 110°C and filament current of 35 mA.

-A Hewlett-Packard Model 5710A, G.C. fitted with a flame ionization detector was used to analyze hydrocarbons in the C_1-C_5 range in methane and ethylene pyrolyses and in CH_4-H_2O reforming. The column used was a 1/8"x6' S.S. tube packed with 50/80 mesh Porapak Q. N_2 at P_{in}=35psig was the carrier. The instrument possesses an oven temperature programmer, Model 5702A, which was set at T_1=50°C for 2 min. and T_2=180°C with a rate increase of 8°C/min.

The signals from the chromatographs were connected to an integrator (Spectra Physics, Autolab System I) for digital integration of the peaks and for subsequent data reduction.

-A continuous non-dispersive infrared analyzer was used to monitor the CO and CO_2 content of product gases from CH_4 - H_2O reforming and reactor burn-off experiments. The instrument used was a Model IR-702 made by Infrared Industries of Santa Barbara, CA, capable of simultaneously analyzing CO and CO_2. The CO range was 0 - 2% low scale and 0 - 6% high scale; the CO_2 range was

0 - 0.3% low scale and 0 - 1.0% high scale. It was noted that the instrument response varied with gas flow rate; the response increased slightly at higher flow rates, presumably because of the slightly higher pressure in the detection tube. The instrument was calibrated with the CO - CO_2 - N_2 mixture referred to above at different flow rates. The reaction products were sometimes diluted with N_2 to be brought within the instrument range.

In some experiments, the product gas from methane pyrolysis was sampled with an impact particle separator. The instrument used was an 8-stage low-pressure impactor developed by Drs. Flagan and Friedlander of the Environmental Engineering Department, CIT (Hering, 1978, 1979). The impactor is cylindrically shaped, with a diameter of 2.5 inches, standing 18 inches high. Particles larger than 0.5 μm are sampled at atmospheric pressure using the first four stages. Four additional stages, operating at a pressure of 8-150mmHg absolute, segregate the smaller particles. Opaque particles (possibly coke) were found on the first stage (heavier particles); the lower stages showed many tar droplets. No particles or droplets were found in the four sub-atmospheric stages.

SECTION 3.2: EXPERIMENTAL PROCEDURE

In the study of methane pyrolysis, two experimental modes were employed:

(a) Flow of pure CH_4, and

(b) Flow of pure CH_4 followed by flow of air.

Preceding each experiment, air was flowed through at the usual experimental flow rates of 2 - 14 x 10^{-5} mol/s to consume any previous carbonaceous deposits. This flow was continued until the CO_2 level at the IR instrument decreased to the ambient air CO_2 content (.03%). At this point, the flow of air was interrupted and N_2 was flowed through, again at experimental flow rates. The flow of N_2 continued until the CO_2 reached a level undetectable by the IR (usually, this required about 10 minutes). The N_2 flow was then stopped and CH_4 was introduced. GC samples and IR readings were taken every five minutes for the first hour and every 10-30 minutes for subsequent hours of operation. In this way, the CH_4, H_2, CO and CO_2 contents of the exit gas were continuously monitored. In experimental mode (a), the product composition reached a steady state after 5-15 minutes of operation. The delay is due to transport lag and Taylor diffusion in the lines where the flow is laminar. The lines were 20' long and 1/4" in diameter. The data used for the kinetic calculations were obtained after 40 minutes of operation. After termination of each run, the above steps (N_2 flow for 10 minutes, air flow afterwards) were reversed.

In mode (b), a flow of CH_4 of a certain duration was followed by a flow of N_2 for 10 minutes followed by a flow of air, all at the same flow rate. During the air flow, IR readings were taken

every 30 seconds and the CO, CO_2 levels were used to calculate the carbon content in the reactor. This carbon had been deposited in the reactor during the period of methane pyrolysis. A period of air flow of 10-20 minutes was sufficient to consume the carbon inventory and to reduce the CO level to zero and the CO_2 level to a little above ambient air levels. The carbon burn-off was not complete at that point, because carbon deposited in colder parts of the reactor oxidized at a slower rate. However, the leveling off of the CO_2 reading was taken as a cut-off point for the calculation of the carbon inventory in the hot regions of the reactor. Air flow was continued for a few hours before an experiment of mode (a) or (b) could be performed again.

In the study of the steam reforming of methane (discussed in detail in Chapters 4 and 5), both steam and methane were flowed through in experiments of mode (a). For experiments of mode (b), the period of methane-steam reforming was followed by a period of nitrogen-steam flow to consume the carbon inventory. In this case, carbon was removed by the steam-carbon reaction. The same leveling-off in the CO_2 content of the product gas was used to signal the end of carbon removal from the hottest parts of the reactor.

SECTION 3.3: RESULTS OF METHANE PYROLYSIS IN BLANK REACTORS AND IN REACTORS CONTAINING Na_2O-P_2O_5 AND Na_2O-P_2O_5-NiO

Most of the experiments involving methane pyrolysis were carried out in the Annular Crucible and Tube (ACT) reactors. Certain other reactors were used in preliminary runs to determine the reactivity of CH_4 and the range of products under cracking conditions.

Tables 3.3.1 and 3.3.2 present such results in two cast reactors of Type I, one blank and the other with Na_2O-P_2O_5 salt. The melt in the salt-containing reactor occupied about half the reactor's volume and covered about half its internal surface area. Therefore, only half of the volume and surface area were available for reaction in the salt-containing reactor as compared to the blank reactor. The feed methane contained a small amount of ethane, C_2H_6, and other alkanes.

The results show that at high temperatures, the alkanes pyrolyze mostly to H_2 and unsaturated hydrocarbons, e.g. C_2H_2, C_2H_4, etc. If account is taken of the difference in volume and area between the two reactors, the reactivities and product distributions are similar in the presence and absence of molten salt.

In addition to methane, a number of experiments were conducted in the pyrolysis of ethylene. Table 3.3.3 lists the product distribution from C_2H_4 pyrolysis in a Type I reactor under conditions similar to those of CH_4 pyrolysis as listed in Tables 3.3.1 and 3.3.2. It can be seen that C_2H_4 is much more

TABLE 3.3.1

METHANE PYROLYSIS

Typical Product Distribution

No Salt Reactor Type I

T(^{o}K)		1127	1178
Feed	CH_4	99.63%	99.63%
	C_2H_6	0.37	0.37
	Flow Rate, mol/s	8.1×10^{-5}	8.1×10^{-5}
Products	H_2	3.94%	21.02%
	CH_4	95.56	78.09
	C_2H_2	0.00	0.00
	C_2H_4	0.37	0.76
	C_2H_6	0.09	0.08
	C_3H_x	0.05	0.06
	C_{4+}*	Trace	Trace

Reactor Volume: $63cm^3$ Reactor Surface Area: $110cm^2$

* Trace amounts of these species were observed, but GC sensitivity was not high enough to record the amount.

TABLE 3.3.2

METHANE PYROLYSIS

Typical Product Distribution

Salt: $Na_2O-P_2O_5$ Reactor Type I

$T(^oK)$		1127	1178
Feed	CH_4	99.63%	99.63%
	C_2H_6	0.37	0.37
	Flow Rate, mol/s	8.1×10^{-5}	8.1×10^{-5}
Products			
	H_2	1.83%	11.23%
	CH_4	97.62	87.16
	C_2H_2	0.00	0.32
	C_2H_4	0.37	1.15
	C_2H_6	0.11	0.14
	C_3H_x	0.07	0.01
	C_{4+}*	Trace	Trace

Reactor Volume: $45cm^3$ Reactor Surface Area: $81cm^2$

*Trace amounts of these species were observed, but GC sensitivity was not high enough to record the amount.

TABLE 3.3.3

ETHYLENE PYROLYSIS

Typical Product Distribution

Reactor Type I		
Volume, cm^3	63	45
Surface Area, cm^2	110	81
Salt	No Salt	$Na_2O-P_2O_5$
Ethylene Feed		
Flow Rate, mol/s	6.1×10^{-5}	6.1×10^{-5}
Temperature, ^oK	1115	1115
Products, %		
H_2	37.2	27.6
CH_4	32.2	32.6
C_2H_2	0.1	0.9
C_2H_4	25.2	32.6
C_2H_6	4.4	4.3
C_3H_x	0.4	1.0
C_4H_x	0.5	1.0
C_{5+}*	Trace	Trace

* Trace amounts of these species were observed, but GC sensitivity was not high enough to record the amount.

reactive. The comparison between the two gases is in accord with the results from previous studies indicating that CH_4 is the most refractory hydrocarbon in regard to pyrolysis.

3.3.1 Effect of the Partial Pressure of Methane on the Reaction Rate

To examine the kinetics of methane pyrolysis, mixtures of CH_4 and N_2 at constant total flow rate were passed through ACT reactors. Table 3.3.4 and Fig. 3.3.1 present the effect of methane concentration on the pyrolysis rate, $-r_{CH_4}$. First order kinetics with respect to CH_4 appear to be applicable.

3.3.2 Effect of Salt on the Rate

The pyrolysis reaction was carried out at many temperatures and in reactors with or without salt. Table 3.3.5 presents the rates obtained in the empty reactors and Table 3.3.6 presents the results in reactors containing Na_2O-P_2O_5. No significant difference in reactivity is apparent. Fig. 3.3.2 depicts both sets of results.

Table 3.3.7 presents the data for the Na_2O-P_2O_5-NiO system and these results are also included in Fig. 3.3.2. The results at both temperatures indicate no rate enhancement by the added NiO.

The reaction rate did not change appreciably with time, past the initial period of 5-15 minutes (See section 3.2, Experimental Procedure). The production of H_2 remained constant even if the reaction had been carried out for many hours.

3.3.3 Elutriation of Pyrolysis Products

Methane pyrolyzes into a variety of products ranging from H_2 to unsaturated hydrocarbons, heavy tars and finally coke:

TABLE 3.3.4

PYROLYSIS OF CH_4 IN ACT REACTORS

Effect of CH_4 Concentration on the Rate

Salt = $Na_2O-P_2O_5$ P = 1 atm. T = 1146°K

Balance = Nitrogen $\dot{n}_T = 8.1 \times 10^{-5}$ mol/s

Run	(CH_4)(mol/cm^3)	$-r_{CH_4}$(mol/s)
9.N1	10.3×10^{-6}	65.7×10^{-8}
9.N2	0.6 "	2.25 "
9.N3	5.1 "	29.0 "
9.N4	2.6 "	23.2 "
9.N5	6.5 "	32.0 "
9.N6	0.7 "	0 "
9.N8	2.3 "	17.9 "
9.N9	3.2 "	22.6 "
9.N11	10.3 "	50.6 "

Model: $(-r_{CH_4}) = k_m(CH_4)$

By linear regression: $k_m = .0659$ cm^3/s

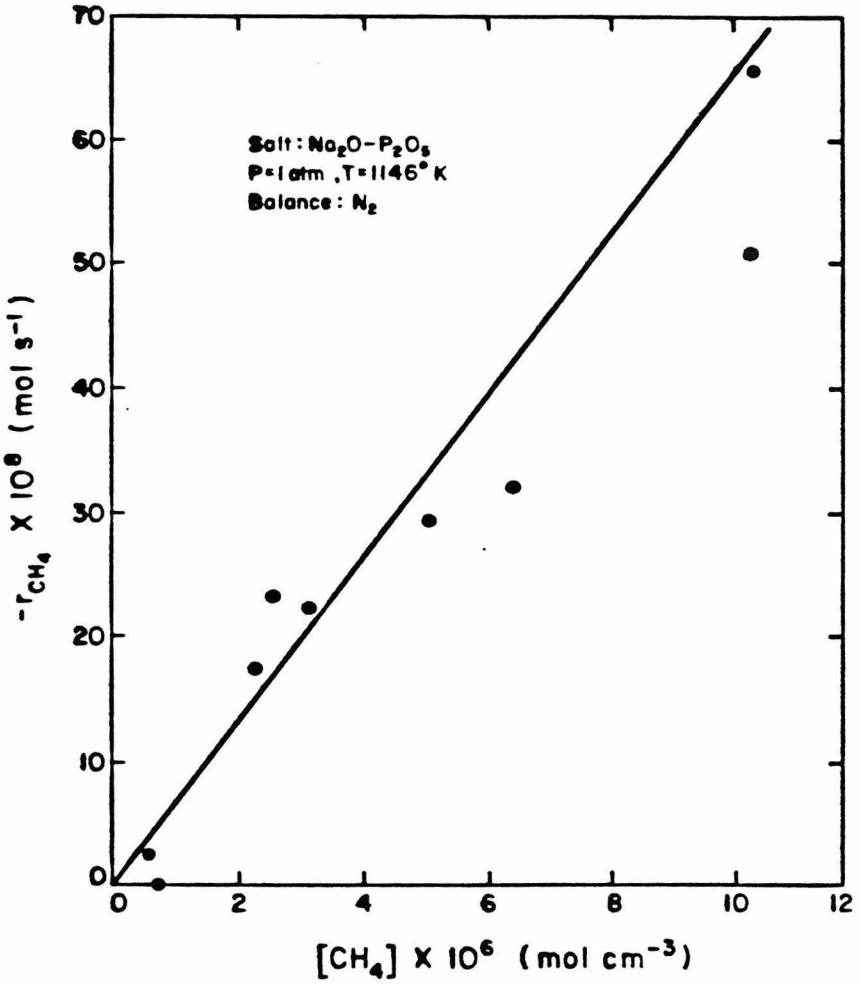

FIG. 3.3.1: EFFECT OF CH_4 CONCENTRATION ON THE RATE

TABLE 3.3.5

PYROLYSIS OF METHANE IN ACT REACTORS

No Salt $p^{o}_{CH_4}$ = 1 atm.

Run	T(^{o}K)	$\dot{n}_T$(mol/s)	$-r_{CH_4}/p_{CH_4}$(mol/s/atm)
1.1	1034	3.7×10^{-5}	2.49×10^{-8}
1.4	1099	3.7 "	15.99 "
4.1	1045	1.7 "	4.39 "
5.2	1105	3.7 "	17.98 "
5.3	1132	3.7 "	33.08 "
5.4	1168	3.7 "	92.13 "
5.5	1196	3.7 "	211.0 "
8.2	1154	3.7 "	64.24 "

Calculated E_a = 62 Kcal/mol

TABLE 3.3.6

PYROLYSIS OF METHANE IN ACT REACTORS

Salt: $Na_2O-P_2O_5$ $p^o_{CH_4}$ = 1 atm.

Run	T(^oK)	$\dot{n}_t$(mol/s)	$-r_{CH_4}/p_{CH_4}$(mol/s/atm)
2.5	1211	3.7×10^{-5}	156.6×10^{-8}
2.6	1234	3.7 "	367.2 "
2.7	1265	9.0 "	782.3 "
2.10	1055	1.8 "	4.42 "
3.1'	1068	1.7 "	7.07 "
3.1"	1076	1.7 "	11.03 "
3.2"	1094	1.7 "	19.13 "
3.3	1146	3.7 "	75.94 "
6.1	1114	3.7 "	34.12 "

Calculated E_a = 60 kcal/mol

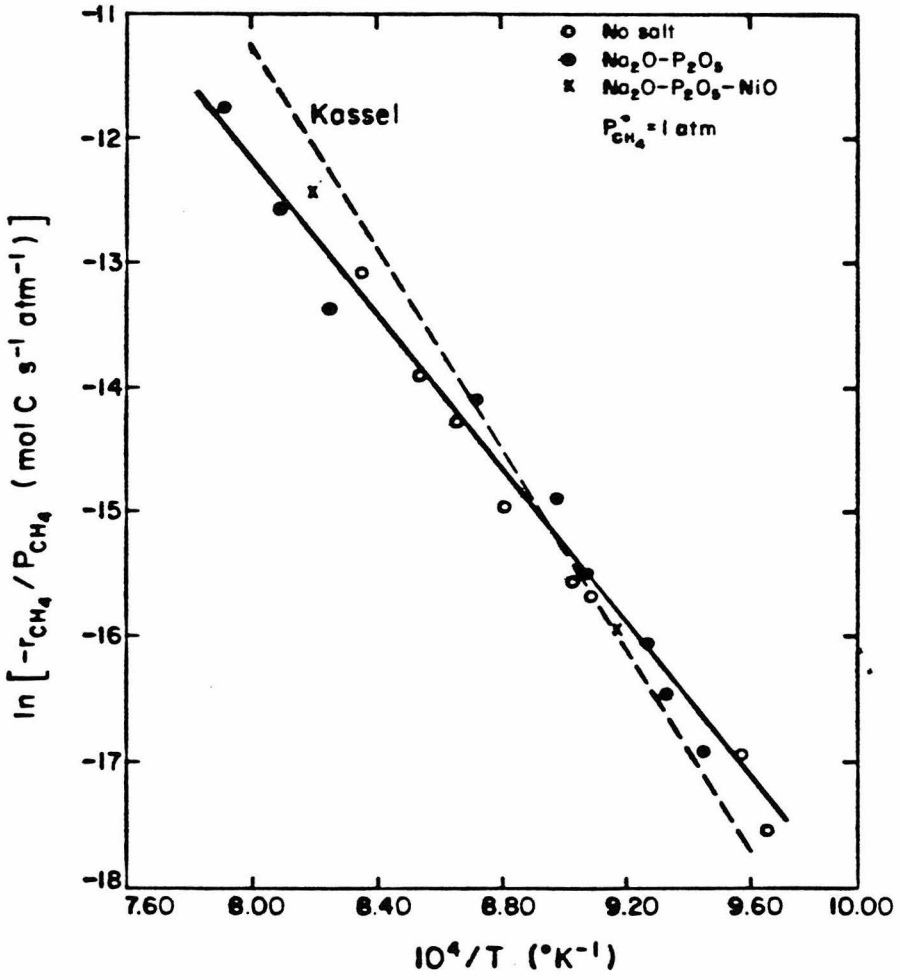

FIG. 3.3.2: CH_4 PYROLYSIS IN ACT REACTORS

TABLE 3.3.7

PYROLYSIS OF METHANE IN ACT REACTORS

Salt: $Na_2O-P_2O_5-NiO$ $p^o_{CH_4}$ = 1 atm.

Run	T(^oK)	$\dot{n}_t$(mol/s)	$-r_{CH_4}/p_{CH_4}$(mol/s/atm)
22.1	1091	1.7×10^{-5}	4.25×10^{-8}
19.3	1220	14.0 "	400.0 "

(THIS PAGE IS BLANK, DUE TO ERROR IN PAGINATION)

$$CH_4 \rightarrow H_2, C_2H_2, C_2H_4, \ldots, C_xH_y, \ldots, \text{coke} \qquad (3.3.1)$$

The lighter products were detected by G.C. analysis (Tables 3.3.1 and 3.3.2) whereas tars were collected on glass wool filters at the reactor exit. When reactors were opened at room temperature, without having been previously exposed to a flow of oxygen, carbonaceous deposits were found. These deposits consisted of particles about .1mm in size attached to the mullite walls or the salt surface. For very long durations of methane flow, the deposits took the appearance of sheets covering the reactor walls.

The effect of the duration of CH_4 flow (duration of run) on the carbon inventory in the reactor, n_c, is shown in Table 3.3.8 and Fig. 3.3.3 for experiments of mode (b) (See section 3.2 for procedure). It can be seen that the carbon inventory leveled off at higher durations of CH_4 flow.

The carbonaceous residue found in the reactor after cooling to room temperature was identified as coke. The pyrolysis products exiting the reactor were of a wider spectrum including gases, light liquids and tars.

3.3.4 Impact Particle Separator Study

To determine the identity of elutriated pyrolysis products, reactor off-gases were passed through an impact particle separator in which particles could be collected and classified according to size. Fig. 3.3.4 presents drawings of microscopic views of separator disks. Disks $M_2 1$ and $M_2 4$ are the top (heavier particles) and the fourth from the top. The samples were taken

TABLE 3.3.8

METHANE PYROLYSIS IN ACT REACTORS

Variation of Carbon Inventory with Duration of CH_4 Flow.

Mode (b) Experiments

Salt: $Na_2O-P_2O_5$

Duration of CH_4 Flow (min)	T(^oK)	Carbon Burned Off (mol)	Eq. Carbon Burned Off @ 1164^oK(mol)
31	1164	13.9×10^{-5}	13.9×10^{-5}
59	1164	30.4 "	30.4 "
89	1162	39.9 "	41.8 "
187	1165	50.9 "	49.7 "
269	1175	53.0 "	40.9 "

$\dot{n}_{CH_4,\ in} = 13.3 \times 10^{-5}$ mol/s

$\dot{n}_{N_2,\ in} = 13.3 \times 10^{-5}$ mol/s, for 10 minutes

$\dot{n}_{Air,\ in} = 13.3 \times 10^{-5}$ mol/s, for 10-20 minutes

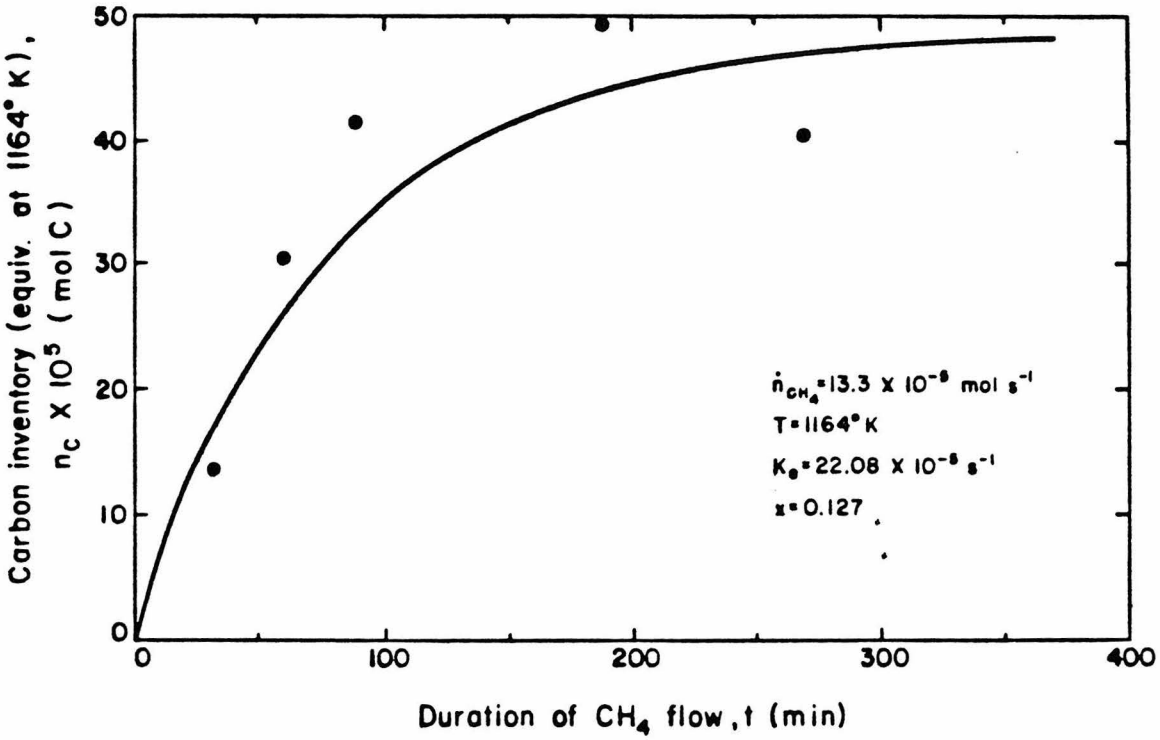

FIG. 3.3.3: CH_4 PYROLYSIS. VARIATION OF CARBON INVENTORY WITH DURATION OF CH_4 FLOW

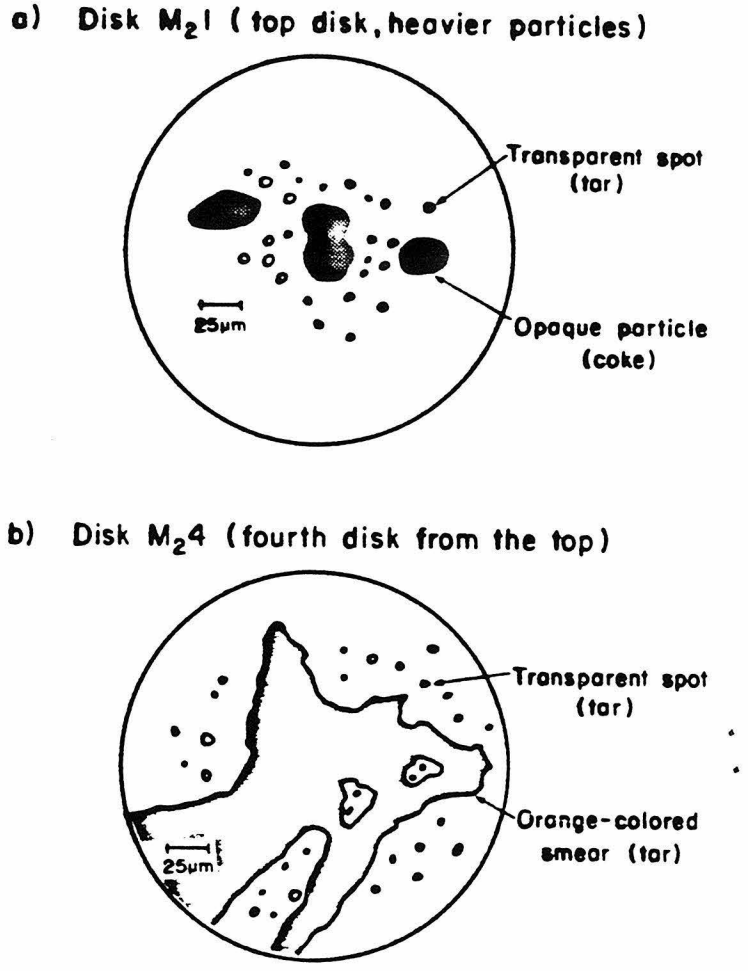

FIG. 3.3.4: ELUTRIATION OF CH_4 PYROLYSIS PRODUCTS. IMPACT PARTICLE SEPARATOR STUDY. $T = 1218^{o}K$, $\dot{n}_{CH_4} = 14 \times 10^{-5}$ mol/s, t = 60 min. LIGHT MICROSCOPE VIEWS

60 minutes after the start of a mode (a) experiment (CH_4 pyrolysis). Disk $M_2 1$ shows opaque particles, possibly coke, as well as small transparent spots (tar). The spots were identified as tar because of their oily liquid appearance. Disk $M_2 4$ shows a large, orange-colored tar smear. Smaller, transparent tar spots were also present. It can be concluded that tar compounds escaped the reactor to condense at cooler surfaces downstream. Coke particles also escaped as evidenced by Disk $M_2 1$.

Fig. 3.3.5 shows microscopic examinations of materials scraped from reactor walls. Large carbonaceous plates (coke) were apparent as well as crystalline salt particles (Fig. 3.3.5 (b)). It is interesting to note that the coke particles exhibit pockmark-like spots. These could be the remainders of bubbles of pyrolysis gases evolving from inside the coke deposit. The salt found close to the top of the reactor derives from the bursting of gas bubbles forming small salt droplets which solidified when the reactor was cooled. The carbonaceous matter found in the higher regions of the reactor had a fuzzy appearance possibly because of its formation as chain agglomerates of particles.

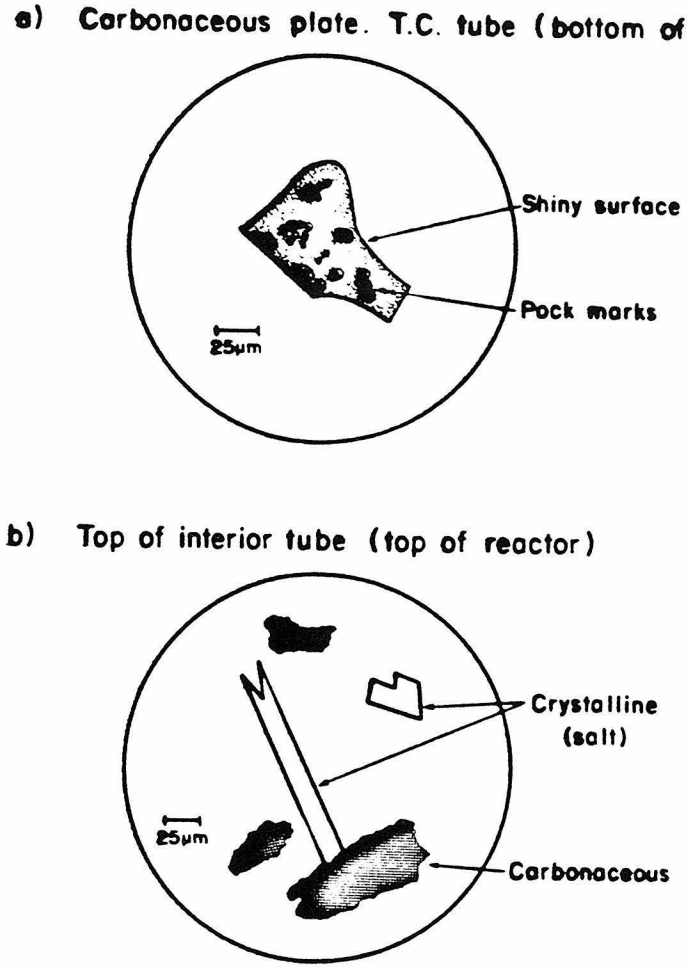

FIG. 3.3.5: CH_4 PYROLYSIS. CARBONACEOUS DEPOSITS FROM REACTOR WALLS. LIGHT MICROSCOPE VIEWS

SECTION 3.4: DISCUSSION OF METHANE PYROLYSIS RESULTS

A linear regression analysis showed that the rate of methane pyrolysis could be represented by first order kinetics (Table 3.3.4, Fig. 3.3.1):

$$-r_{CH_4} = k_m(CH_4) \qquad (3.4.1)$$

At T = 1146°K the rate constant k_m had the value .0659 cm^3/s for the ACT reactors. The activation energy E_A in an Arrhenius representation of k_m was calculated taking into account the temperature gradient in the reactors. This procedure is presented in Appendix I. The calculated activation energy is in the range of 60-64 kcal/mol. This must be compared with the value of 79 kcal for the homogeneous reaction reported by Kassel (1932) and Steacie (1954):

$$k_m^1 = 1.0 \times 10^{12} \exp(-79{,}385/RT)\ s^{-1} \qquad (3.4.2)$$

Figure 3.3.2 shows that the rate calculated using (3.4.2) also fits the data within experimental error. The lower activation energy estimated by linear regression could reflect surface effects on the free-radical gas-phase reactions. Surface initiation on the mullite or the salt would be effective inasmuch as the mass transfer between the surfaces and the bulk of the gas is very rapid (See Appendix II). The absence of any bending in the Arrhenius curve of Fig. 3.3.2 is an additional indication of the absence of mass transfer limitation.

3.4.1 Carbonaceous Deposits

Carbonaceous deposits on reactor walls result from surface reactions and from deposition of particles originating in homogeneous reactions. The build-up of a carbon inventory in a

reactor under typical conditions is presented in Fig. 3.3.3. During an initial period of CH_4 flow (30-60 minutes), the rate of deposition was .281 μg C $min^{-1}cm^{-2}$. However, at longer times the carbon inventory leveled off. Trimm (1977) reported a rate of 4μg C $min^{-1}cm^{-2}$ for n-C_4H_{10} cracking on SiO_2 at 1073°K. After accounting for the higher pyrolysis rate of butane (Steacie, 1954), the two deposition rates are comparable.

The build-up of the carbonaceous (coke) inventory in the reactor can be modeled as follows:

- Carbon is produced by the pyrolysis reaction either in the gas phase or on a surface;

- A fraction, x, of this carbon is retained on the reactor surfaces; the remainder, 1-x, immediately escapes with the exiting gases;

- The inventory of carbon suffers elutriation by the continuing shear of the gases; this elutriation is assumed to be proportional to the carbon mass in the reactor, n_c (gmols C):

$$\text{elutriation} = k_e n_c \tag{3.4.3}$$

where k_e (s^{-1}) is the rate constant for elutriation. The above lead to:

$$\frac{dn_c}{dt} = xk_m(CH_4) - k_e n_c \tag{3.4.4}$$

Starting with a clean reactor (no carbon deposits):

$$n_c = 0 \text{ at } t = 0 \tag{3.4.5}$$

Equation (3.4.4) is integrated to:

$$n_c = \frac{xk_m(CH_4)}{k_e}\left(1 - e^{-k_e t}\right) \tag{3.4.6}$$

As time progresses, a steady-state is established for the carbon inventory:

$$n_c\Big|_{s.s.} = \frac{xk_m(CH_4)}{k_e} \qquad (3.4.7)$$

The carbon inventory levels off when the production of coke is balanced by elutriation. The rise time of this balancing process is indicative of k_e, whereas the initial slope depends on x. To calculate k_e and x from the data on Table 3.3.8, it was assumed that elutriation was not significant during the relatively short periods of N_2 flush and air burn-off. Additionally, since k_m is a strong function of T (E_a of CH_4 pyrolysis $\sim$ 62kcal), the data were reduced to a single temperature assuming that x and k_e were relatively constant for these temperature differences, but that k_m did vary with T. Using nonlinear regression, the following values were obtained:

$$k_e = 2.2 \times 10^{-4}\ s^{-1} \qquad (3.4.8)$$

and $$x = .13 \qquad (3.4.9)$$

Under these conditions, the rise time to steady-state was about three hours. The fraction x can be thought of as the ratio of the surface reaction rate to the overall reaction rate and should vary with reaction temperature and surface composition. The parameter k_e should depend on gas velocity (shear forces) and interfacial forces between carbonaceous matter on the one hand and reactor wall and/or salt melt on the other.

Alternative models of coke deposition have been proposed. The rate of coke deposition can be assumed to be inversely proportional to the coke already on the surface:

$$\frac{dn_c}{dt} = \frac{a_p}{n_c} \tag{3.4.10}$$

This assumption is made on the basis of considerations of surface coverage by coke and subsequent surface availability for reaction. Equation (3.4.10) leads to the expression:

$$n_c = \sqrt{2a_p t} \tag{3.4.11}$$

According to (3.4.11), no steady-state is established, but coking continues, although at an ever-decreasing pace. The results presented in Fig. 3.3.3 can fit either this model or the elutriation model. However, the impact particle separator experiments showed possible coke particles in the product gas in support of the elutriation model and the attainment of a steady-state carbon inventory.

SECTION 3.5: CONCLUSIONS

The products identified during the methane pyrolysis experiments ranged from H_2 (major product) to light hydrocarbons, tar and coke. The pyrolysis of ethylene showed a similar range of products but greater reactivity. The reactivities of CH_4 and C_2H_4 were not affected by the presence of Na_2O-P_2O_5 or Na_2O-P_2O_5-NiO melt in the reactors.

The kinetics of CH_4 pyrolysis were independent of the salt used and can be described by a first order reaction with activation energy of about 62 kcal/gmol. This must be contrasted with the activation energy of homogeneous pyrolysis known to be 79 kcal. The difference might be due to the participation of the reactor surface in initiation and termination reactions.

The reaction products include light gases, tar and coke. The tar exits the reactor in vapor form. Some of the coke is carried with the gases and some remains in the reactor to form a carbon inventory. The instantaneous ratio of deposited coke to coke produced by pyrolysis is about 12.7%. However, elutriation removes part of the coke already deposited in the reactor. Eventually, the processes of coke deposition and coke elutriation reach a balance and a steady-state carbon inventory is established.

The exit gas was sampled for particulates with an impact particle separator. Tar was evident on the collecting disks, along with some opaque particles which were tentatively identified as coke.

CHAPTER FOUR

METHANE STEAM REFORMING

SECTION 4.1: EXPERIMENTAL

4.1.1 Steam Generation

The experimental set-up described in the previous chapter (Fig. 3.3.1) was modified to allow the introduction of steam. Electric tape (R=17 ohms) was wrapped around a Pyrex glass flask, the stainless teel tube leading from the steam generator to the reactor inlet and the tube connecting the reactor outlet to the condenser. A glass thermometer read the temperature at the water surface in the generator flask. The power to the heating tapes was regulated with Variacs; the voltage to the steam generator flask varied from 0 to 60 volts, depending on the desired mol fraction of steam, whereas the voltage to the tubes was kept at 90 volts to ensure that no steam condensed there.

Methane was bubbled through the flask to carry steam at the partial pressure corresponding to the temperature set by the heating tape. The methane-steam mixture was introduced in the reactor and the product gases were led to the condenser. The latter consisted of an air-cooled coil and a separator where unreacted water was collected and measured. The gases (now at room temperature) then passed through a Drierite-filled tube to remove residual water vapor before entering the analytical instruments (G.C.s and IR).

Two methods were used to estimate the flow rate of H_2O through the reactor:

(a) Measuring the condensed water flow rate along with the calculated water consumption;

(b) Assuming that the partial pressure of steam in the

steam generator and the reactor was the equilibrium vapor pressure at the thermometer temperature.

Table 4.1.1 compares these two measurements. The mole fraction of steam derived from the condensate measurements is consistently below the fraction derived, assuming saturation conditions in the steam generator. This can be explained by some condensation at the top of the generator flask which sustained large heat losses and was at a somewhat lower temperature than the one indicated by the thermometer. As a result of this discrepancy in the two measurements, only the condensate-derived steam fraction was used in the calculations. The temperature of the water in the generator was used only as a rough indication of y_{H_2O} and as a monitor of the transient resulting from changes in the voltage of the heating tape.

4.1.2 Molten Media and Catalysts

Both blank (no-salt) ACT reactors and ACT reactors containing different salt mixtures were used in steam-methane reforming experiments to determine the reaction rate as a function of quantity and composition of the melt. The melts used were similar to the ones described in Section 3.1 An additional melt mixture used was Na_2O-P_2O_5-V_2O_5. The procedure for preparing the reactor was as described previously: a mixture of salts and oxides was added to the bottom of the crucible before assembling the ACT reactor. Table 4.1.2 is a listing of the ACT reactors used in steam reforming experiments along with their salt loadings.

TABLE 4.1.1

$T_{S.G.}$ (^{o}C)	$p^{o}_{H_2O}$ (mmHg)	$(y^{o}_{H_2O})$ thermometer	$(y^{o}_{H_2O})$ condensate
61.5	161	.21	.13
62.5	168	.22	.12
67.0	205	.27	.18
85.0	434	.57	.24
90.5	536	.71	.55

TABLE 4.1.2

Annular Crucible and Tube Reactors (ACT)	$NaPO_3$ (g)	$Na_4P_2O_7$ (g)	NiO (g)	V_2O_5 (g)	Total (g)	NiO (wt %)	V_2O_5 (wt %)
1	---	---	---	---	0	----	----
2	2.5	1.5	---	---	4.0	----	----
3	8.8	5.6	---	---	14.4	----	----
4	---	---	---	---	0	----	----
5	---	---	---	---	0	----	----
6	8.5	5.4	---	---	13.9	----	----
7	8.5	5.4	---	---	13.9	----	----
8	---	---	---	---	0	----	----
9	8.5	5.4	---	---	13.9	----	----
12	---	---	---	---	0	----	---
13	8.3	5.5	---	---	13.8	----	----
14	20.4	12.6	---	---	33.0	----	----
16	10.4(*)	10.3(*)	---	---	20.7	----	----
17	8.3	5.5	3.7	---	17.5	21.1	----
18	9.0	5.3	.78	---	15.1	5.2	----
19	9.0	5.3	.78	---	15.1	5.2	----
20	---	---	---	---	0	----	----
21	10.2	6.1	---	---	16.3	----	----
22	9.5	6.0	.50	---	16.0	3.1	----
23	9.4	6.0	.28	---	15.6	1.8	----
24	9.7	6.0	.28	---	15.6	1.8	----
25	9.7	5.8	---	1.95	17.5	----	11.1
27	9.7	5.9	---	5.1	20.7	----	24.6
28	9.7	5.9	1.4	5.1	22.1	6.3	23.1
29	9.7	5.9	4.9	5.1	25.6	19.1	19.9

(*) Potassium phosphates instead of sodium phosphates

Table 4.1.2 continued

Annular Crucible and Tube Reactors (ACT)	$NaPO_3$ (g)	$Na_4P_2O_7$ (g)	NiO (g)	V_2O_5 (g)	Total (g)	NiO (wt %)	V_2O_5 (wt %)
30	16.2	9.4	5.6	---	31.2	17.9	----
31	15.7	9.7	5.6	---	31.0	18.1	----
32	16.0	9.6	5.5	---	31.1	17.7	----
33	15.9	9.7	1.17	---	26.8	4.4	----
34	15.5	9.2	1.00	---	25.7	3.9	----
36	8.0	4.9	.38	---	13.3	2.9	----
37	8.0	4.7	.40	---	13.2	3.0	----
38	8.0	4.8	.49	---	13.3	3.7	----
39	8.1	4.3	.38	---	12.8	3.0	----

SECTION 4.2: STEAM REFORMING OF METHANE IN BLANK ACT REACTORS

Table 4.2.1 presents representative data on steam reforming of methane in the ACT reactors in the absence of any salt. The rate of carbon oxide formation was calculated as:

$$r_{CO_x} = \dot{n}_T \frac{p_{CO} + p_{CO_2}}{p_{total}} \text{ mol / s} \qquad (4.2.1)$$

The rate was normalized by p_{CH_4}, and this normalized variable, r_{CO_x}/p_{CH_4}, is plotted vs. the temperature in Fig. 4.2.1. It can be seen that the calculated activation energy of 65 kcal/mol is close to that for the pyrolysis reaction reported in Chapter 3. However, the absolute size of the normalized rate is smaller than the corresponding rate of CH_4 disappearance because of pyrolysis. This suggests that some carbonaceous material resulting from CH_4 pyrolysis does not participate in the carbon-steam reaction, but is removed from the reactor in the form of gaseous products, tar or coke.

Table 4.2.2 presents the rates of the CH_4-H_2O reaction at a single temperature and various CH_4 to H_2O ratios. Figure 4.2.2 depicts the variation of r_{CO_x}/p_{CH_4} as a function of p_{H_2O}. It is clear from this last graph that a high steam partial pressure adversely affects the rate of carbon oxide formation. The rate of H_2 formation (indicative of pyrolysis) does not decrease, suggesting that pyrolysis is not adversely affected by a high p_{H_2O}.

TABLE 4.2.1

STEAM REFORMING OF METHANE IN BLANK ACT REACTORS

No Salt $\bar{p}$ = 1 atm.

Run	T(^{o}K)	$\dot{n}_T$(mol/s)	$p_{CO}+p_{CO_2}$ (atm)	p_{H_2} (atm)	p_{CH_4} (atm)	p_{H_2O} (atm)	r_{CO_x} (mol C/s)	r_{CO_x}/p_{CH_4} (mol C/s/atm)
8.T2	1136	21.7 x 10^{-5}	.00002	.00041	.078	.92	.43 x 10^{-8}	5.6 x 10^{-8}
5.T4	1165	12.8 "	.00008	.00105	.133	.87	1.02 "	7.7 "
20.T2(5)	1193	21.2 "	.00059	.00208	.66	.34	12.5 "	19.0 "
5.T5	1198	10.4 "	.00057	.00222	.163	.84	5.9 "	36.4 "
20.T3(2)	1218	15.0 "	.00177	.00618	.93	.068	26.5 "	28.5 "

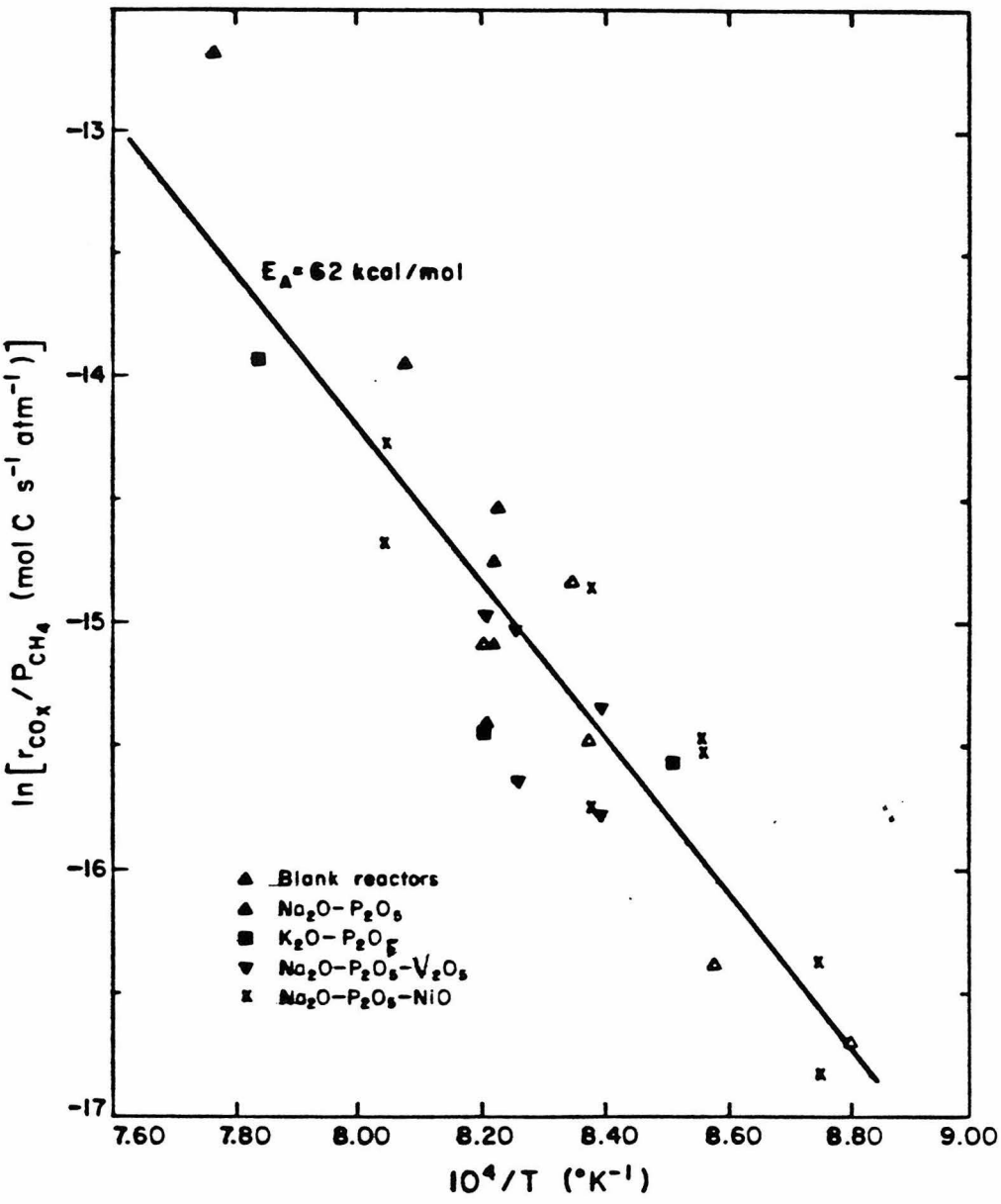

FIG. 4.2.1: CH_4 - H_2O REFORMING

TABLE 4.2.2

STEAM REFORMING OF METHANE IN BLANK ACT REACTORS

No Salt $T = 1218^{O}K$

Effect of p_{H_2O} on the rate

Run	$\dot{n}_T$(mol/s)	p_{CO} (atm)	p_{CO_2} (atm)	p_{H_2} (atm)	p_{CH_4} (atm)	p_{H_2O} (atm)	r_{CO_x} (mol C/s)	r_{CO_x}/p_{CH_4} (mol C/s/atm)	r_{CH_4}/p_{CH_4} (mol C/s/atm)
20.T3(1)	14.4×10^{-5}	.00281	.00000	.02604	.94	.0272	40.5×10^{-8}	43.0×10^{-8}	199×10^{-8}
20.T3(2)	15.0 "	.00168	.00000	.02093	.94	.0383	25.2 "	26.8 "	167 "
20.T3(3)	14.9 "	.00170	.00000	N.M.	.92	.0543	25.3 "	27.5 "	-----
20.T3(4)	17.2 "	.00089	.00000	.02158	.80	.180	15.3 "	19.1 "	232 "
20.T3(5)	22.6 "	.00031	.00000	N.M.	.62	.36	7.0 "	11.3 "	-----
20.T3(6)	48.2 "	.00012	.00000	N.M.	.34	.64	5.8 "	17.0 "	-----

N.M.: Not Measured

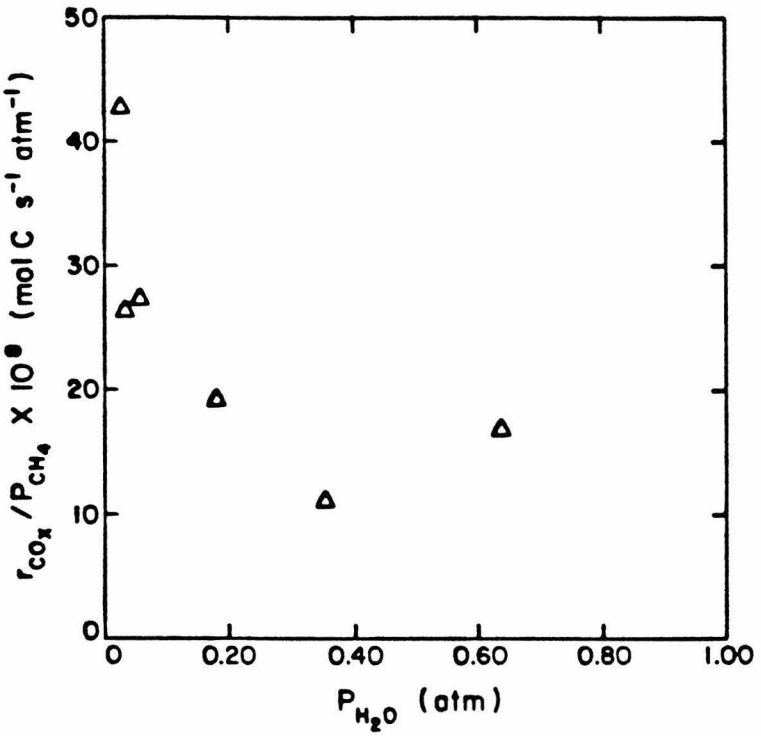

FIG. 4.2.2: CH_4 - H_2O REFORMING. EFFECT OF p_{H_2O} ON RATE OF CO_x FORMATION.
NO SALT, T = 1218°K

SECTION 4.3: STEAM REFORMING OF METHANE IN THE PRESENCE OF SODIUM PHOSPHATES

A eutectic mixture of $NaPO_3$ and $Na_4P_2O_7$ was used as a medium for the CH_4-H_2O reaction. The reactants were bubbled through the molten salt contained in a mullite ACT reactor. Table 4.3.1 presents typical conditions and product distributions for this type of system. The normalized steam reforming rate, r_{CO_x}/p_{CH_4}, is plotted vs. the temperature in Fig. 4.2.1. It can be seen that this rate is not significantly different from that observed in an empty ACT reactor.

The reaction was also carried out in a molten K_2O-P_2O_5 mixture. Data from this system are presented in Table 4.3.2. Fig. 4.6.1 includes the K_2O-P_2O_5 results, along with those from the Na_2O-P_2O_5 system. It is evident that the activity is in the same range as for the blank case.

It was concluded from this series of experiments that the catalytic activity of the surfaces of molten sodium and potassium phosphate is comparable to that of the mullite surface. Assuming similar behavior for the Na_2O-P_2O_5 systems, an activation energy of 73 kcal/mol is calculated. In view of the scatter of the data, the difference in the activation energies in the present reactor (73 kcal/mol) and in the blank reactor (65 kcal/mol) is not considered significant. The data for steam reforming tended to scatter more than the pyrolysis data because of differences in the rate of elutiation and the build-up of carbon inventory from experiment to experiment. It should be added that the absolute rate of steam methane reforming is less than

TABLE 4.3.1

STEAM REFORMING OF METHANE IN ACT REACTORS

Salt: $Na_2O-P_2O_5$ P = 1 atm.

Run	Salt Wt.(g)	T(^oK)	$\dot{n}_T$(mol/s)	$p_{CO}+p_{CO_2}$ (atm)	p_{H_2} (atm)	p_{CH_4} (atm)	p_{H_2O} (atm)	r_{CO_x} (mol C/s)	r_{CO_x}/p_{CH_4} (mol C/s/atm)
6.T3	13.9	1215	18.3×10^{-5}	.00025	.00216	.093	.90	4.6×10^{-8}	49.2×10^{-8}
7.T3	13.9	1216	20.4 "	.00016	.00173	.083	.91	3.3 "	39.3 "
21.T3(1)	16.3	1218	38.8 "	.00019	.00068	.36	.64	7.4 "	20.5 "
21.T3(2)	16.3	1218	17.3 "	.00133	.01277	.81	.19	23.0 "	28.4 "
13.T1	13.8	1237	17.6 "	.00105	.00546	.21	.79	18.5 "	88.0 "
13.T2	13.8	1287	17.2 "	.00379	.01886	.21	.78	65.2 "	310.4 "

TABLE 4.3.2

STEAM REFORMING OF METHANE IN ACT REACTORS

Salt: $K_2O-P_2O_5$ p = 1 atm

Run	Salt Wt.(g)	T(^oK)	$\dot{n}_T$(mol/s)	$p_{CO}+p_{CO_2}$ (atm)	p_{H_2} (atm)	p_{CH_4} (atm)	p_{H_2O} (atm)	r_{CO_x} (mol/s)	r_{CO_x}/p_{CH_4} mol C/s/atm)
16.T1	20.7	1175	25.3×10^{-5}	.00010	.00063	.146	.85	2.53×10^{-8}	17.3×10^{-8}
16.T2	20.7	1219	27.1 "	.00010	.00119	.137	.86	2.71 "	19.8 "
16.T4(5)	20.7	1275	21.8 "	.00067	.00761	.162	.83	14.6 "	90.2 "

the rate of methane pyrolysis because of elutriation of carbonaceous material produced by the pyrolysis.

SECTION 4.4: STEAM REFORMING OF METHANE IN THE PRESENCE OF SODIUM PHOSPHATES AND VANADIUM PENTOXIDE

Vanadium pentoxide, V_2O_5, is a well-known oxidation catalyst used commercially in sulfuric acid production (Duecker, 1959). It was thought that V_2O_5 might prove useful in methane-steam reforming by facilitating the oxidation of CH_4 or intermediate products in the pyrolysis chain.

Table 4.4.1 presents typical conditions and results for steam reforming in a melt of Na_2O-P_2O_5-V_2O_5. In Fig. 4.2.1, the normalized rate of steam reforming, r_{CO_x}/p_{CH_4}, is plotted against the reaction temperature. Comparing these results with those for the blank reactor (Section 4.2), no appreciable difference is observed. The rate of steam reforming remained the same, suggesting that V_2O_5 does not have appreciable catalytic activity. This is also confirmed by the insensitivity of the reaction rate on the amount of V_2O_5 in the reactor (reactor ACT 27 vs. reactor ACT 25). Once more, the rate of steam reforming was less than the pyrolysis rate because of elutriation. Overall, it seems that the system Na_2O-P_2O_5-V_2O_5, like the systems Na_2O-P_2O_5 and K_2O-P_2O_5, is not an active methane steam reforming catalyst.

TABLE 4.4.1

STEAM REFORMING OF METHANE IN ACT REACTORS

Salt: $Na_2O-P_2O_5-V_2O_5$ P = 1 atm.

Run	V_2O_5 Wt(g)	Total Salt(g)	T(^oK)	$\dot{n}_T$ (mol/s)	$p_{CO}+p_{CO_2}$ (atm)	p_{H_2} (atm)	p_{CH_4} (atm)	p_{H_2O} (atm)	r_{CO_x} (mol C/s)	r_{CO_x}/p_{CH_4} (mol C/s/atm)
27.T1(2)	5.1	20.7	1192	3.8×10^{-5}	.00330	.0842	.89	.0250	12.5×10^{-8}	14.1×10^{-8}
27.T1(9)	5.1	20.7	1192	6.5 "	.00188	.0137	.56	.42	12.2 "	21.8 "
25.T3(1)	1.95	17.5	1210	14.4 "	.00107	.00412	.96	.03	15.4 "	16.1 "
25.T3(2)	1.95	17.5	1210	16.5 "	.00153	.00589	.84	.15	25.2 "	30.1 "
27.T2(2)	5.1	20.7	1218	12.3 "	.00045	.0118	.29	.70	5.5 "	19.1 "

SECTION 4.5: STEAM REFORMING OF METHANE IN THE PRESENCE OF SODIUM PHOSPHATES AND NICKEL OXIDE

The traditional methane steam reforming catalyst is nickel supported on alumina pellets (Bodrov, 1964, Ross, 1973). In this set of experiments, nickel oxide, NiO, was added to the Na_2O-P_2O_5 molten salt bath. The intent was to study the activity of NiO dissolved in the salt bath, as well as the activity of metallic Ni particles suspended in the bath.

Table 4.5.1 lists conditions and results for methane steam reforming experiments in the Na_2O-P_2O_5-NiO system. The designation NaO-P_2O_5-NiO includes the case of NiO dissolved in the melt (oxidizing atmosphere) and the case of metallic Ni suspended in the melt (reducing atmosphere). Fig. 4.5.1 is a graphic representation of the normalized rate, r_{CO_x}/p_{CH_4}, vs. the temperature.

The experimental points cluster in two groups corresponding to high and low rates. The large difference indicates a drastic change in the form of the nickel component: the low rate indicating a relatively oxidizing atmosphere with the nickel present in oxide form, the high rate indicating a relatively reducing one whereby the nickel is present in metallic form. Evidence for this behavior will be presented in Chapter 5.

Under oxidizing conditions, NiO is dissolved in the melt of Na_2O-P_2O_5 (See subsection 5.2.2). The activity of this melt, Na_2O-P_2O_5-NiO, is not significantly different from the activity of the previously examined melts or that of the blank reactor.

The reduced Na_2O-P_2O_5-NiO system catalyzes the reaction as it can be expected for a system containing metallic Ni. This

TABLE 4.5.1

STEAM REFORMING OF METHANE IN ACT REACTORS

Salt: $Na_2O-P_2O_5-NiO$ P = 1 atm.

Run	NiO Wt(g)	Total Salt(g)	T(^oK)	$\dot{n}_T$ (mol/s)	$p_{CO}+p_{CO_2}$ (atm)	p_{H_2} (atm)	p_{CH_4} (atm)	p_{H_2O} (atm)	r_{CO_x} (mol C/s)	r_{CO_x}/p_{CH_4} (mol C/s/atm)
38.T1(4)	.49	13.3	1143	11.9×10^{-5}	.00020	.00080	.31	.69	2.38×10^{-8}	7.7×10^{-8}
38.T1(5)	.49	13.3	1143	6.8 "	.00040	.00140	.54	.46	2.72 "	5.0 "
38.T1(8)	.49	13.3	1143	4.0 "	.01900	.05780	.90	.06	76.0 "	84.0 "
38.T2(1)	.49	13.3	1168	8.2 "	.00130	.00460	.55	.45	10.7 "	19.4 "
38.T2(4)	.49	13.3	1168	7.6 "	.00120	.00420	.49	.51	9.1 "	18.6 "
38.T2(5)	.49	13.3	1168	4.5 "	.04060	.12180	.79	.13	183.0 "	231.0 "
37.T1(1)	.40	13.2	1193	6.3 "	.00330	.0137	.58	.42	20.8 "	35.8 "
37.T1(2)	.40	13.2	1193	16.1 "	.00020	.00070	.22	.77	3.22 "	14.6 "
37.T1(4)	.40	13.2	1193	4.7 "	.05130	.1638	.73	.165	241.0 "	330.0 "
37.T1(6)	.40	13.2	1193	5.0 "	.03580	.1351	.70	.22	179.0 "	256.0 "
36.T1(1)	.38	13.3	1243	16.6 "	.00319	.01117	.84	.16	53.0 "	63.0 "
36.T1(2)	.38	13.3	1243	24.9 "	.00095	.00333	.56	.44	23.7 "	42.2 "
36.T1(3)	.38	13.3	1243	15.7 "	.01230	.04330	.89	.10	193.0 "	217.0 "

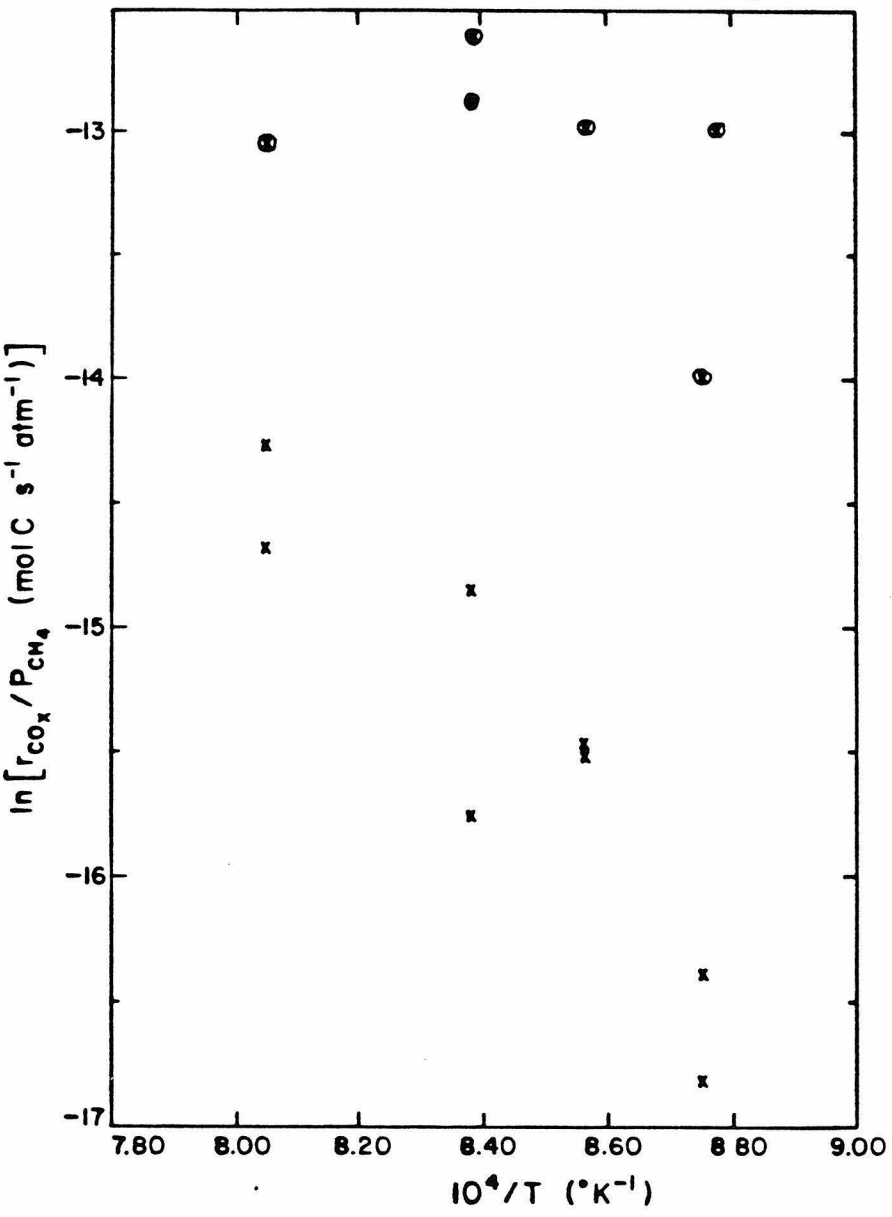

FIG. 4.5.1: CH_4 - H_2O REFORMING

SALT: Na_2O - P_2O_5 - NiO

⊗ : LOW p^oH_2O

x : HIGH p^oH_2O

new, molten salt system has the novel feature of carrying the Ni catalyst in suspension.

SECTION 4.6: CONCLUSIONS

Fig. 4.2.1 summarizes the results of methane steam reforming in these different systems:

- Blank ACT reactors
- the Na_2O-P_2O_5 system
- the K_2O -P_2O_5 system
- the Na_2O-P_2O_5-V_2O_5 system, and
- the Na_2-P_2O_5-NiO system under oxidizing conditions.

The difference among the various systems is small and none can be considered as a catalyst for methane steam reforming. Combining these data for the purpose of obtaining an activation energy leads to E_a = 62 kcal/mol, close to the activation energy of CH_4 pyrolysis. This value suggests pyrolysis as the rate-controlling step in steam reforming. However, because coke and various hydrocarbons are carried with the product steam, the amount of carbon oxides formed is lower than the amount of methane consumed.

When the reactor atmosphere is reducing, the Na_2O-P_2O_5-NiO system does show high activity. This is an interesting and novel application of a Ni catalyst in a molten salt environment. An important consideration in this case is the critical steam to methane, or steam to hydrogen, ratio necessary to establish reducing conditions. The activity due to metallic nickel particles is subject to transient conditions as these particles form out of the Na_2O-P_2O_5-NiO melt and as they subsequently slowly agglomerate. These questions are examined in a more detailed study of the Na_2O-P_2O_5-NiO systems described in Chapter 5.

CHAPTER FIVE

DETAILED STUDY OF THE $Na_2O-P_2O_5-NiO$ SYSTEM

GENERAL

A detailed study of methane steam reforming in the presence of Na_2O-P_2O_5-NiO was carried out in Annular Crucible and Tube (ACT) reactors. The salt loadings of different reactors were presented in Table 4.1.1.

The rate of CH_4 pyrolysis was not significantly affected by the presence of Ni in the reactor. Passing CH_4 with no steam over the Ni-containing melt, as in Run 19.3, Table 3.3.7, resulted in no appreciable increase in the rate of CH_4 cracking. However, the rate of the CH_4-H_2O reaction was greatly affected by the NiO addition to the molten salt bath, as it is indicated by the CH_4-H_2O data presented in Section 4.5. The activity was high at low steam fractions, while at high steam fractions, the activity was comparable to that of the sodium phosphate melt or of the empty annular reactor.

By examining the glass formed by cooling the melt to room temperature, it was observed that metallic Ni was formed at low steam fractions. Metallic nickel was not evident at high steam fractions. Nickel is solid at the reaction temperatures (800°-1000°C vs. m.p. of nickel at 1453°C). This explains the high rate of the methane steam reforming reaction at low steam fractions.

The transient behavior of this system, i.e., the manner of nickel particle formation and dissolution in the melt, is examined in this chapter. Some results are also presented concerning the state of nickel deposits obtained by X-ray diffraction and electron microprobe analysis. The dependence of the rate

on operating variables, such as amount of nickel in the reactor, reactor atmosphere (reducing vs. oxidizing) and temperature is also examined.

SECTION 5.1: RATE TRANSIENTS

5.1.1 Procedure

An important aspect of the system Na_2O-P_2O_5-NiO is the transition between the oxidized and the reduced states of nickel. In the experiments described in the present section, the melt was formed by mixing NiO powder and granular $NaPO_3$ and $Na_4P_2O_7$, and adding the mixture to the reactor crucible. As the temperature was raised above the melting point of the sodium phosphate salts (above 550°C), the NiO dissolved in the molten glass (m.p. of NiO: 1990°C). A quantitative analysis of the glasses after the experiments (see subsection 5.2.2) indicated that NiO dissolves into the glass even at the higher loadings. However, a small amount of NiO could remain undissolved because of poor contacting (no stirring or bubbling during dissolution). To explain the observed transient behavior, this undissolved NiO had to be taken into account.

After the desired temperature had been reached, a flow of air was started to oxidize any organic matter in the reactor (See also Section 3). Steam was then added to the air at a specified partial pressure. The flow of air was subsequently replaced by a flow of N_2, and then of CH_4, starting a period of CH_4 and steam flow. If the steam mole fraction was sufficiently high, NiO was kept oxidized. For "first reduction" experiments the steam fraction was set low, so that NiO was reduced by the reducing gases in the reactor, e.g. CH_4 and H_2. The rate of CO_x formation was monitored and the experiment continued until the rate stabilized. Such a reduced reactor could be oxidized

by increasing the steam mol fraction. More reduction/oxidation cycles could then follow. Rate transients were again monitored until a steady-state was achieved.

5.1.2 Results

Figures 5.1.1, 5.1.2 and 5.1.3 show the behavior of the rate of CO_x evolution from reactors exposed to a reducing atmosphere for the first time. At first there is a short-term increase in the rate to a short-lived maximum. (Note: The figures do not discount the transport lag from the reactor to the IR instrument measuring CO and CO_2; the lag is about 5-15 minutes). This maximum is attributed to undissolved NiO, easily available for reduction by CH_4 to CO and CO_2. As this mass is quickly reduced, the rate drops. However, the rate starts increasing again as dissolved NiO reaches the gas-liquid interface where it is reduced and starts catalyzing the reaction as solid metallic Ni. Therefore, the rate increases to a new, higher maximum. In the cases of Figs. 5.1.1 and 5.1.3, this maximum is followed by a slow decline to a steady-state. In the case of Fig. 5.1.2, this arrival at a steady-state by way of a slow decline is not as clear, although it could be present. The decline in the rate is evidence of agglomeration of Ni particles. After NiO has been reduced to finely divided solid Ni, these Ni particles agglomerate by a process of sintering at the high reaction temperatures. This agglomeration results in a decreased surface area and reaction rate.

If a reactor in a reduced state were to be exposed to an oxidizing gas, Ni would be oxidized and the activity would be

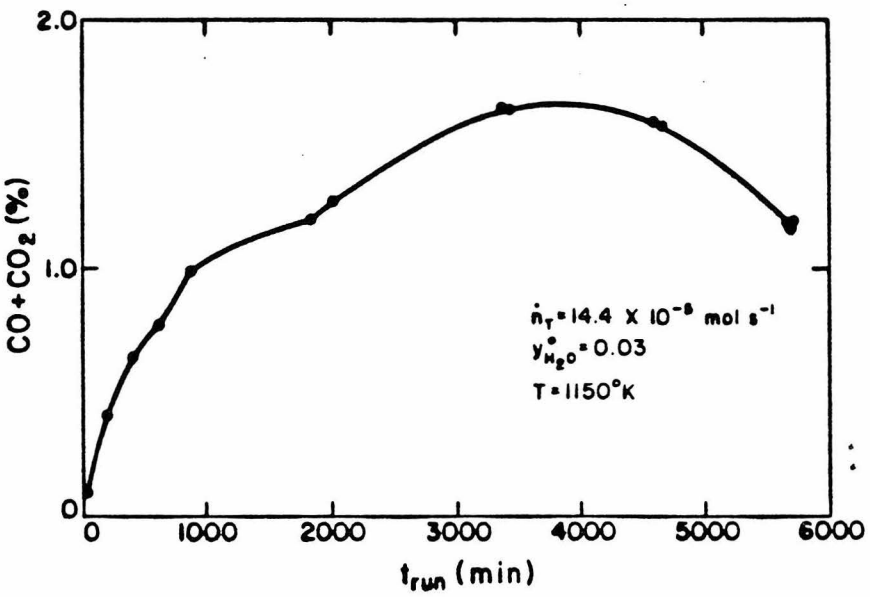

FIG. 5.1.1: FIRST REDUCTION OF CATALYST

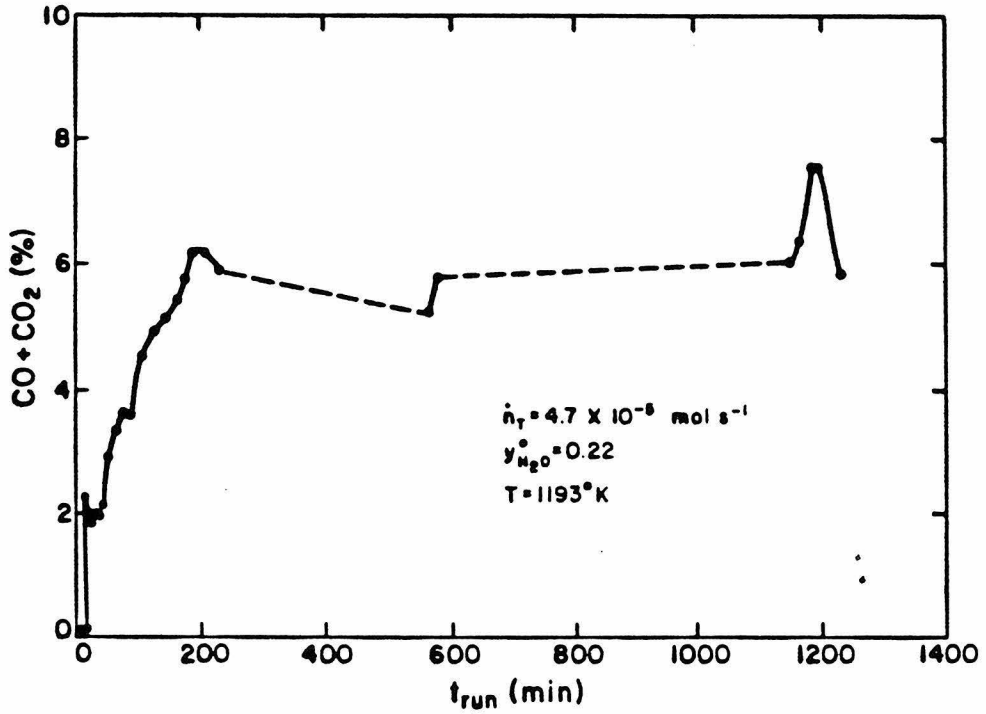

FIG. 5.1.2: FIRST REDUCTION OF CATALYST

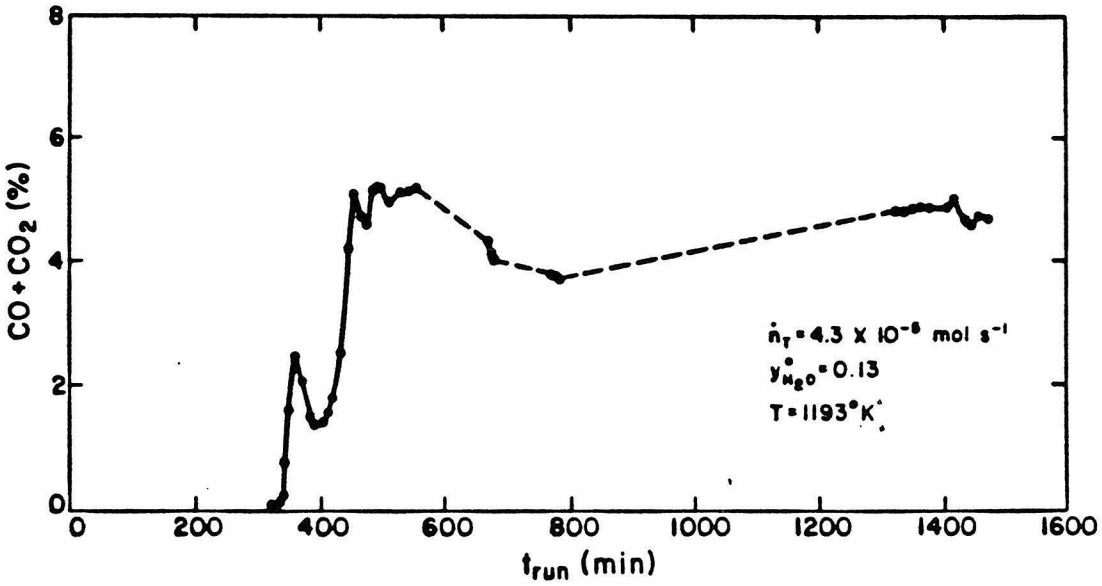

FIG. 5.1.3: FIRST REDUCTION OF CATALYST

decreased. If the contact between the melt and the newly formed NiO is good, NiO will again dissolve in the melt. However, if contact is not good, a large part of NiO would remain undissolved. The "second" or later reduction of a reactor is shown in Fig. 5.1.4. Here, the rate declines to a steady-state. This is because in the reactors used, the contacting between melt and NiO was not always good. The NiO mass is exposed and easily available for reduction by the gas, leading to CO_x formation.

5.1.3 Analysis of Transient Behavior

To quantify the transient behavior of CO_x evolution, let it be assumed that the amount of NiO originally in the reactor, W^o_{NiO}, is divided into two portions:

(a) W^{os}_{NiO}, originally dissolved in the melt, and

(b) W^{ow}_{NiO}, originally undissolved and attached to the walls of the reactor.

Let the rate constants of reduction of these portions be k_{1_s} and k_{1_w}(mol C/(s·atm·gNiO))respectively and the rate constant of steam-methane reforming on metallic Ni be k_{Ni} (mol C/(s·gNi·atm)) and let the rate of CO_x formation in the absence of NiO at these conditions be $\left[r_{CO_x}\right]_{BASE}$ (mol C/s). Then, the rate of CO_x evolution at any time, t, is:

$$r_{CO_x} = \left(k_{1s} W^s_{NiO} + k_{1w} W^w_{NiO}\right) p_{CH_4} + k_{Ni} W_{Ni} p_{CH_4} + \left[r_{CO_x}\right]_{BASE} \quad (5.1.1)$$

where W_{Ni} is the amount of solid metallic Ni at any time (see Section 5.3 for this dependence). The differential equations and initial conditions are as follows:

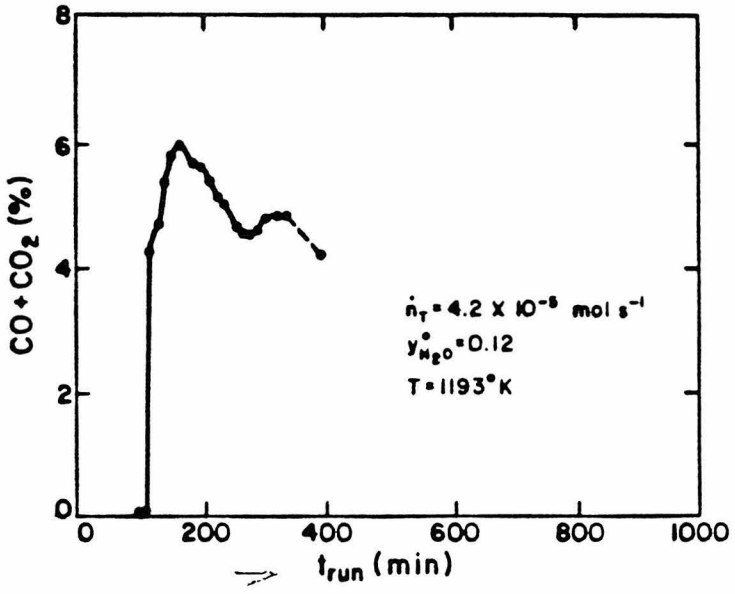

FIG. 5.1.4: SECOND REDUCTION OF CATALYST

$$\frac{d(W^s_{NiO})}{dt} = -\nu k_{1s} W^s_{NiO} p_{CH_4} \quad , \quad W^s_{NiO} = W^{os}_{NiO} \text{ at } t = 0 \qquad (5.1.2)$$

$$\frac{d(W^w_{NiO})}{dt} = -\nu k_{1w} W^w_{NiO} p_{CH_4} \quad , \quad W^w_{NiO} = W^{ow}_{NiO} \text{ at } t = 0 \qquad (5.1.3)$$

and

$$\frac{d(W_{Ni})}{dt} = \{\nu k_{1s} W^s_{NiO} + \nu k_{1w} W^w_{NiO}\} \frac{MW(Ni)}{MW(NiO)} p_{CH_4}, W_{Ni}=0 \text{ at } t=0 \qquad (5.1.4)$$

where the rates were taken as first order and ν is a stoichiometric constant relating changes in NiO and CO_x. Integrating equations (5.1.2), (5.1.3) and (5.1.4) we obtain:

$$W^s_{NiO} = W^{os}_{NiO} \exp\left(-\nu\, k_{1s} p_{CH_4}\, t\right) \qquad (5.1.5)$$

$$W^w_{NiO} = W^{ow}_{NiO} \exp\left(-\nu\, k_{1w} p_{CH_4}\, t\right) \qquad (5.1.6)$$

$$W_{Ni} = (W^{os}_{NiO} + W^{ow}_{NiO}) \frac{MW(Ni)}{MW(NiO)} - \left(W^{os}_{NiO} \exp(-\nu k_{1s} p_{CH_4} t) + W^{ow}_{NiO} \exp(-\nu k_{1w} p_{CH_4} t)\right) \frac{MW(Ni)}{MW(NiO)} \qquad (5.1.7)$$

These results are combined to provide the following expression for the rate of CO_x formation:

$$r_{CO_x} = \left(r_{CO_x}\right)_{BASE} + k_{Ni} p_{CH_4} \left(W^{os}_{NiO} + W^{ow}_{NiO}\right) \frac{MW(Ni)}{MW(NiO)} + W^{os}_{NiO} \left(k_{1s} - k_{Ni} \frac{MW(Ni)}{MW(NiO)}\right) \exp(-\nu k_{1s} p_{CH_4} t) + W^{ow}_{NiO} \left(k_{1w} - k_{Ni} \frac{MW(Ni)}{MW(NiO)}\right) \exp(-\nu k_{1w} p_{CH_4} t) \qquad (5.1.8)$$

As $t \to \infty$, r_{CO_x} reaches a steady-state given by the sum of the first two terms; the transient behavior arises because of the last two terms. The approach to the steady-state can occur in several different modes according to the values of the parameters. Appendix III contains a further discussion and analysis of the transient behavior.

SECTION 5.2: CATALYST ANALYSES

After carrying out a series of experiments, each reactor was cooled to room temperature and the frozen salt was saved. The material was separated by breaking it into fragments and selecting specimens according to appearance with the help of a microscope. The specimens fell into distinct categories:

- Amorphous glass (mostly sodium phosphates)
- Crystalline salt matter (nickel oxides and salts, recrystallized sodium phosphates),
- Metallic Ni deposits.

From some reactors, more than one sample were taken to examine composition variations at different parts of the reactor caused, for example, by segregation of metal nickel. Analyses were performed to determine the chemical composition and the crystalline structure of these different specimens. It was especially interesting to determine the particle size of of any metallic Ni present in the phosphate glass. Metallic Ni was found on the reactor walls just above the salt bath, or in the salt bath, as spongy clusters of a few millimeters in size. These were presumably built up from smaller particles formed during the process of first reduction of NiO from the sodium phosphate melt. Thus, smaller particles were expected to be found in the glass specimens.

The analyses used were X-ray diffraction (XRD) to determine the crystalline structure of the specimens, and electron microprobe analysis. Polished sections of glasses were examined with an electron microprobe to determine quantitative chemical

composition. Other glass specimens were also examined with an electron microprobe to identify microstructures and their qualitative chemical composition.

5.2.1 X-Ray Diffraction Study of Catalysts

Powder X-ray crystallography was used to identify the crystalline structure of starting phosphate salts and of different specimens collected from various reactors. The X-ray source was CuK_{α}, λ = 1.542 Å at 45 kV, 16 mA, with a Ni filter.

Figures 5.2.1 and 5.2.2 are analyses of starting materials. Fig. 5.2.1 shows that the sodium pyrophosphate used contained $Na_4P_2O_7 \cdot 10H_2O$ and $Na_4P_2O_7 \cdot 2H_2O_2 \cdot 8H_2O$(McClune, 1978). Many other peaks appear, presumably belonging to other crystalline forms of hydrated sodium polyphosphates. Fig. 5.2.2 shows that the sodium metaphosphate used was amorphous as expected of the straight-chain polymeric $(NaPO_3)_n$ forms (See Section 2.1). Fig. 5.2.3 shows the X-ray diffraction pattern of a sodium phosphate glass specimen left to recystallize for months at room temperature. During this period, its appearance had changed from that of a clear,colorless glass to that of an opaque, white, crystalline matter. The X-ray pattern shows the presence of many sodium phosphate forms.

Fig. 5.2.4 presents the XRD analysis of glass from reactor ACT 32. This reactor had been reduced and oxidized many times; its final treatment was air oxidation at reaction temperatures. The pattern shows no crystalline structure, indicating a uniformly amorphous glass. The electron microprobe analysis of

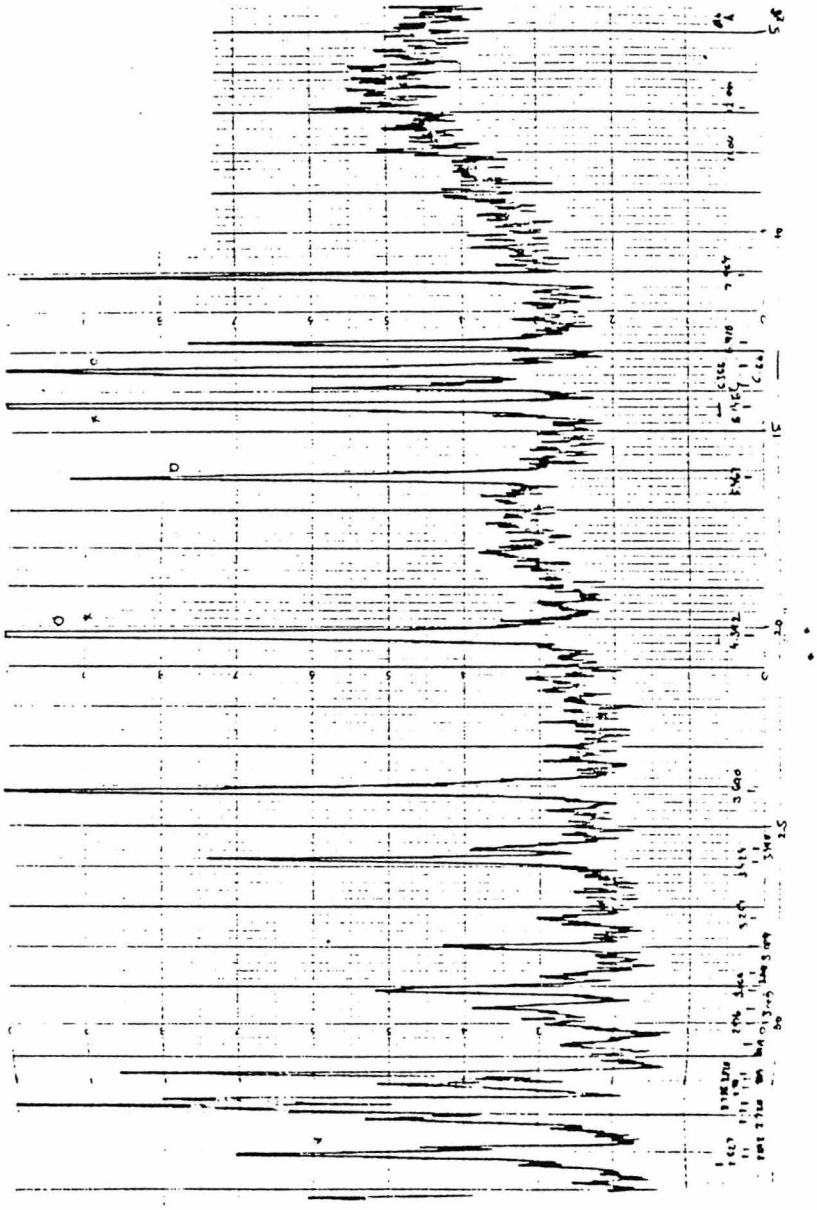

FIG. 5.2.1: XRD ANALYSIS OF SODIUM PYROPHOSPHATE (STARTING MATERIAL). $Na_4P_2O_7 \cdot 10H_2O$ AND $Na_4P_2O_7 \cdot 2H_2O_2 \cdot 8H_2O$ PRESENT.

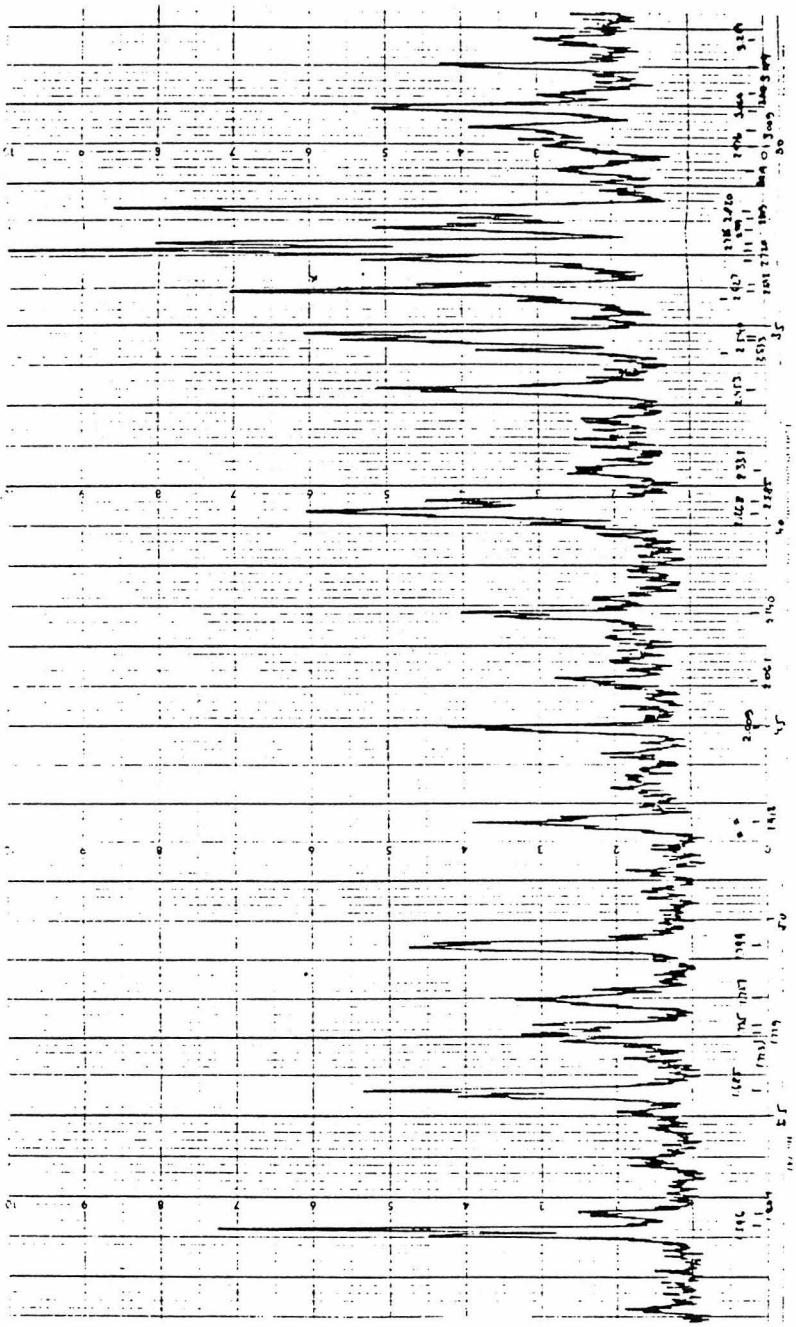

FIG. 5.2.1: CONTINUED

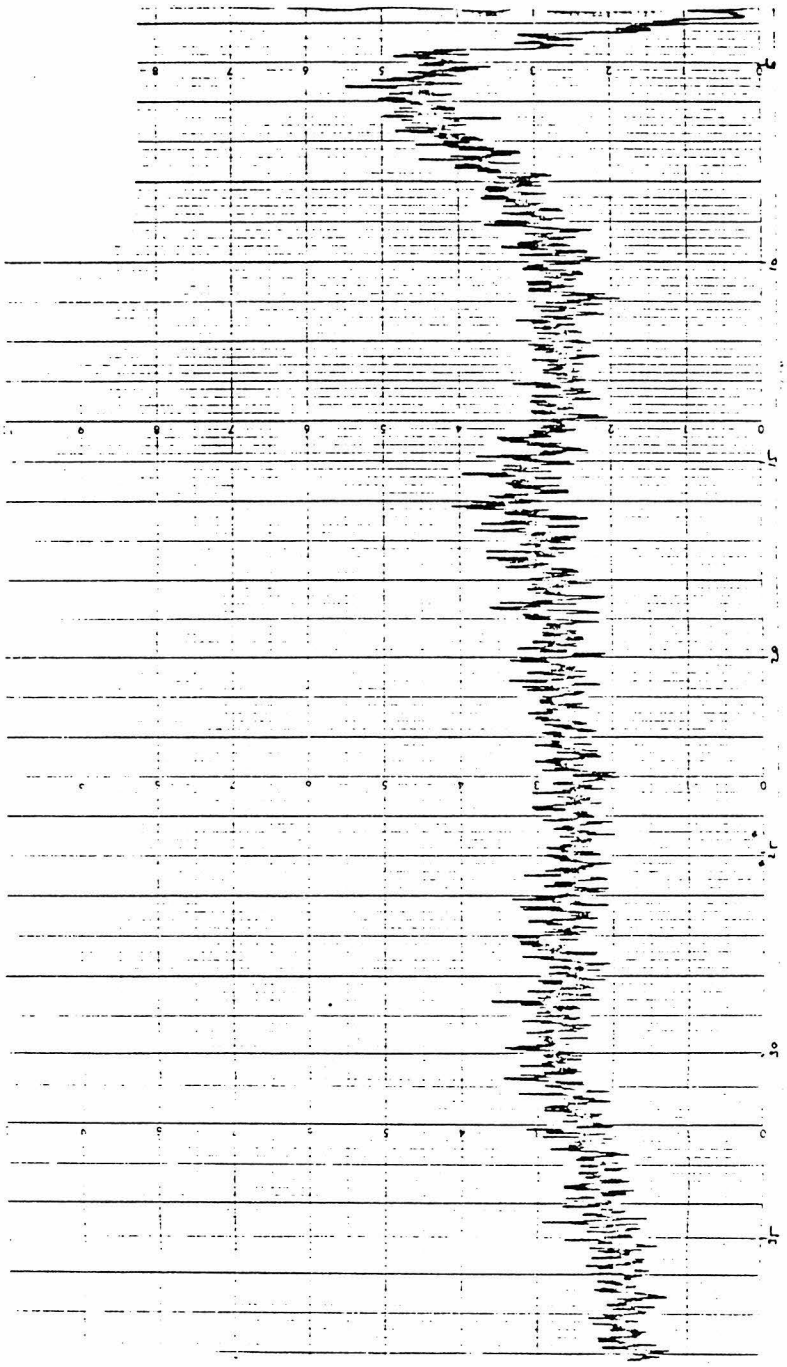

FIG. 5.2.2: XRD ANALYSIS OF SODIUM METAPHOSPHATE (STARTING MATERIAL). AMORPHOUS.

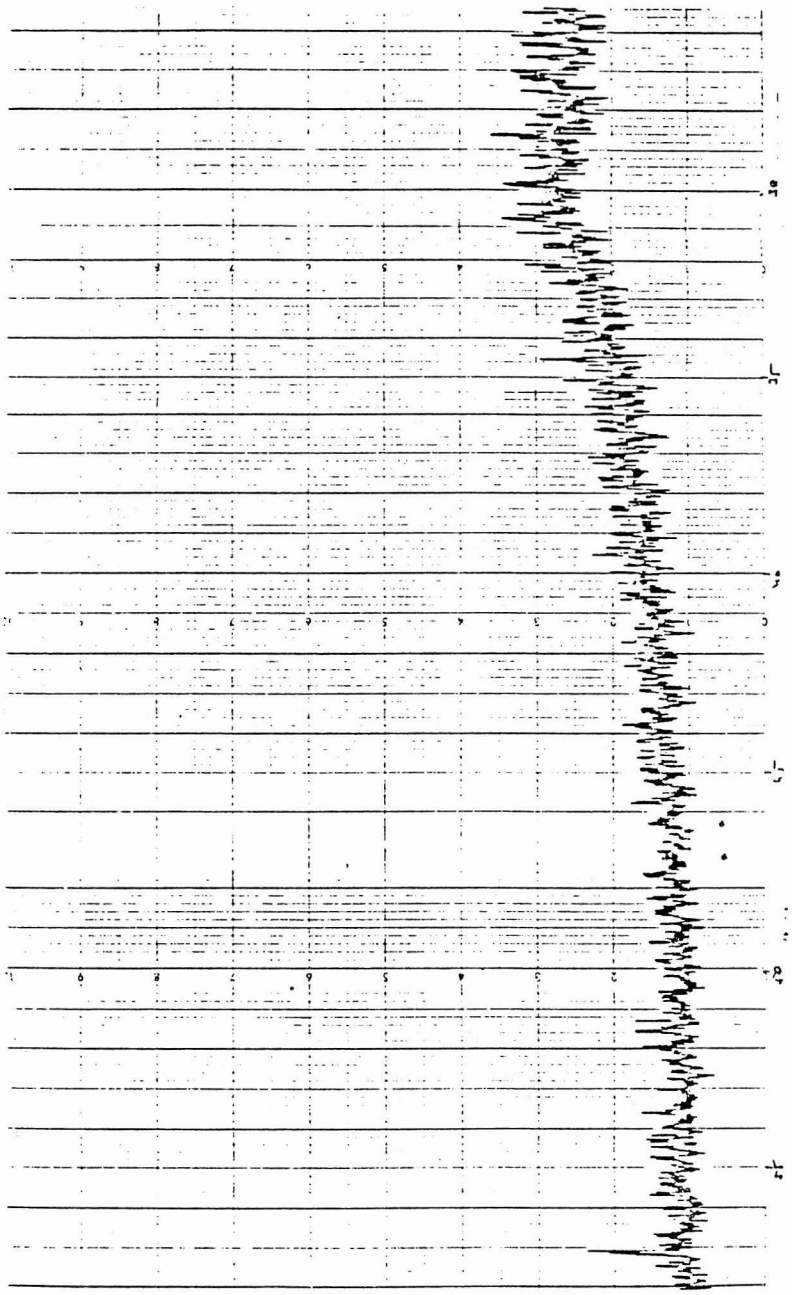

FIG. 5.2.2: CONTINUED

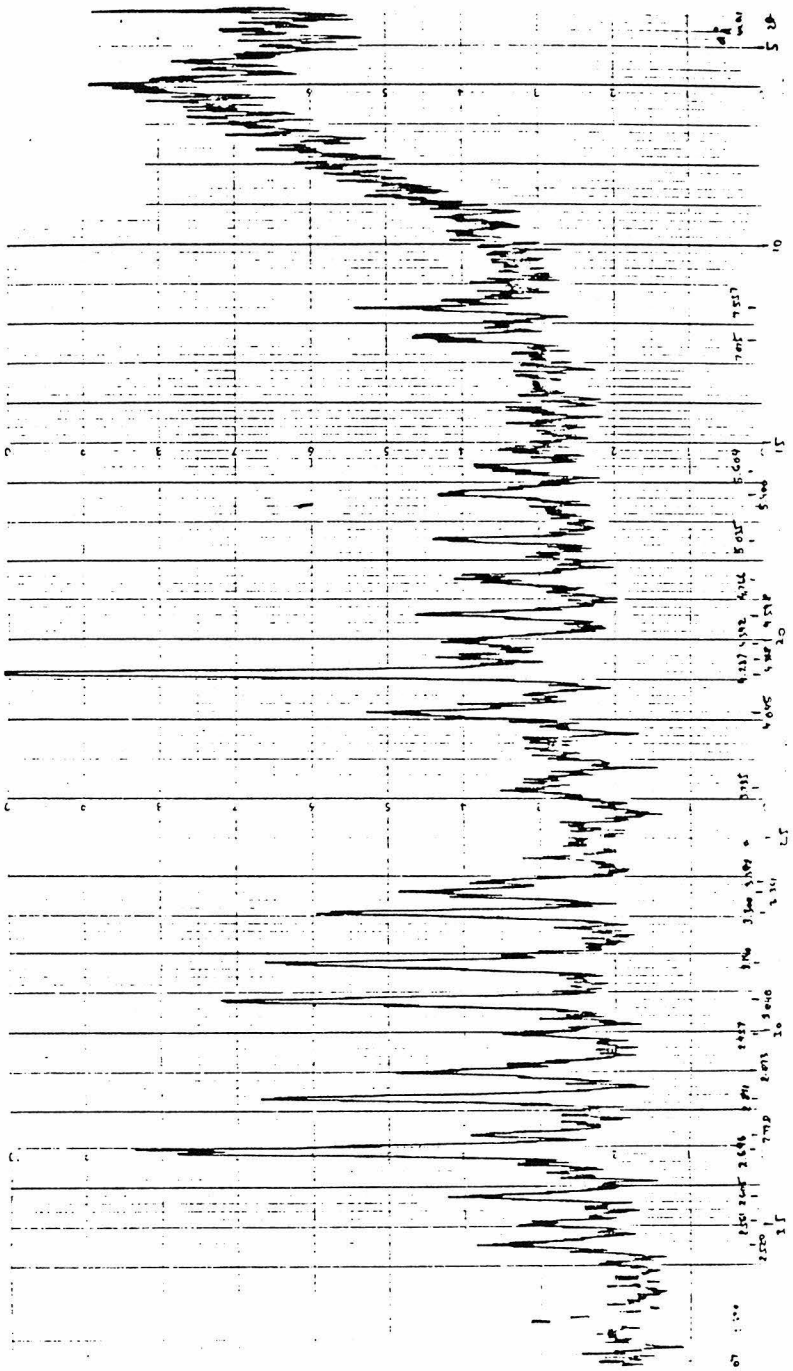

FIG. 5.2.3: XRD ANALYSIS OF RECRYSTALLIZED Na_2O-P_2O_5 GLASS.

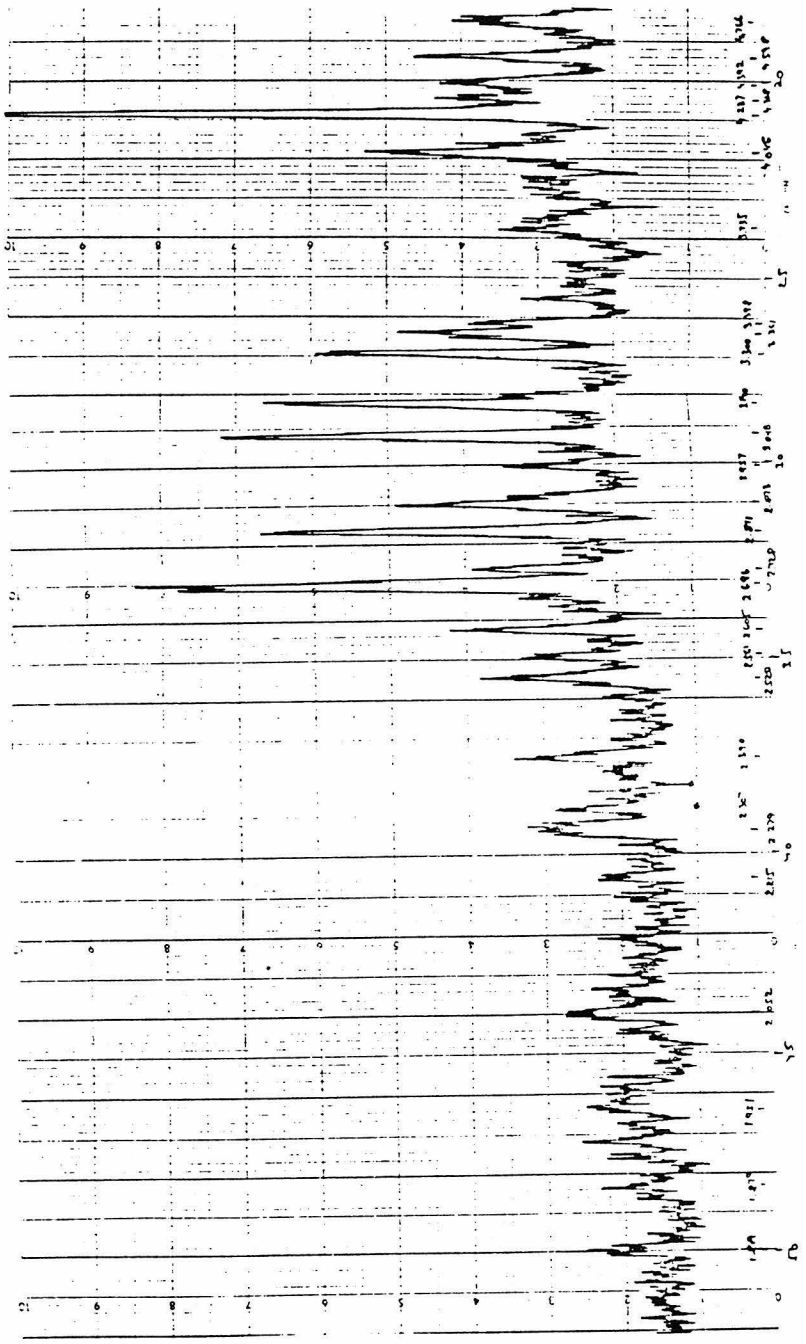

FIG. 5.2.3: CONTINUED

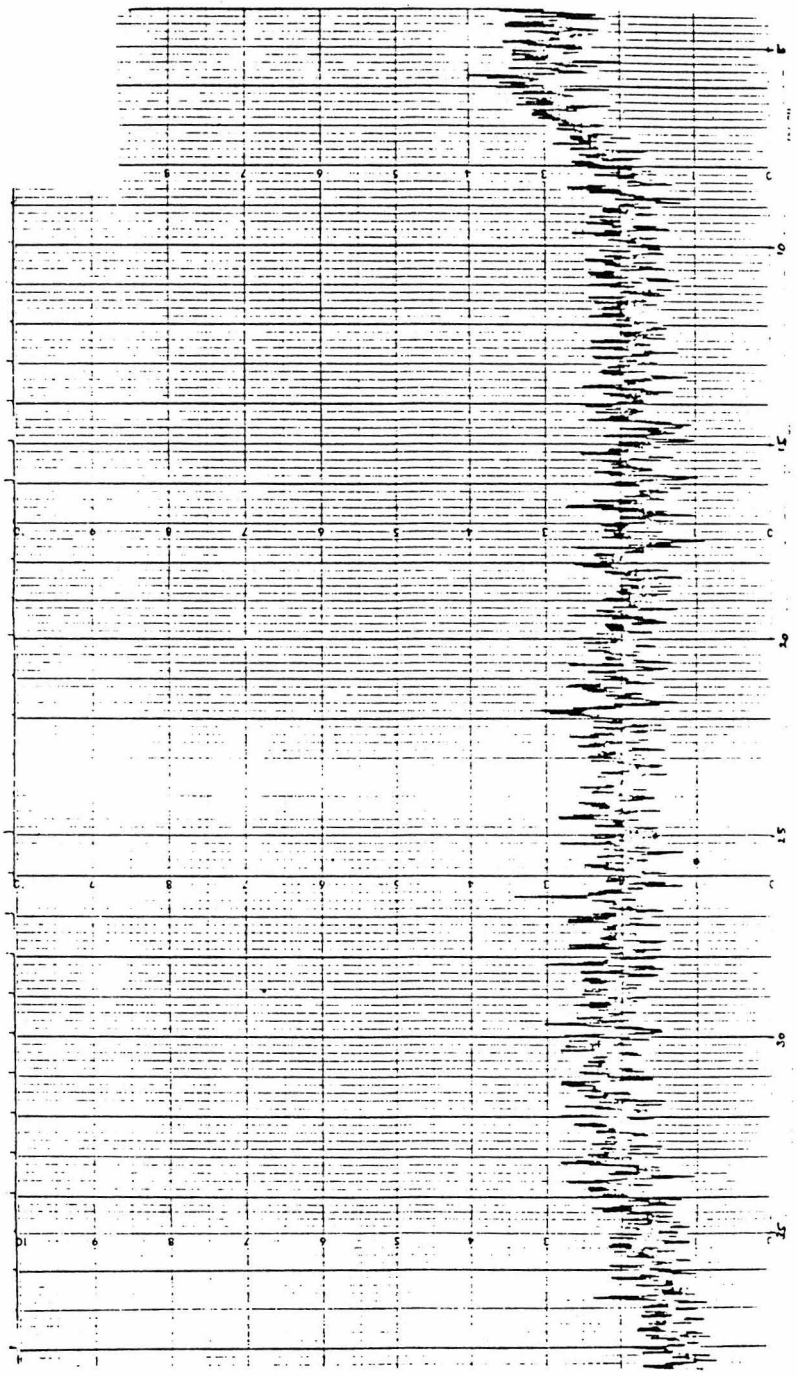

FIG. 5.2.4: GLASS FROM REACTOR ACT 32 (OXIDIZED). AMORPHOUS.

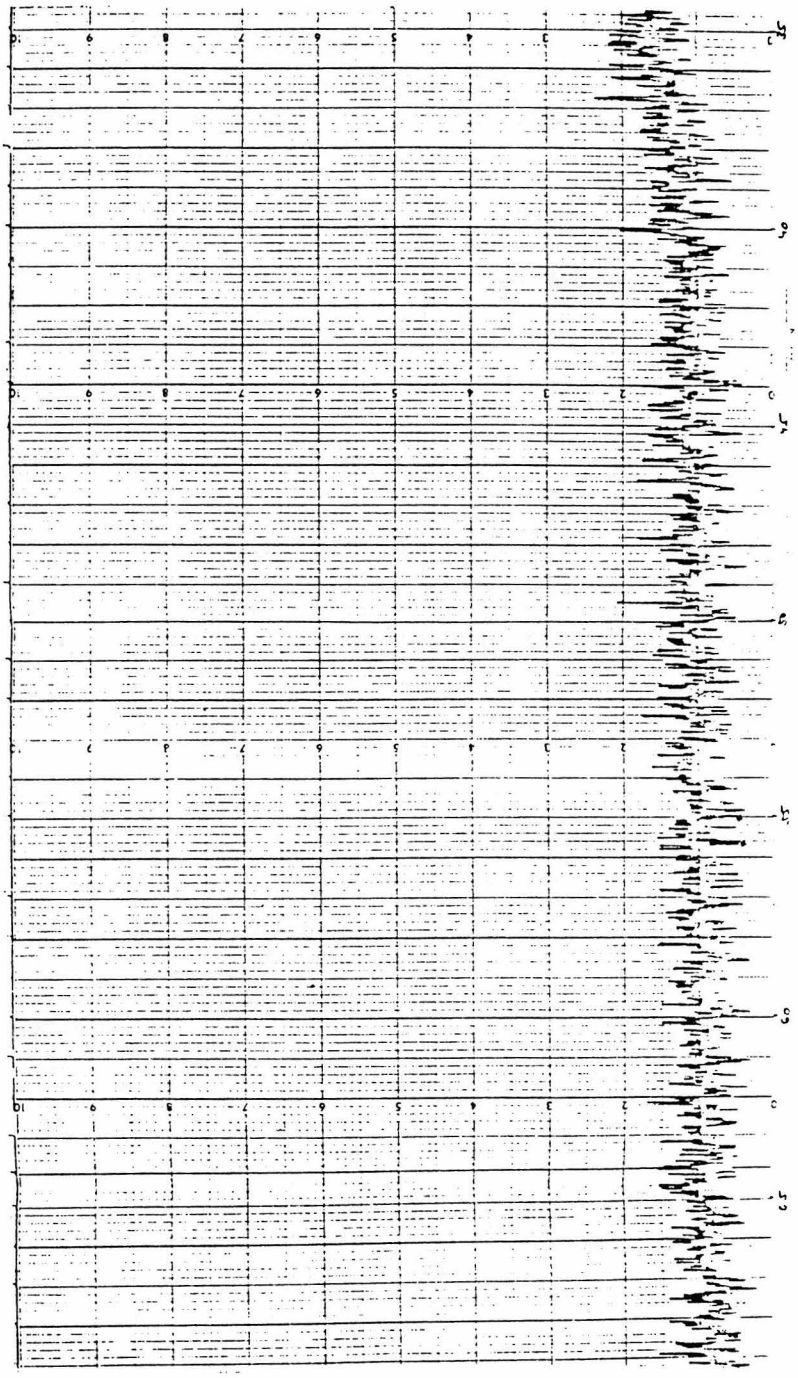

FIG. 5.2.4: CONTINUED.

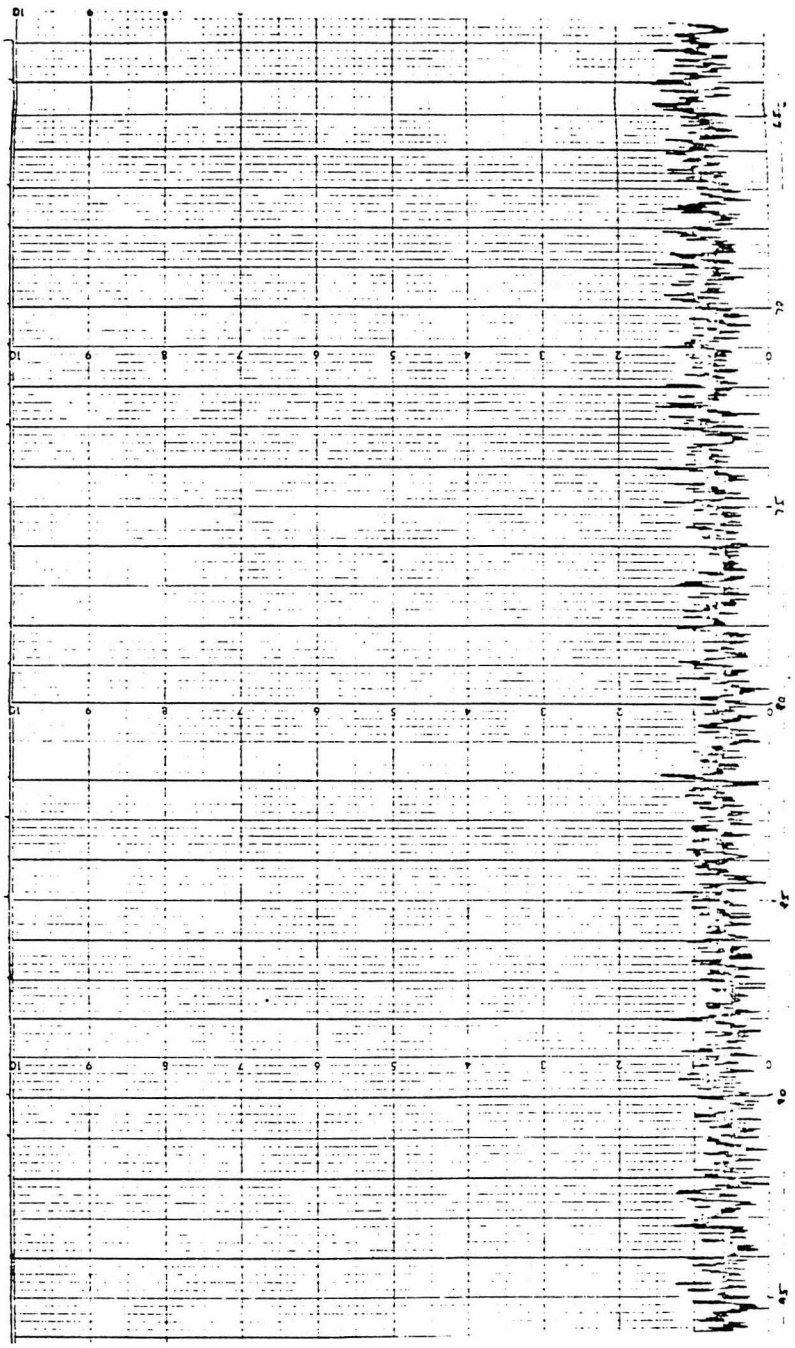

FIG. 5.2.4: CONTINUED.

this sample indicates an average NiO content of 16.7% by weight. (See subsection 5.2.2) versus 17.7% at preparation (Table 4.1.1). The close agreement in the nickel content indicates the high solubility of nickel and the effective contact between melt and oxidized nickel particles.

Fig. 5.2.5 is the analysis of a glass sample from reactor ACT 31. After a series of oxidation-reduction cycles during the steam reforming experiments, this reactor was reduced by a flow of H_2. The pattern is generally amorphous, corresponding to the glass, with two small peaks at λ = 2.028Å and λ=1.755Å corresponding to metallic Ni (McClune, 1978). The metallic nickel crystallites were evidently suspended in the glass following their formation during the reduction of dissolved NiO. The metallic Ni crystallites were also found in the electron microprobe analysis of this sample (See subsection 5.2.3).

Fig. 5.2.6 presents the analysis of Ni deposits from reactor ACT 31. As it was mentioned before, this reactor was last contacted by a stream of hydrogen. The Ni lines are quite strong, at λ=2.034Å, λ=1.762Å, λ=1.246Å, λ=1.046Å and λ=1.017Å, since they come from macroscopic Ni deposits. These deposits are the final step in the agglomeration of small crystallites resulting from NiO reduction from the salt. Their size is about 5mm.

Fig. 5.2.7 presents the analysis of mixed crystalline matter and glass from reactor ACT 30 which had been reduced and then oxidized. The oxidized sample was taken from the bottom of the reactor crucible where agitation is poor and redissolu-

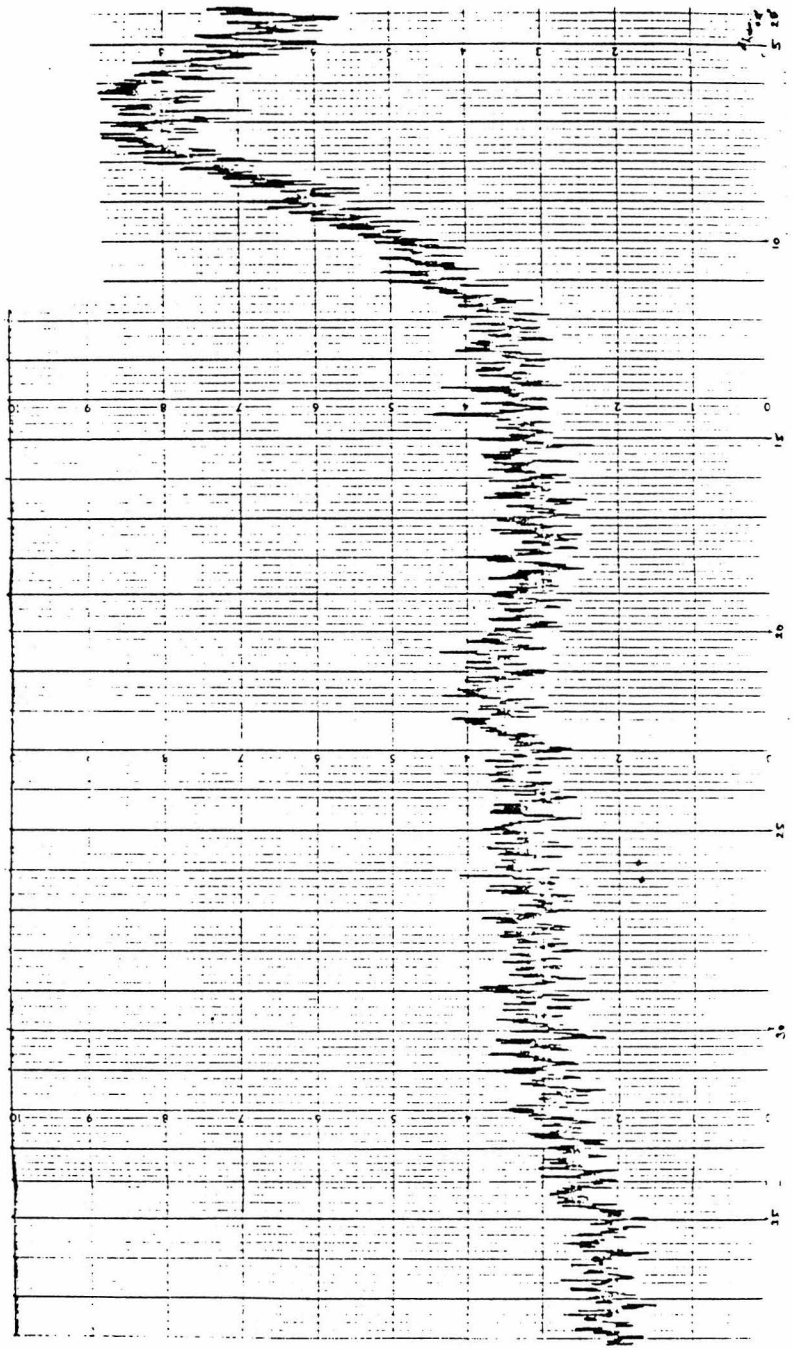

FIG. 5.2.5: GLASS FROM REACTOR ACT 31 (REDUCED). AMORPHOUS GLASS AND CRYSTALLINE Ni.

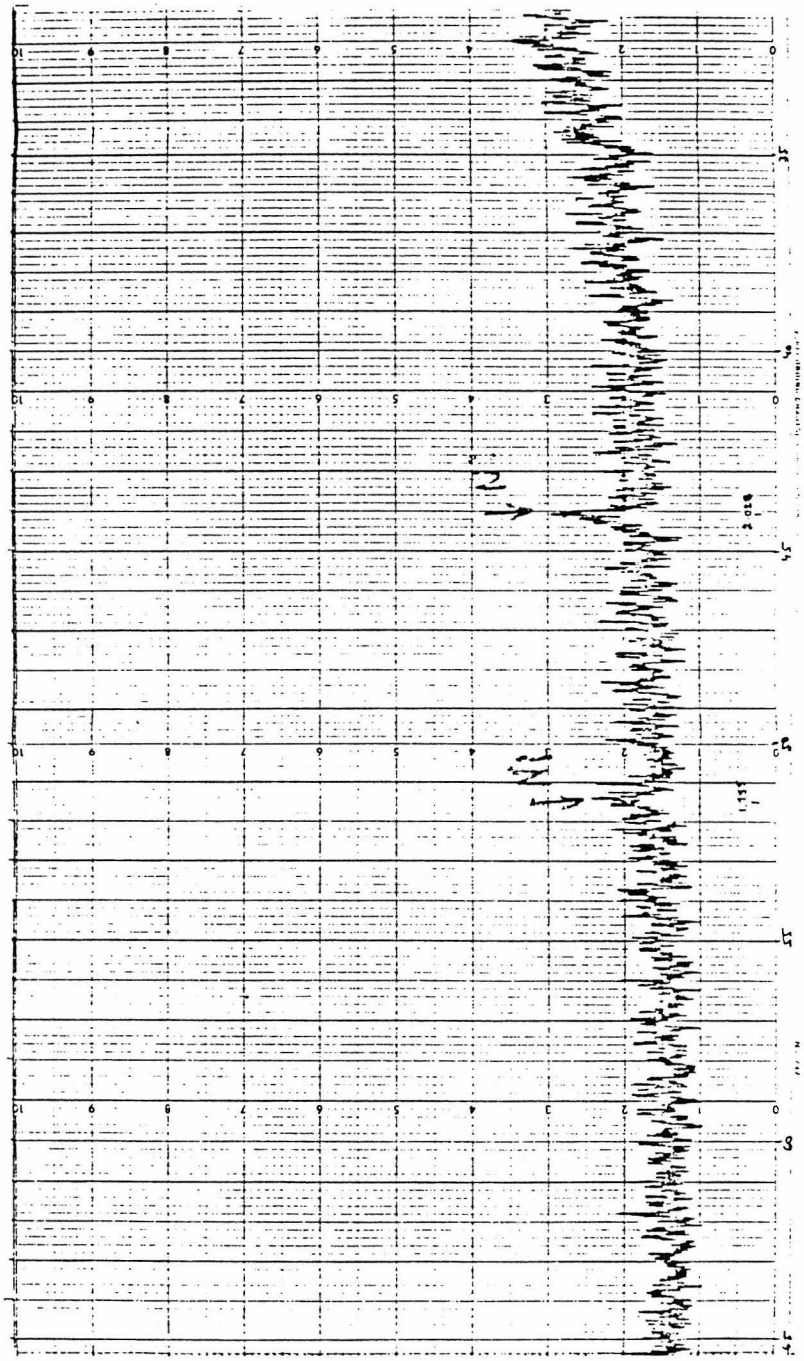

FIG. 5.2.5: CONTINUED.

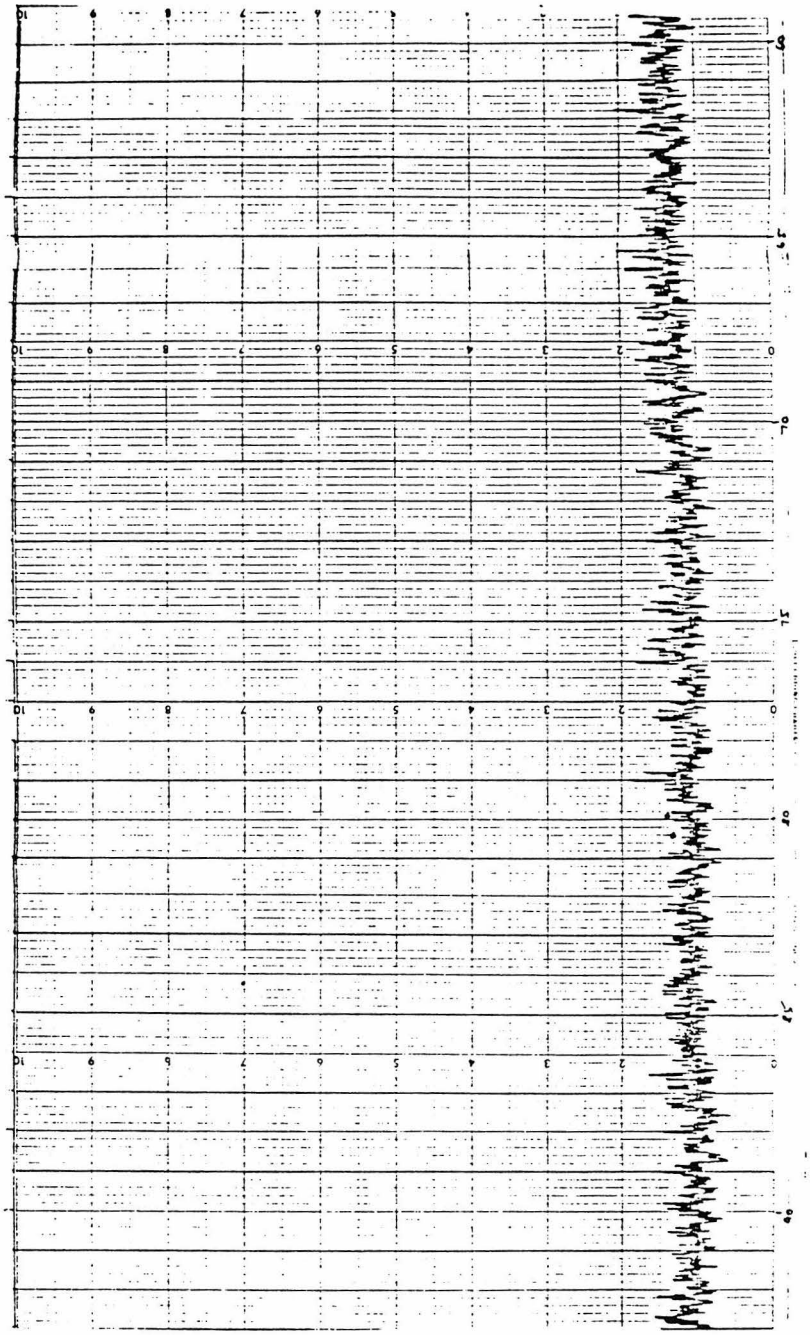

FIG. 5.2.5: CONTINUED.

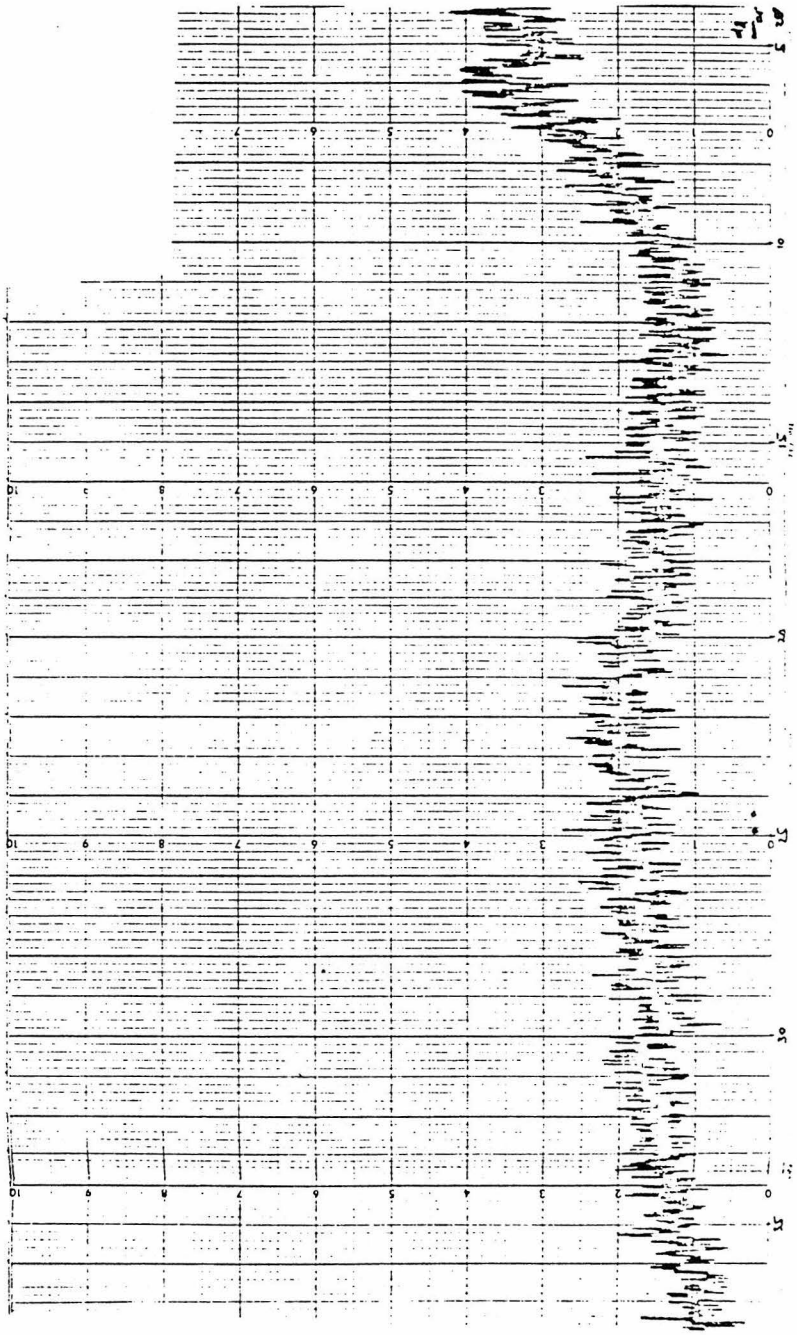

FIG. 5.2.6: NICKEL DEPOSITS FROM REACTOR ACT 31 (REDUCED). STRONG Ni LINES.

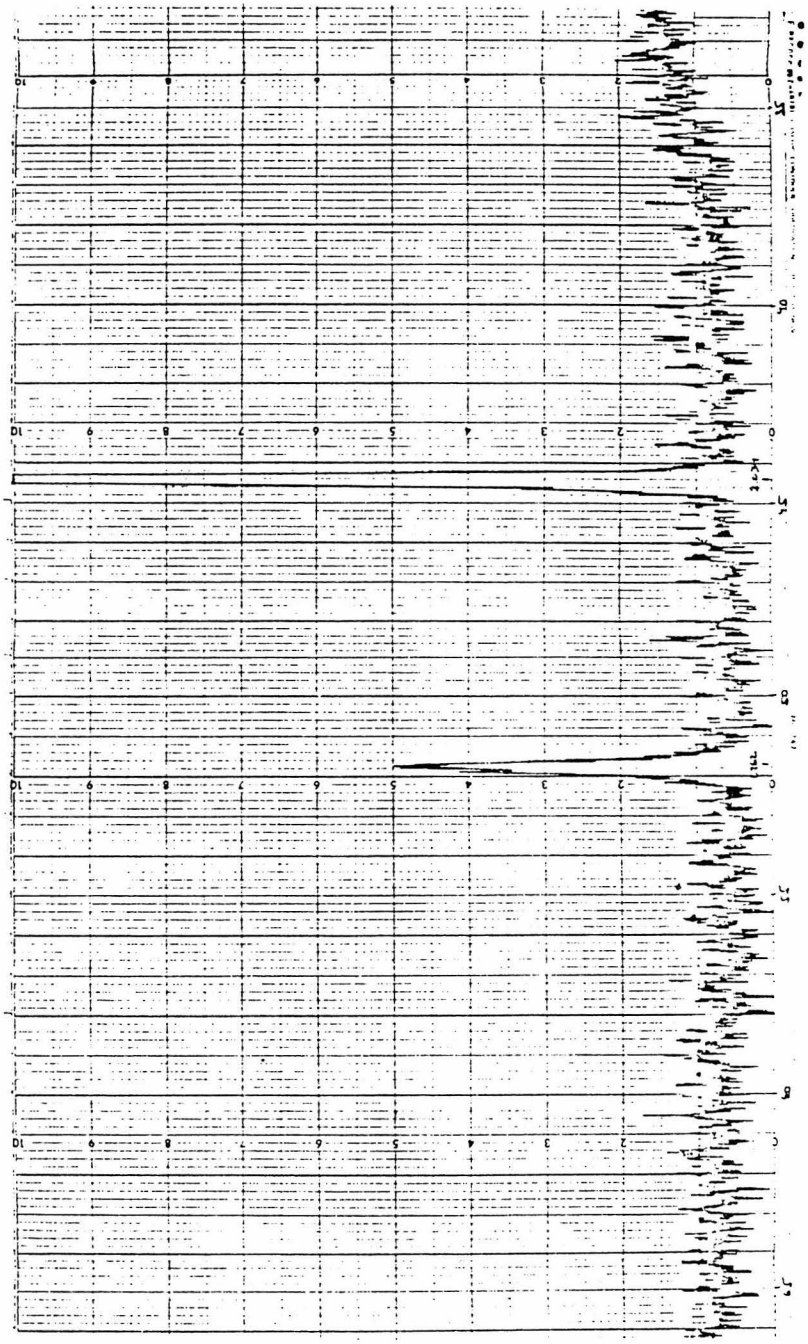

FIG. 5.2.6: CONTINUED.

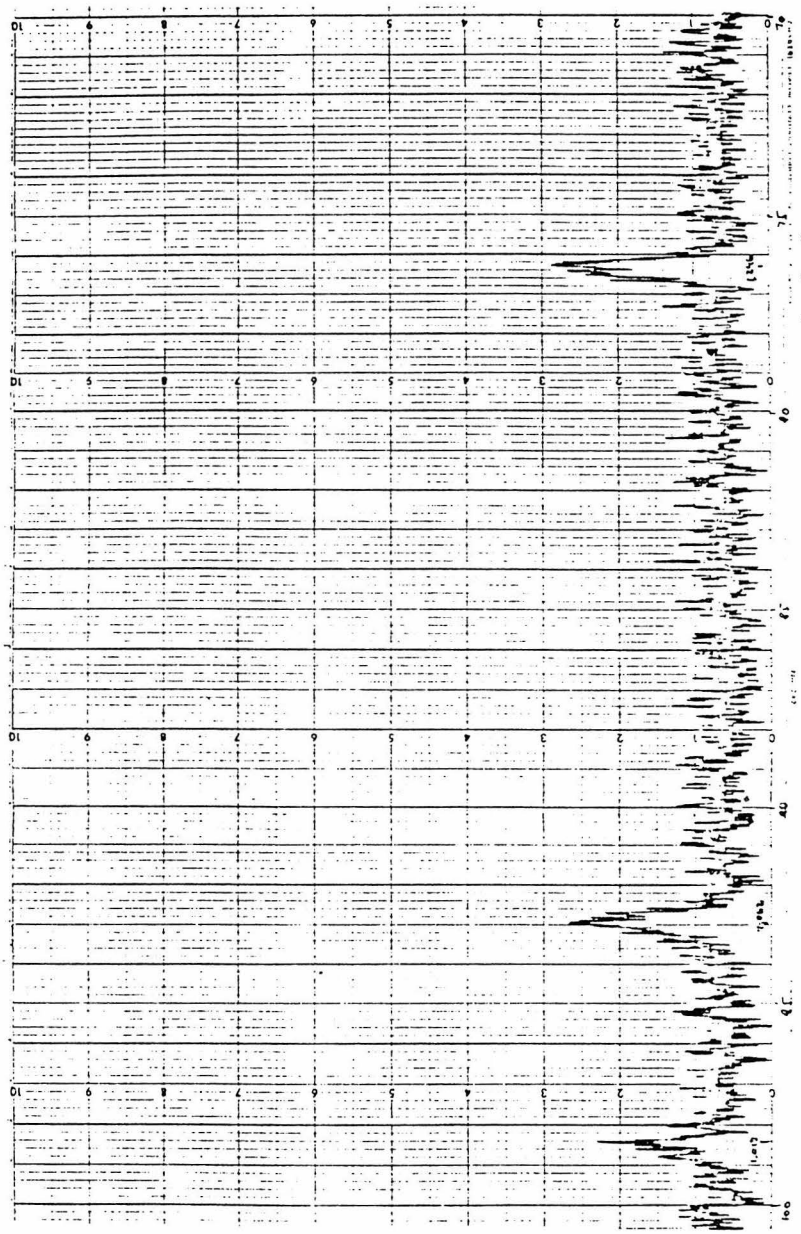

FIG. 5.2.6: CONTINUED.

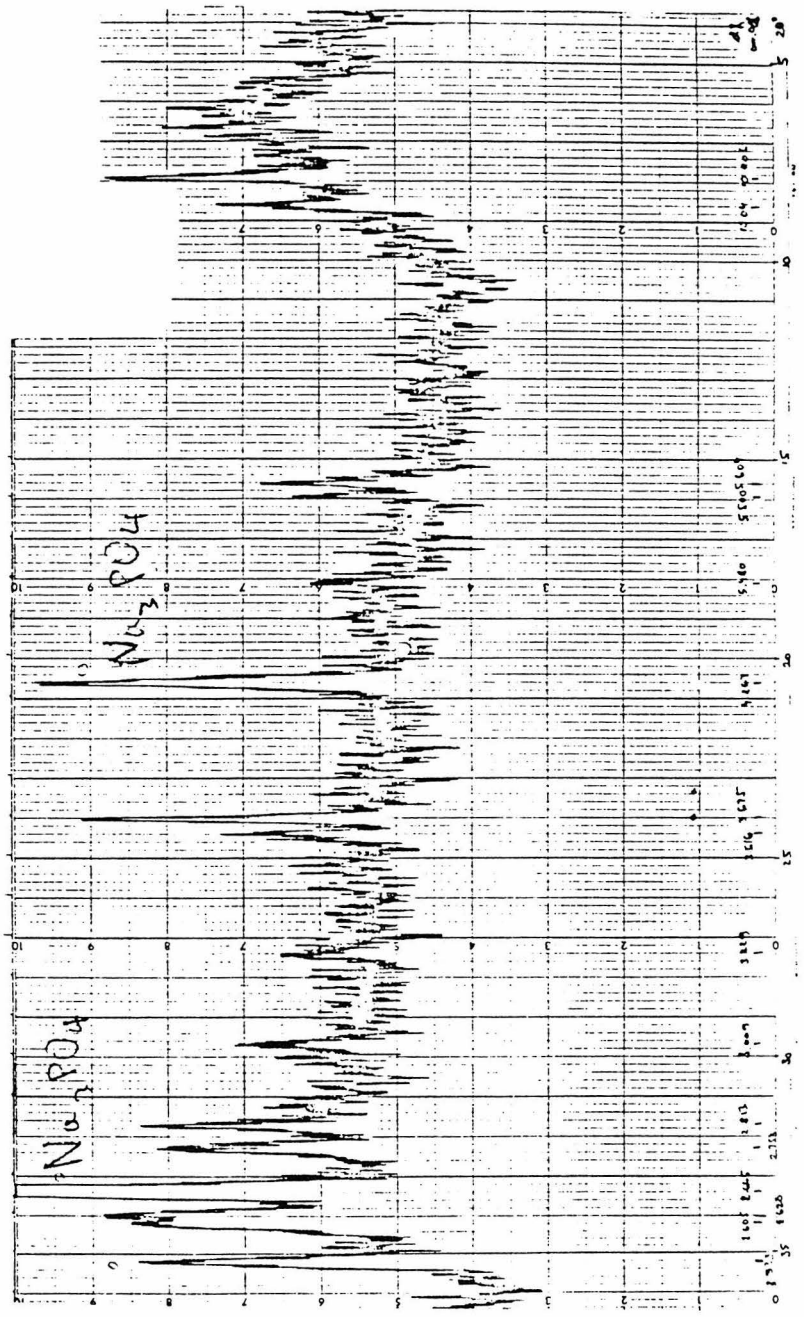

FIG. 5.2.7: MIXED MATTER FROM BOTTOM OF REACTOR ACT 30 (OXIDIZED). NiO, Na_3PO_4 AND OTHER SODIUM PHOSPHATES PRESENT.

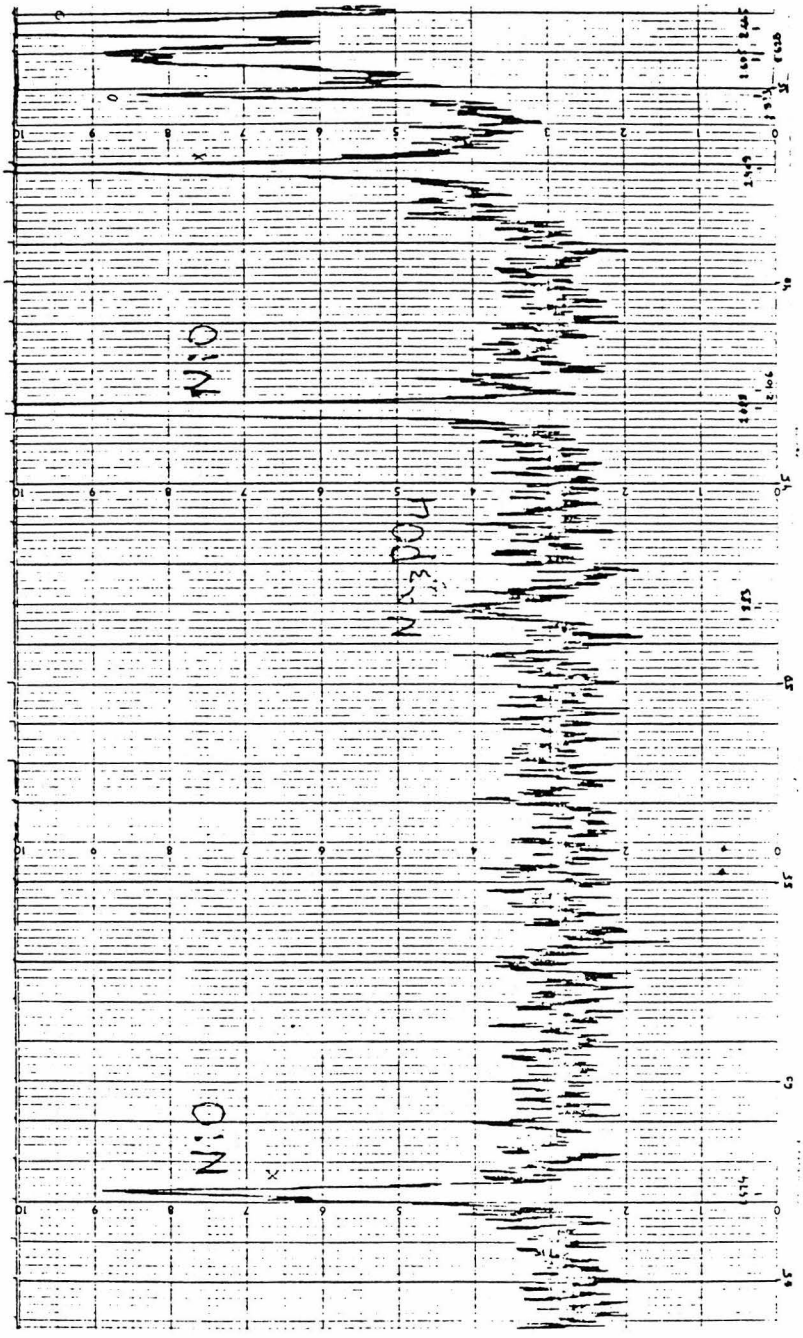

FIG. 5.2.7: CONTINUED.

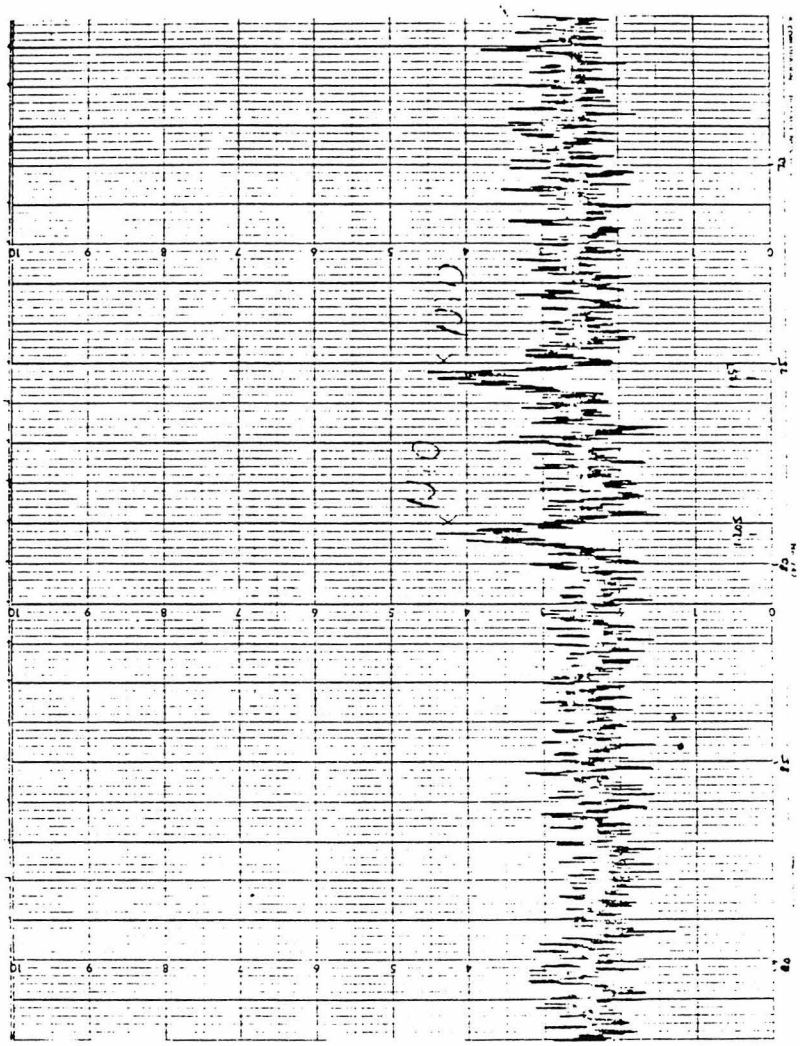

FIG. 5.2.7: CONTINUED.

tion most difficult. Under the microscope, the sample exhibited green crystalline areas and an orange glass coating. A glass of mixed oxides, $Na_2O-P_2O_5-NiO$, has deep orange color, whereas NiO is green and crystalline. The XRD pattern shows the presence of NiO (bunsenite) at λ=2.409Å, λ=2.088Å, λ=1.474Å, λ=1.257Å and λ=1.205Å. Na_3PO_4 appears at λ=4.267Å, λ=2.665Å and λ= 1.883Å. Other peaks of the sodium phosphate system also appear.

The X-ray diffraction study confirmed our hypothesis about the form of nickel in the reactor under different operating conditions. Under oxidizing conditions, NiO remains dissolved in the sodium phosphate melt except for small crystals of NiO deposited above the surface of the melt. Under reducing conditions, small Ni crystallites appear in the molten glass. These subsequently agglomerate into larger Ni deposits. Presumably, the Ni crystallites are formed at the gas-liquid interface. However, under the bubbling agitation, they disperse in the bulk of the melt.

5.2.2 Quantitative Electron Microprobe Analysis of Catalysts

Electron probe analysis can determine the local composition and structure of heterogeneous materials. This is accomplished by focusing an electron beam on a small area of the sample surface and measuring the characteristic X-rays emitted from the irradiated area. The beam is focused onto an area as small as 0.1 to 3μm in diameter and X-rays are emitted from atoms to a depth of 1-3μm below the surface. The limit of detectability is about 100-500ppm by wt. at the local level

(Birks, 1971). This technique was used on glass samples to determine their quantitative chemical composition and to detect any spatial variations in composition and any microcrystalline structures.

An electron microprobe study of polished sections of two glass samples was conducted. The instrument used was a MAC-5 SA3 model microprobe. The glasses examined were taken from reactors ACT 30 and ACT 32. Both reactors had been subjected to reduction followed by oxidation. Macroscopically, however, the materials from the two reactors had a different appearance. In the case of ACT 30, a lot of crystalline green matter (NiO) was separate from the orange Na_2O-P_2O_5-NiO glass, indicating poor redissolution of NiO into the glass upon reoxidation. In the case of ACT 32, no such NiO deposits were found and the glass had a darker color. Table 5.2.1 presents the results of the quantitative electron microprobe analysis. In the case of Sample 30-2, the content of NiO is much less than the content of NiO in the starting materials used to prepare the melt. This shows that redissolution of NiO into the melt was difficult in reactor ACT 30. The composition of NiO in the other sample, 32-1, is only slightly below the composition at preparation, indicating facile redissolution of NiO following a cycle of reduction and oxidation. The difference between the two samples is attributed to different flow patterns in the regions from where the samples were taken. Sample 30-2, showing a small NiO content, was taken from the bottom of the reactor crucible, a relatively stagnant region, whereas Sample 32-1 was taken from

TABLE 5.2.1

ELECTRON MICROPROBE STUDY OF Na_2O-P_2O_5-NiO GLASSES

Sample	Grain & Point	Na_2O	Al_2O_3	SiO_2	P_2O_5	NiO	Other Oxides	$\frac{NiO}{NiO+Na_2O+P_2O_5}$		NiO as Prepared
		(Weight per cent)								
30-2	1 • 1	16.577	20.024	14.144	38.346	1.530	9.379	2.710		
30-2	1 • 2	14.977	23.593	14.852	38.500	1.649	6.429	2.991		
30-2	1 • 3	14.690	22.302	14.839	35.284	1.869	11.016	3.605	Avg.: 3.2	17.9
30-2	1 • 4	14.777	22.094	14.752	36.744	1.942	9.691	3.632		
32-1	1 • 1	3.051	23.090	16.740	32.621	8.800	15.697	19.788		
32-1	1 • 1	10.942	23.886	19.462	29.533	7.017	9.160	14.775		
32-1	1 • 2	13.335	20.967	14.169	32.740	9.047	9.742	16.413		
32-1	1 • 3	13.953	22.872	15.022	30.561	8.368	9.225	15.824	Avg.:16.7	17.7
32-1	1 • 4	15.903	21.054	14.414	31.861	8.542	8.227	15.171		
32-1	1 • 5	15.870	20.565	14.409	31.815	8.677	8.664	15.395		
32-1	2 • 1	6.226	18.172	12.618	36.707	12.521	13.756	22.579		

Note: The averaging period for all measurements was 1 sec., with the exception of an averaging period of 10 sec. used for the first measurement of Sample 32-1, grain 1 and point 1

the annular part of the salt bath, a more agitated region. As stated in Section 2.1, the viscosity of the Na_2O-P_2O_5 melt is about 50-100 cp at reactor conditions. However, the addition of NiO greatly increases the viscosity as was qualitatively observed by melting Na_2O-P_2O_5-NiO mixtures over a Bunsen burner. Therefore, in spite of the agitation by the gas bubbles, the viscosity is sufficiently high to hinder uniformity in the melt. The different regions examined by the microprobe analysis indicate a spatial non-uniformity in the composition of the glass. This should be expected since the distribution of solid NiO is not uniform before redissolution. Because of this nonuniformity and the high viscosity of the Na_2O -P_2O_5-NiO melt, gradients of NiO concentration are set up in the glass despite the bubbling action.

In addition to Na_2O, P_2O_5 and NiO, the electron microanalysis shows Al_2O_3, SiO_2 and other oxides. These originate in the dissolution of the mullite crucible (mullite: $3Al_2O_3 \cdot 2SiO_2$) and as impurities in the starting salts.

It should be noted that alkali atoms are removed under the action of an electron beam such as that of the electron microprobe. This results in a decreasing Na signal as time passes. In the case of Sample 32-1, grain 1 and point 1, the first measurement, using an averaging period of 10 sec., gave 3.051 wt. % Na_2O; the second measurement, using an averaging period of 1 sec., gave 10.942 wt. % Na_2O. The undercount of Na_2O resulted in overestimating the content of the other oxides, including that of NiO. For example, in the case of glass 32-1,

the true NiO content is less than the measured content of 16.7%; therefore, the difference in the nickel content of the glass sample from the reactor and of the initial materials is greater than that indicated earlier.

5.2.3 Catalyst Microstructure Indentification Using Electron Microprobe Analysis

An AMR 900 electron microprobe instrument was used in a mode different from that in the last subsection to examine two-dimensional regions of glass specimens. The electron microscope mounted on the instrument was used to target and photograph interesting regions on the glass surface while the electron microprobe beam provided the qualitative chemical composition of the region. By choosing an X-ray wavelength window, characteristic of an element, e.g. Ni, and scanning the region with the microprobe, it was possible to map the composition in this particular element. This 2-D composition map could, then be photographed. This mode of electron microprobe analysis was used to determine the distribution of Ni in the glasses and to identify metallic Ni crystallites.

Two samples were analyzed using this mode of operation. Sample 32-1 is a glass taken from ACT 32, a reactor that had been reduced and reoxidized. The XRD analysis of this sample, given in Fig. 5.2.4, shows a completely amorphous substance. The chemical composition (Table 5.3.1) obtained by electron microprobe analysis is close to that at preparation. Fig. 5.2.8 is an electron microscope photograph of a region of the sample at 50X magnification and Fig. 5.2.9 shows the chemical composi-

FIG. 5.2.8: SAMPLE 32-1 (OXIDIZED)
ELECTRON MICROSCOPE VIEW, 50X, 200 μm/cm.

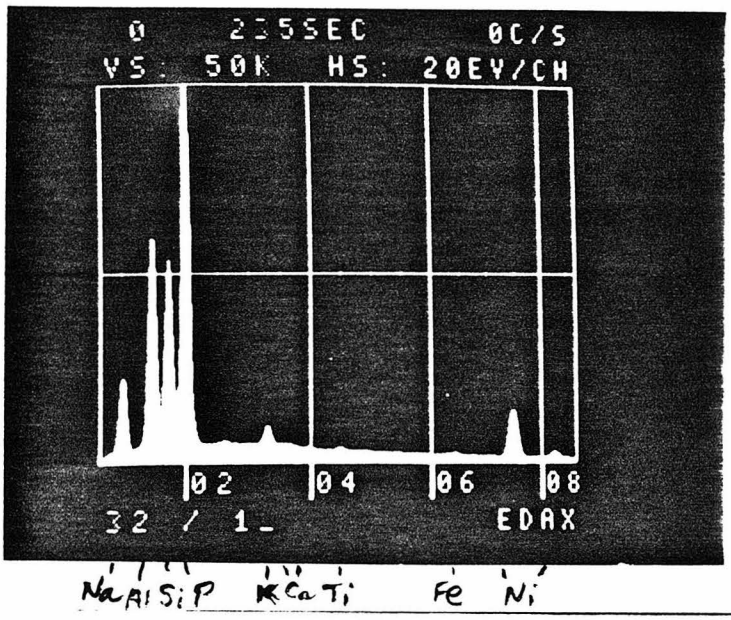

FIG. 5.2.9: SAMPLE 32-1 (OXIDIZED)

ELECTRON MICROPROBE ANALYSIS.

tion of the region. The major constituents are P(P_2O_5), Al(Al_2O_3), Na(Na_2O), Si(SiO_2), Ni(NiO), K(K_2O) and small amounts of Ca,Ti and Fe. These results are consistent with the quantitative data of Table 5.3.1. Fig. 5.2.10 is an X-ray map in the Ni window of the same region shown in Fig. 5.2.8. No significant patterns of Ni distribution can be detected. Raising the magnification to 10,000X (Figs. 5.2.11, 5.2.12) does not lead to the recognition of any significant pattern. Rather, Ni (in an oxidized form) is uniformly distributed in the glass. Overall, it seems that NiO is evenly dissolved and distributed in the glass under oxidizing conditions.

Sample 31-2 is a glass taken from ACT 31, a reactor which was last treated by reduction with H_2. The XRD analysis of this sample is given in Fig. 5.2.5. The amorphous pattern of the glass is accompanied by small Ni peaks. This two-dimensional electron microprobe study found the small Ni crystallites responsible for these peaks. Fig. 5.2.13 is an electron microscope photograph of a Ni crystallite at 10,000X magnification. Its size is about 2μm. Fig. 5.2.14 is a Ni X-ray map of the environment of this crystallite. It can be seen that the sphere of the photograph corresponds to a large density of Ni, whereas the rest of the area is poor in Ni. While both reactors ACT 31 and ACT 32 were prepared with essentially the same amount of NiO, Figs. 5.2.12 and 5.2.14 indicate that the glass in ACT 31-2 contains much less Ni. Reducing conditions remove nickel from its dissolved state to form metal particles that are partly transferred to the surface (metallic Ni). Moreover, the pattern

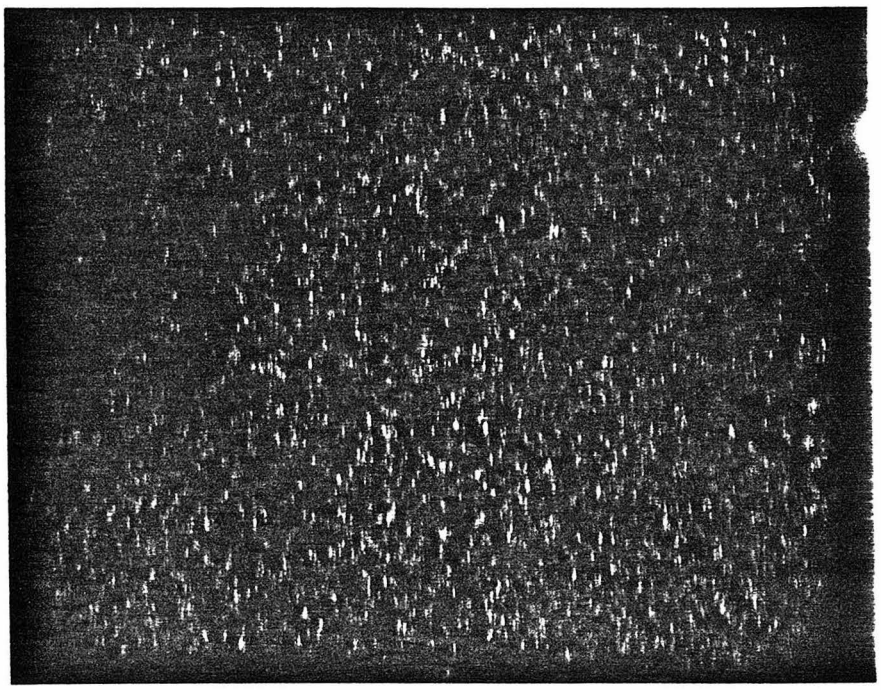

FIG. 5.2.10: SAMPLE 32-1 (OXIDIZED).
Ni X-RAY MAP, MAGNIFICATION 50X.

FIG. 5.2.11: SAMPLE 32-1 (OXIDIZED)

ELECTRON MICROSCOPE VIEW, 10,000X, 1 μm/cm.

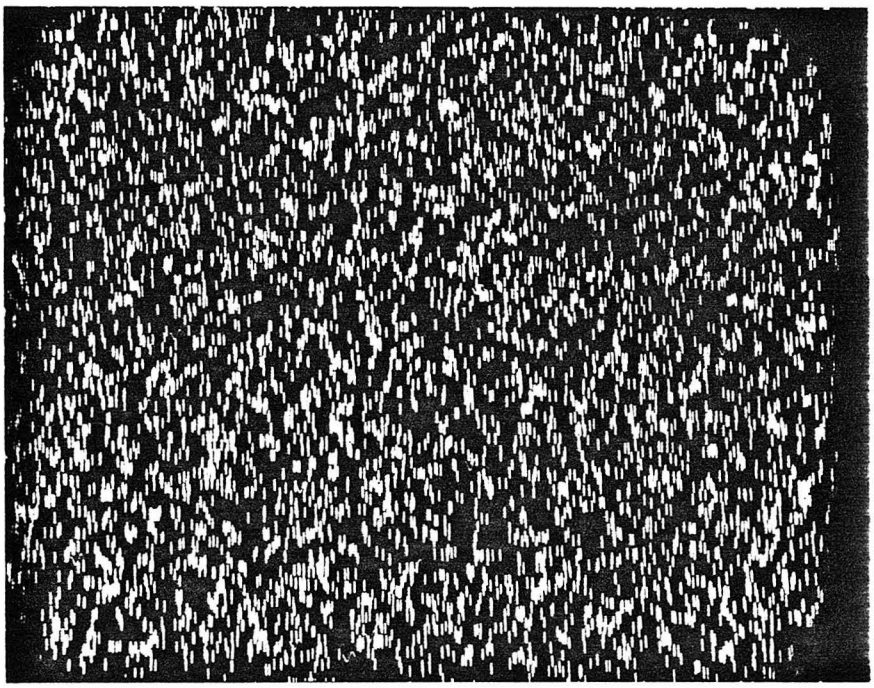

FIG. 5.2.12: SAMPLE 32-1 (OXIDIZED)

Ni X-RAY MAP, MAGNIFICATION 10,000X

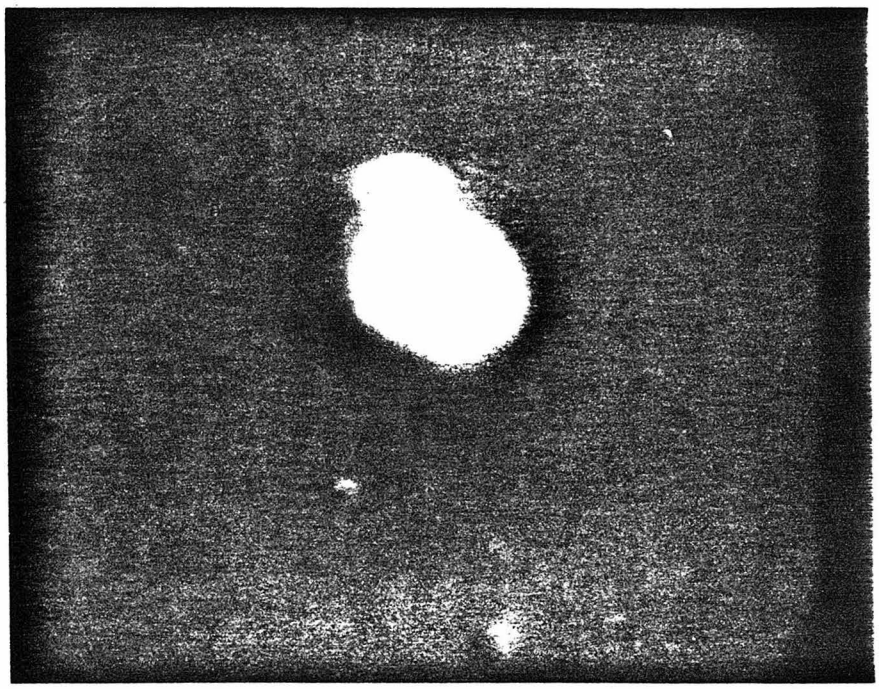

FIG. 5.2.13: SAMPLE 31-2 (REDUCED)
ELECTRON MICROSCOPE VIEW, 10,000X, 1 μm/cm.

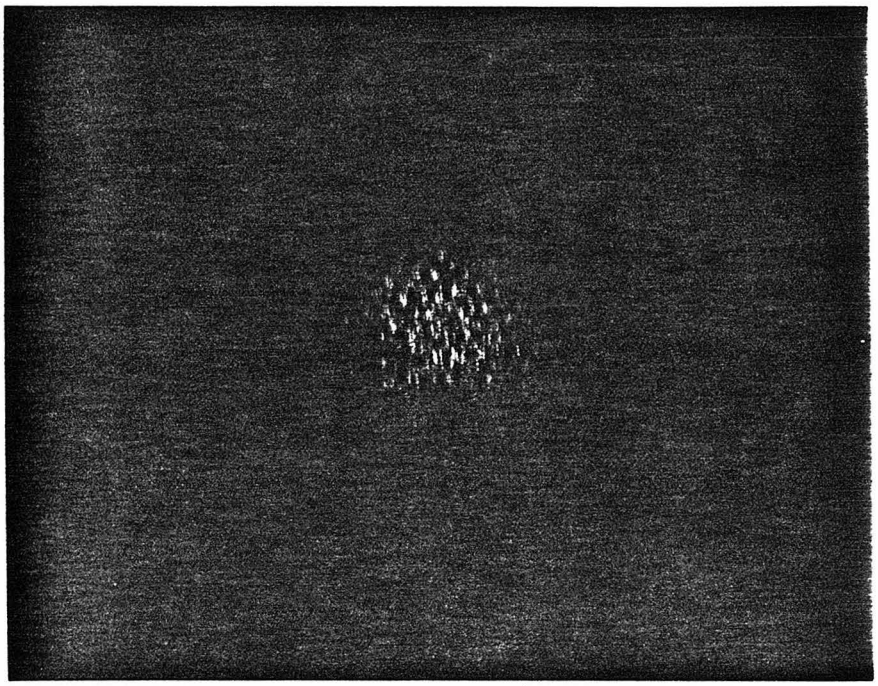

FIG. 5.2.14: SAMPLE 31-2 (REDUCED)

Ni X-RAY MAP, MAGNIFICATION 10,000X

of Ni distribution in Fig. 5.2.14 is weaker at the edges of the sphere and stronger at the center. This suggests that the sphere is wetted and partially embedded in the glass.

Fig. 5.2.15 is an electron microscope photograph of another Ni crystallite in Sample 31-2 and Fig. 5.2.16 is the corresponding X-ray map. Again, the same depletion in Ni is noticed away from the sphere. The apparent size of the sphere is about 2μm, whereas the size of the X-ray pattern corresponding to the sphere is about 2.5μm, indicating wetting between the metal and the salt and a possible gradient of nickel concentration in the salt close to the sphere.

Figs. 5.2.17 and 5.2.18 are chemical composition analyses for points A and B of Fig. 5.2.15. Point A,on the sphere, shows a high Ni intensity as well as the melt components Na, P, Si, Al. Point B, in the glass, away from the sphere, shows strong melt component intensities, while it is almost entirely depleted in Ni. These chemical composition checks confirm that the sphere is a Ni crystallite and the bulk of the glass contains very little nickel.

5.2.4 Phases Present in the Reactors

The different catalyst analyses, combined with the method of catalyst preparation and the experimental procedure, lead to the following picture of the reactor under experimental conditions. The phases present at high temperatures (800 to 1000°C) under oxidizing conditions, in a reactor originally containing Na_2O - - P_2O_5 and NiO are (Fig. 5.2.19) mullite (solid), sodium phos-

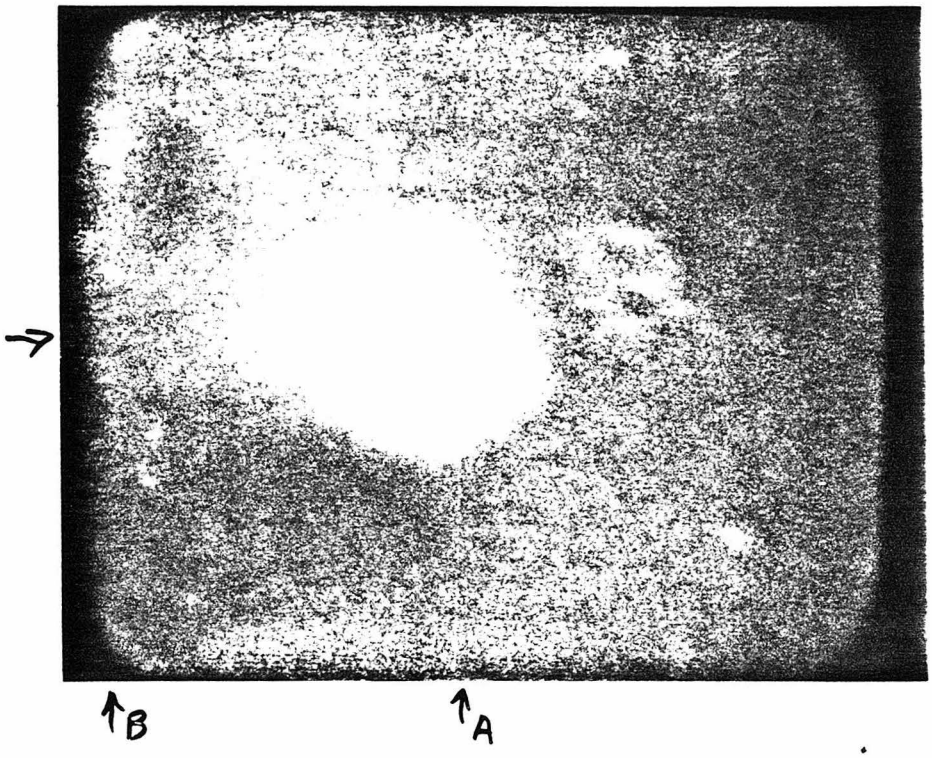

FIG. 5.2.15: SAMPLE 31-2 (REDUCED)

ELECTRON MICROSCOPE VIEW, 10,000X 1 μm/cm.

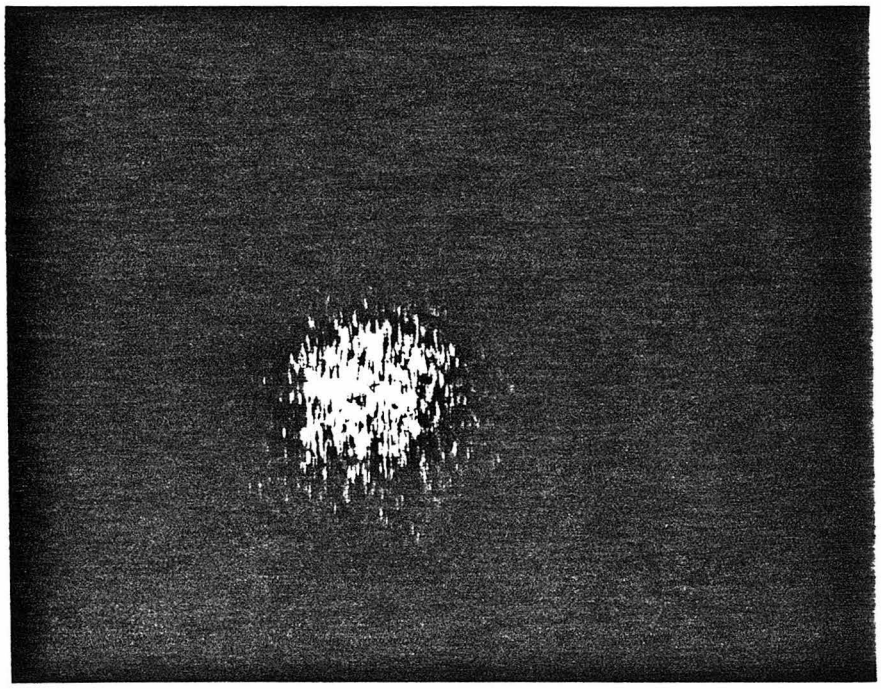

FIG. 5.2.16: SAMPLE 31-2 (REDUCED)
Ni X-RAY MAP, MAGNIFICATION 10,000X.

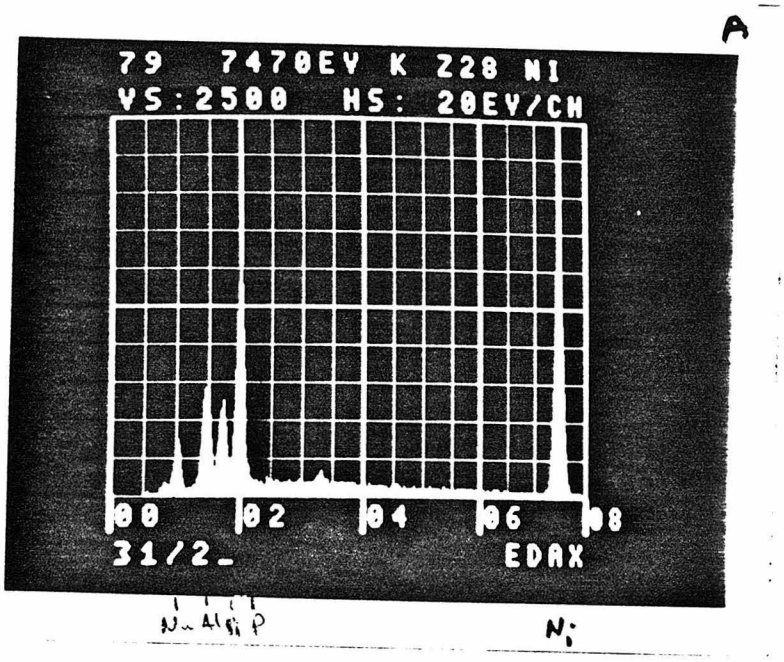

FIG. 5.2.17: ELECTRON MICROPROBE ANALYSIS OF REGION A, FIG. 5.2.15.

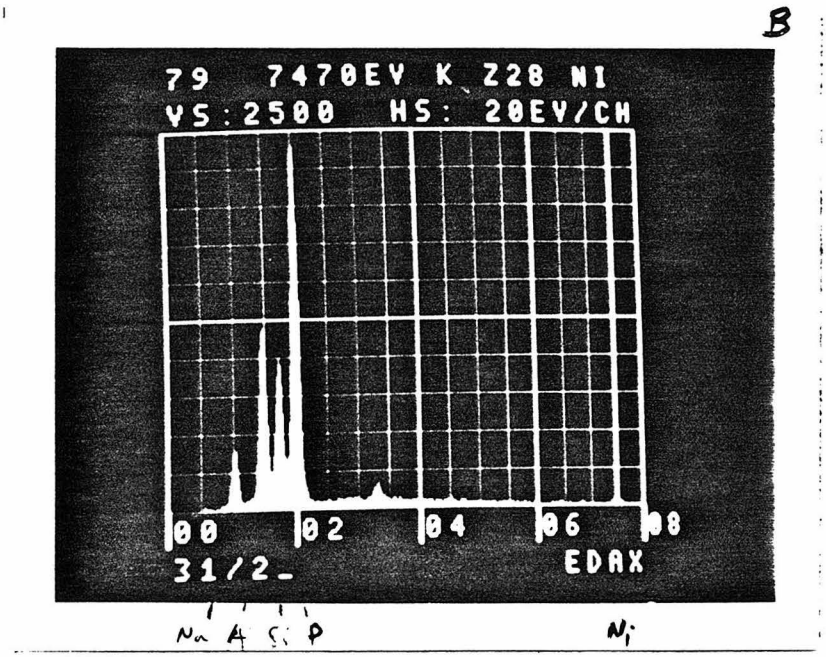

FIG. 5.2.18: ELECTRON MICROPROBE ANALYSIS OF REGION B, FIG. 5.2.15.

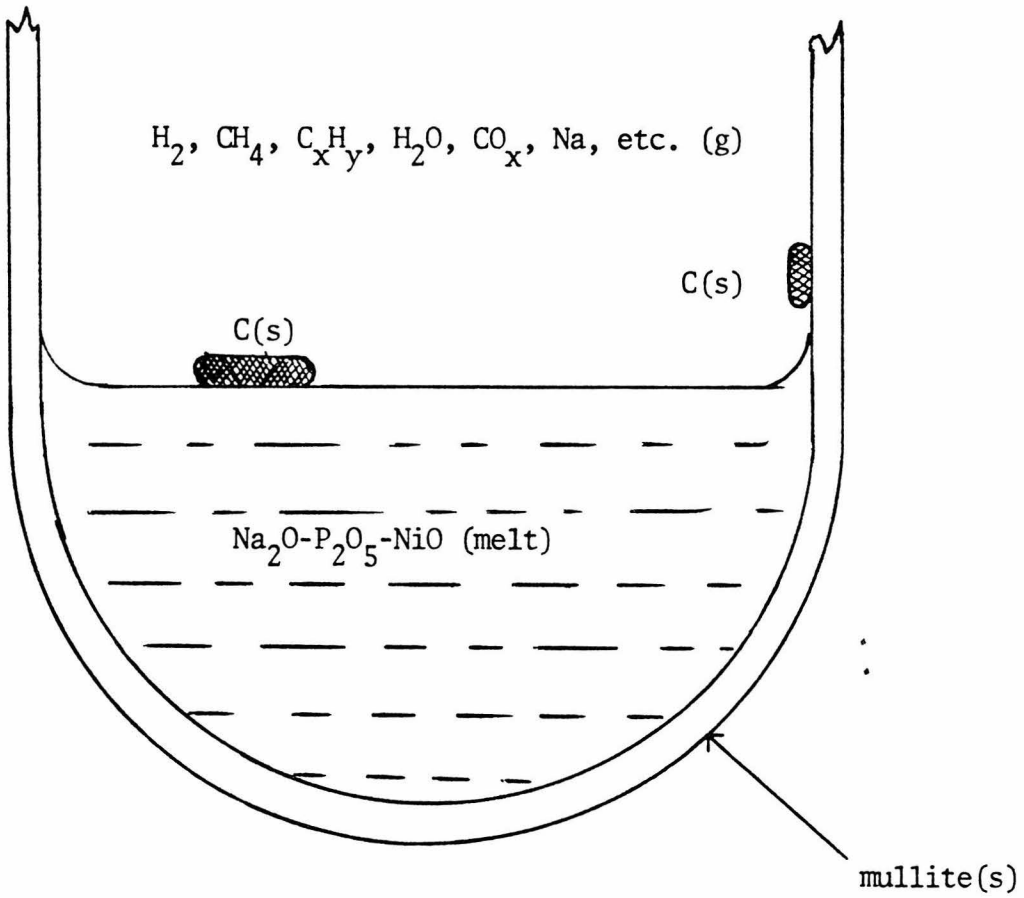

FIG. 5.2.19: PHASES PRESENT IN A REACTOR, ORIGINALLY CONTAINING Na_2O-P_2O_5-NiO, UNDER OXIDIZING CONDITIONS.

phates (melt) and NiO (in solution), and carbon or carbonaceous matter (solid).. Additionally, there is the gaseous phase containing H_2, CH_4, other hydrocarbons, H_2O, CO, CO_2, Na, etc. The same reactor under reducing conditions contains (Fig. 5.2.20) mullite (solid), sodium phosphates (melt), Ni (solid) and carbon (solid). In this case Ni and C can form a solid solution (alloy). The same gaseous mixture also exists.

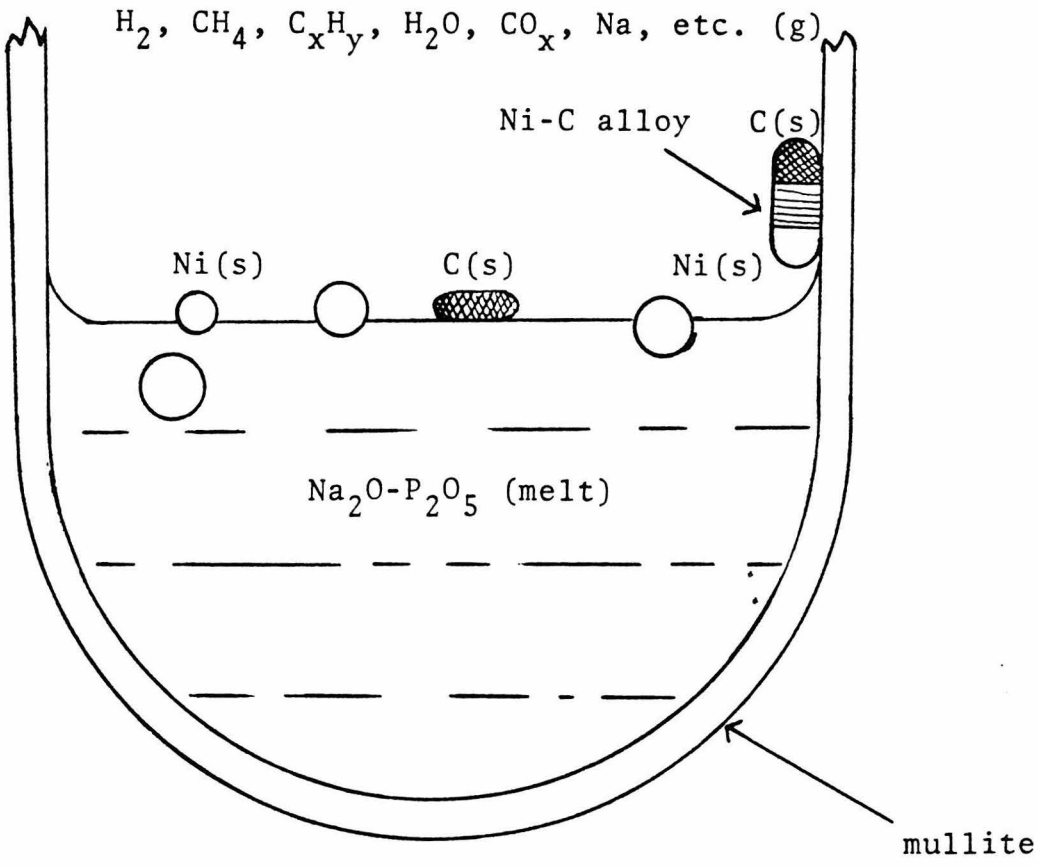

FIG. 5.2.20: PHASES PRESENT IN A REACTOR, ORIGINALLY CONTAINING Na_2O-P_2O_5-NiO, UNDER REDUCING CONDITIONS.

SECTION 5.3: DEPENDENCE OF RATE ON W^{o}_{NiO}

5.3.1 Results

Since the catalyzed steam-methane reaction takes place on the surface of metallic Ni, the reaction rate would depend on the amount of NiO originally added to the reactor. Reactors with different nickel contents were prepared and methane-steam reforming experiments were performed to examine the relation between the rate and nickel content.

Tables 5.3.1 and 5.3.2 list the reaction rate as a function of nickel content for two sets of conditions. There is a general increase in the rate of CO_x formation, r_{CO_x}, with the amount of NiO originally added to the reactor, W^{o}_{NiO}.

5.3.2 Analysis and Discussion

The relation between mass and surface area depends on the particle size distribution. In the case of Ni particles formed from the melt upon reduction of NiO, this distribution is affected by particle agglomeration, or sintering. The temperature and the time elapsed under reducing conditions determine the extent of sintering. Assuming, however, that these changes in particle size distribution do not vary greatly among experiments, the surface area is simply proportional to the amount of Ni, or of NiO originally added to the reactor, W^{o}_{NiO}. Therefore, the rate attributable to Ni, $\left(r_{CO_x}\right)_{Ni}$, is proportional to W^{o}_{NiO}:

$$\frac{\left(r_{CO_x}\right)_{Ni}}{p_{CH_4}} = R_{Ni} \quad W^{o}_{NiO} \qquad (5.3.1)$$

TABLE 5.3.1

STEAM REFORMING OF METHANE IN ACT REACTORS

Salt: $Na_2O-P_2O_5-NiO$ P = 1 atm. T = 1168°K

Effect of w_{NiO} on the rate

Run	NiO Wt(g)	Total Salt(g)	$\dot{n}_T$(mol/s)	y_{H_2O} (atm)	r_{CO_x} (mol/s)	r_{CO_x}/p_{CH_4} (mol/s)	$\left(r_{CO_x}\right)_{Ni}/p_{CH_4}$ (mol C/s/atm)
24.T2	.28	15.6	14.4×10^{-5}	.03	2.8×10^{-8}	3.1×10^{-8}	0×10^{-8}
38.T2(7)	.49	13.3	3.8 "	.03	58.3 "	60.8 "	44.0 "
38.T2(10)	.49	13.3	9.5 "	.03	75.6 "	78.1 "	66.0 "
38.T2(12)	.49	13.3	15.3 "	.03	79.4 "	81.8 "	70.0 "
18.T1(1)	.78	15.1	3.8 "	.03	63.0 "	65.0 "	53.0 "
18.T1(3)	.78	15.1	3.8 "	.03	106.0 "	109.0 "	97.0 "
19.T1(1)	.78	15.1	3.8 "	.03	141.0 "	145.0 "	133.0 "
19.T1(2)	.78	15.1	14.4 "	.03	98.0 "	101.0 "	89.0 "

Note: At T = 1168°K, $\left(\frac{r_{CO_x}}{p_{CH_4}}\right)_{BASE} = 11.6 \times 10^{-8} \frac{\text{mol C}}{\text{s}\cdot\text{atm}}$

TABLE 5.3.2

STEAM REFORMING OF METHANE IN ACT REACTORS

Salt: $Na_2O-P_2O_5-NiO$ P = 1 atm. T = 1193°K

Effect of w_{NiO} on the Rate

Run	NiO Wt(g)	Total Salt(g)	$\dot{n}_T$(mol/s)	y_{H_2O} (atm)	r_{CO_x} (mo/ C/s)	r_{CO_x}/p_{CH_4} (mol C/s)	$\left[r_{CO_x}\right]_{Ni}/p_{CH_4}$ (mol C s/atm)
24.T3	.28	15.6	14.4×10^{-5}	.09	5.6×10^{-8}	5.8×10^{-8}	0×10^{-8}
39.T1(1)	.38	12.8	4.2 "	.08	171.0 "	206.0 "	186.0"
39.T1(2)	.38	12.8	4.2 "	.07	180.0 "	215.0 "	195.0"
37.T1(7)	.40	13.2	4.1 "	.10	72.8 "	82.0 "	62.0"
18.T2(7)	.78	15.1	15.6 "	.10	242.0 "	269.0 "	249.0"
19.T2(1)	.78	15.1	15.6 "	.10	106.0 "	118.0 "	98.0"
19.T2(4)	.78	15.1	15.6 "	.10	175.0 "	194.0 "	174.0"

Note: At T = 1193°K, $\frac{\left[r_{CO_x}\right]_{BASE}}{p_{CH_4}} = 20.3 \times 10^{-8} \frac{\text{mol C}}{\text{s}\cdot\text{atm}}$

where: $\left(r_{CO_x}\right)_{Ni}$ = rate of CH_4-H_2O reaction on Ni, mol C/s

p_{CH_4} : methane partial pressure, atm.

R_{Ni} : rate of CH_4-H_2O reaction on Ni, per unit mass of added NiO, normalized for p_{CH_4}, $\frac{\text{mol C}}{\text{s atm gNiO}}$

W^o_{NiO} : amount of NiO originally added to the reactor, g.

Equation (5.3.1) assumes a first order dependence of the reaction on methane, as proposed by Bodrov (1964) and Ross (1973). The observed rate of CO_x formation, r_{CO_x}, is a sum of the rate taking place on Ni, $\left(r_{CO_x}\right)_{Ni}$, and the rate observed under the same conditions in the absence of Ni, $\left(r_{CO_x}\right)_{BASE}$:

$$\frac{r_{CO_x}}{p_{CH_4}} = \frac{\left(r_{CO_x}\right)_{BASE}}{p_{CH_4}} + \frac{\left(r_{CO_x}\right)_{Ni}}{p_{CH_4}} \qquad (5.3.2)$$

where: r_{CO_x} : observed rate of the CH_4-H_2O reaction, $\frac{\text{mol C}}{\text{s}}$,

$\left(r_{CO_x}\right)_{BASE}$: rate observed under the same conditions in the absence of Ni, $\frac{\text{g mol}}{\text{s}}$

Values of $\left(r_{CO_x}\right)_{BASE}$ were obtained from the average values of r_{CO_x} in Fig. 4.6.1, presenting results in blank reactors and non-active molten salt systems. Equations (5.3.1) and (5.3.2) were applied to the data presented in Tables 5.3.1 and 5.3.2 to obtain values of $\left(r_{CO_x}\right)_{Ni}/p_{CH_4}$ vs. W^o_{NiO}. These two variables are plotted in Fig. 5.3.1. It is apparent that

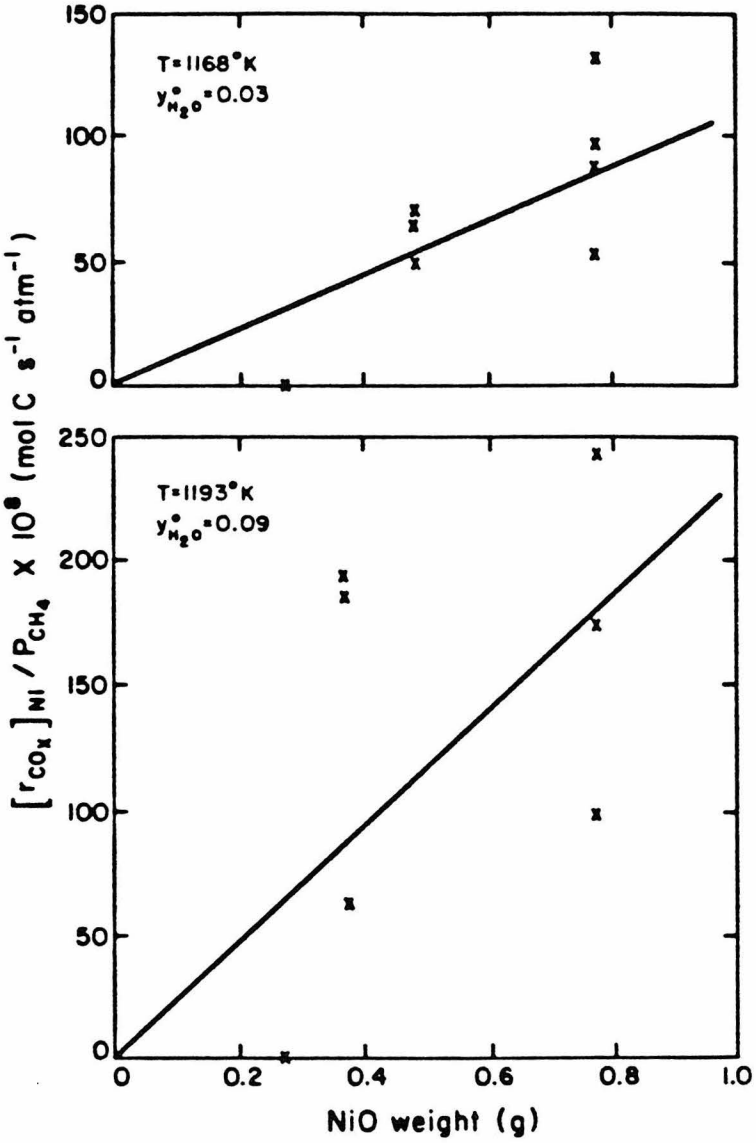

FIG. 5.3.1: CH_4 - H_2O REFORMING

SALT: Na_2O - P_2O_5 - NiO

$\left[r_{CO_x}\right]_{Ni}/p_{CH_4}$ increases with W^{o}_{NiO}. A linear relationship such as equation (5.3.1) is seen to be satisfactory. The large variance in the results can be attributed to differences in particle size distribution and extents of sintering among the different runs.

SECTION 5.4: DEPENDENCE OF RATE ON p_{H_2O}/p_{H_2}.

The rate of the CH_4-H_2O reaction on Ni is adversely affected by the presence of excess H_2O in the gas phase. Ross and Steel (1973) proposed the rate expression

$$\left[r_{CO_x}\right]Ni \propto p_{CH_4}^{1.0} \cdot p_{H_2O}^{-0.5} \qquad (5.4.1)$$

in the 773° to 953°K range, whereas Bodrov et al. (1964) suggested

$$\left[r_{CO_x}\right]Ni \propto \frac{k\, p_{CH_4}}{1+a\,\frac{p_{H_2O}}{p_{H_2}}} \qquad (5.4.2)$$

at 1173°K. Both expressions indicate a negative reaction order with respect to H_2O. The reaction:

$$NiO(s) + H_2(g) \rightarrow Ni(s) + H_2O(g) \qquad (5.4.3)$$

is fast and has an equilibrium constant of 141 at 1173°K (Mah, 1976), thus, for low p_{H_2O}/p_{H_2}, Ni must exist in metallic form. If, however, $p_{H_2O}/p_{H_2} > 141$, at 1173°K, Ni would be present as NiO and the rate would be near its base value, $\left[r_{CO_x}\right]BASE$, observed on surfaces with no specific catalytic activity.

In the experiments reported, the reactor feed contained only CH_4 and H_2O, i.e. $p^o_{H_2} = 0$. However, in the reactor, H_2 is produced by the pyrolysis of methane and the steam methane reaction itself. Thus, the ratio p_{H_2O}/p_{H_2} decreases along the reactor from $+\infty$ to some finite value. If this ratio decreased below the critical p_{H_2O}/p_{H_2} value as established by the equilibrium constant of (5.4.3), nickel would exist as Ni and not NiO from that point on in the reactor. However, the

ACT reactor is not an ideal plug flow reactor as far as the gas is concerned and the melt is agitated by the bubbles. Hence, mixing of nickel particles and of gas occurs and the change from NiO to Ni is not as abrupt and complete.

Tables 5.4.1 through 5.4.5 list experimental results at a series of five different temperatures. The p_{H_2O}/p_{H_2} ratio listed is that at the reactor outlet. Assuming a proportional relation between catalyst activity and catalyst weight, W^o_{NiO} (See Section 5.3), a normalized reaction rate $\left[r_{CO_x}\right]/(p_{CH_4} \cdot W^o_{NiO})$, was obtained. The normalization with respect to W^o_{NiO} is not entirely appropriate, since some of the nickel exists in the non-active NiO form. It would be preferable to normalize with respect to the weight of reduced metallic nickel. The present approach is clearly a first approximation. A more detailed analysis is presented in Chapter 6 under the topic of reactor modeling. Fig. 5.4.1 depicts the data of Table 5.4.3. The abrupt increase in reactivity below a critical p_{H_2O}/p_{H_2} ratio is evident. Above this critical value $\left[r_{CO_x}\right]_{Ni} \simeq 0$ as expected by the definition of $\left[r_{CO_x}\right]_{Ni}$.

TABLE 5.4.1

STEAM REFORMING OF METHANE IN ACT REACTORS

Salt: $Na_2O-P_2O_5-NiO$ P = 1 atm T = 1143°K

Effect of p_{H_2O}/p_{H_2} on Rate

Run	NiO Wt(g)	Total Salt(g)	$\dot{n}_T$(mol/s)	p_{H_2O}/p_{H_2}	r_{CO_x} (mol C/s)	r_{CO_x}/p_{CH_4} (mol C/s/atm)	$\left(r_{CO_x}\right)_{Ni}/(p_{CH_4} w_{NiO})$ (mol C/(s·atm·gNiO))
38.T1(4)	.49	13.3	11.9×10^{-5}	862.	2.38×10^{-8}	7.7×10^{-8}	3×10^{-8}
38.T1(5)	.49	13.3	6.8 "	328.	2.72 "	5.0 "	0 "
38.T1(7)	.49	13.3	4.6 "	20.	12.4 "	15.3 "	19 "
38.T1(8)	.49	13.3	4.0 "	1.02	76.0 "	84.0 "	159 "
36.T3(1)	.38	13.3	14.4 "	8.6	14.0 "	14.4 "	22 "
36.T3(2)	.38	13.3	15.9 "	78.0	7.0 "	7.9 "	4 "
36.T3(3)	.38	13.3	16.6 "	109.0	7.0 "	8.3 "	6 "
34.T1(1)	1.00	25.7	36.8 "	2300.0	2.94 "	7.7 "	1 "
34.T1(2)	1.00	25.7	17.5 "	48.0	21.0 "	26.3 "	20 "
34.T1(3)	1.00	25.7	15.4 "	18.8	21.1 "	23.2 "	17 "

Note: (a) At 1143°K, $\left(\frac{r_{CO_x}}{p_{CH_4}}\right)_{BASE} = 6.2\times10^{-8} \frac{\text{mol C}}{\text{s·atm}}$

(b) Equilibrium of (5.4.3), $K_{eq} = 149$

TABLE 5.4.2

STEAM REFORMING OF METHANE IN ACT REACTORS

Salt: $Na_2O-P_2O_5-NiO$ P = 1 atm T = 1168°K

Effect of p_{H_2O}/p_{H_2} on Rate

Run	NiO Wt(g)	Total Salt(g)	$\dot{n}_T$(mol/s)	p_{H_2O}/p_{H_2}	r_{CO_x} (mol C/s)	r_{CO_x}/p_{CH_4} (mol C/s/atm)	$\left(r_{CO_x}\right)_{Ni}/(p_{CH_4} w_{NiO})$ (mol C/(s·atm·gNiO))
38.T2(1)	.49	13.3	8.2×10^{-5}	97.0	10.7×10^{-8}	19.8×10^{-8}	$17.\times10^{-8}$
38.T2(4)	.49	13.3	7.6 "	121.0	9.1 "	18.6 "	14. "
38T.2(5)	.49	13.3	4.5 "	1.04	181.0 "	229.0 "	444. "
38.T2(7)	.49	13.3	3.8 "	.28	58.3 "	60.8 "	100. "
38.T2(10)	.49	13.3	9.5 "	.89	75.6 "	78.1 "	136. "
38.T2(12)	.49	13.3	15.3 "	1.01	79.4 "	81.8 "	143. "
34.T2(1)	1.00	25.7	14.4 "	8.6	14.0 "	14.9 "	3. "
34.T2(2)	1.00	25.7	16.9 "	17.2	47.6 "	57.0 "	45. "
34.T2(3)	1.00	25.7	39.9 "	2600.0	2.79 "	7.4 "	0 "

Note: (a) At T = 1168°K, $\left(\frac{r_{CO_x}}{p_{CH_4}}\right)_{BASE} = 11.6\times10^{-8}\frac{\text{mol C}}{\text{s·atm}}$

(b) Equilibrium of (5.4.3), $K_{eq} = 143$

TABLE 5.4.3

STEAM REFORMING OF METHANE IN ACT REACTORS

Salt: $Na_2O-P_2O_5-NiO$ P = 1 atm T = 1193°K

Effect of p_{H_2O}/p_{H_2} on Rate

Run	NiO Wt(g)	Total Salt(g)	$\dot{n}_T$(mol/s)	p_{H_2O}/p_{H_2}	r_{CO_x} (mol C/s)	r_{CO_x}/p_{CH_2} (mol C/s/atm)	$\left[r_{CO_x}\right]_{Ni}/(p_{CH_4} w_{NiO})$ (mol C/(s·atm·gNio))
36.T2(2)	.38	13.3	17.1×10^{-5}	16.7	51.8×10^{-8}	63.2×10^{-8}	113×10^{-8}
36.T2(3)	.38	13.3	22.6 "	250.0	9.7 "	14.9 "	0 "
34.T3(1)	1.00	25.7	36.8 "	119.0	54.5 "	144.0 "	124 "
34.T3(3)	1.00	25.7	17.5 "	3.92	238.0 "	298.0 "	278 "
37.T1(1)	.40	13.2	6.3 "	30.4	20.8 "	36.0 "	39 "
37.T1(2)	.40	13.2	16.1 "	1100.0	3.22 "	14.9 "	0 "
37.T1(3)	.40	13.2	8.8 "	148.0	9.7 "	23.6 "	8 "
37.T1(4)	.40	13.2	4.7 "	1.01	242.0 "	332.0 "	779 "
37.T1(6)	.40	13.2	5.0 "	1.64	177.0 "	252.0 "	579 "
37.T1(7)	.40	13.2	4.1 "	.96	72.8 "	82.0 "	154 "
39.T1(1)	.38	12.8	4.2 "	.68	171.0 "	206.0 "	489 "
39.T1(2)	.38	12.8	4.2 "	.54	180.0 "	215.0 "	512 "

Note: (a) At T=1193°K, $\left(\frac{r_{CO_x}}{p_{CH_4}}\right)_{BASE} = 20.3\times10^{-8}\ \frac{\text{mol C}}{\text{s·atm}}$ (b) Equilibrium of (5.4.3), K_{eq}=138

TABLE 5.4.4

STEAM REFORMING OF METHANE IN ACT REACTORS

Salt: $Na_2O-P_2O_5-NiO$ P = 1 atm T = 1218°K

Effect of p_{H_2O}/p_{H_2} on the Rate

Run	NiO Wt(g)	Total Salt(g)	$\dot{n}_T$(mol/s)	p_{H_2O}/p_{H_2}	r_{CO_x} (mol C/s)	r_{CO_x}/p_{CH_4} (mol C/s/atm)	$\left[r_{CO_x}\right]_{Ni}/(p_{CH_4} w_{NiO})$ (mol C/(s·atm·gNiO))
34.T4(1)	1.00	25.7	15.9×10^{-5}	20.5	26.5×10^{-8}	29.8×10^{-8}	0×10^{-8}
34.T4(2)	1.00	25.7	23.3 "	15.9	168.0 "	280.0 "	245 "
34.T4(3)	1.00	25.7	36.8 "	34.8	187.0 "	494.0 "	459 "
34.T4(4)	1.00	25.7	29.1 "	32.2	134.0 "	280.0 "	245 "
34.T4(5)	1.00	25.7	58.3 "	89.0	44.9 "	187.0 "	151 "

Note: (a) At T = 1218°K, $\left(\frac{r_{CO_x}^{\bullet}}{p_{CH_4}}\right)_{BASE} = 35.5\times10^{-8}\ \frac{\text{mol C}}{\text{s·atm}}$

(b) Equilibrium of (5.4.3), $K_{eq} = 135$

TABLE 5.4.5

STEAM REFORMING OF METHANE IN ACT REACTORS

Salt: $Na_2O-P_2O_5-NiO$ P = 1 atm T = 1243°K

Effect of p_{H_2O}/p_{H_2} on the Rate

Run	NiO Wt(g)	Total Salt(g)	$\dot{n}_T$ (mol/s)	p_{H_2O}/p_{H_2}	r_{CO_x} (mol/s)	r_{CO_x}/p_{CH_4} (mol C/s/atm)	$\left(r_{CO_x}\right)_{Ni}/(p_{CH_4} w_{NiO})$ (mol C/(s·atm·gNiO))
36.T1(1)	.38	13.3	16.6×10^{-5}	14.3	53.0×10^{-8}	63.2×10^{-8}	0×10^{-8}
36.T1(2)	.38	13.3	24.9 "	168.0	23.7 "	42.2 "	0 "
36.T1(3)	.38	13.3	15.7 "	2.26	53.7 "	218.0 "	418 "

Note: (a) At T = 1243°K, $\left(\frac{r_{CO_x}}{p_{CH_4}}\right)_{BASE} = 59.2\times10^{-8} \frac{\text{mol C}}{\text{s·atm}}$

(b) Equilibrium of (5.4.3), K_{eq} 130

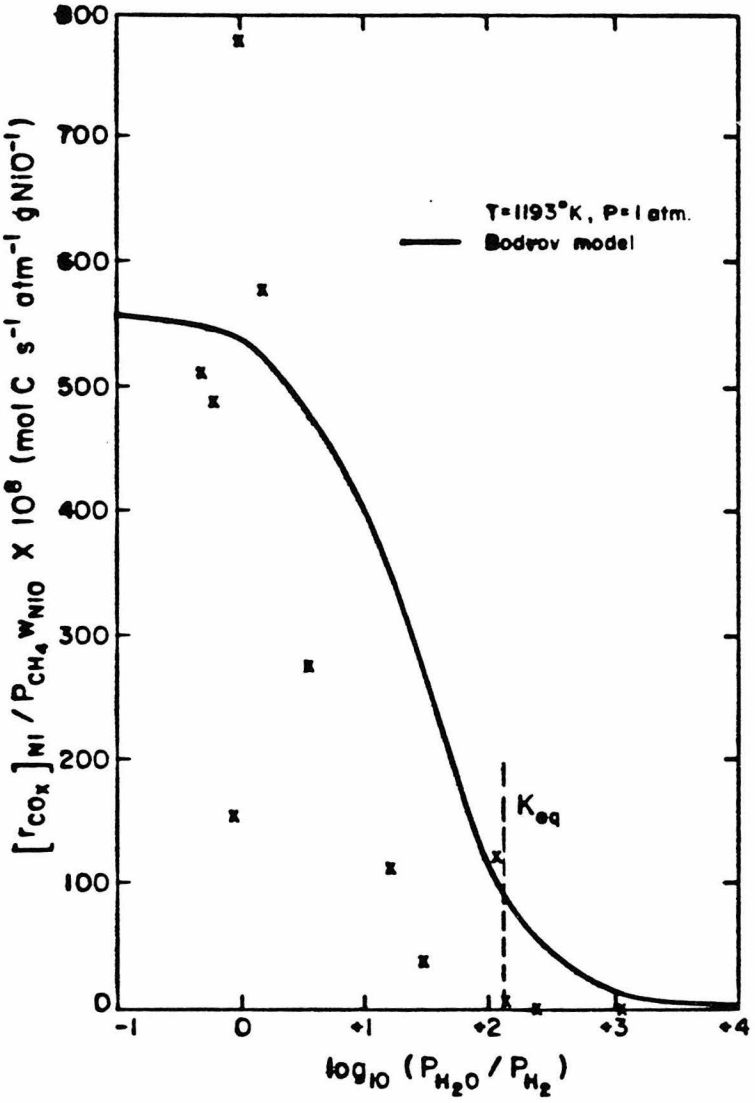

FIG. 5.4.1: CH_4 - H_2O REFORMING

SALT: Na_2O - P_2O_5 - NiO

SECTION 5.5: TEMPERATURE DEPENDENCE OF THE RATE

The data of Tables 5.4.1 through 5.4.3 were analyzed using linear regression to determine the constants k and a in the Bodrov model (Bodrov, 1964):

$$\left(\frac{r_{CO}}{W^{o}_{NiO}x}\right)_{Ni} = \frac{k\, p_{CH_4}}{1 + a\,\frac{p_{H_2O}}{p_{H_2}}} \qquad (5.5.1)$$

where k is a rate constant with units of mol C(s·atm·gNiO), and a is a coverage parameter, both dependent on T.

Table 5.5.1 presents the results of the regression. The constant k does increase with T as expected, and a is in the same range as Bodrov's data. Fig. 5.4.1 shows experimental and calculated results using the parameters of Table 5.5.1. The fit is satisfactory with a drop predicted at the critical p_{H_2O}/p_{H_2} ratio as discussed in the previous section.

The data scatter is due to differences in particle size distributions among reactors. The experimental results in Table 5.2.2 show a maximum rate at some intermediate p_{H_2O}/p_{H_2} ratio. This is also attributed to experimental error.

TABLE 5.5.1

Linear Regression on: $\left(\frac{r_{CO}}{w_{NiO}}\right)_{Ni}$ vs. $\frac{p_{H_2O}}{p_{H_2}}$ data

Bodrov Model: $\left(\frac{r_{CO}}{w_{NiO}}\right)_{Ni} = \frac{k\, p_{CH_4}}{1+a\,\frac{p_{H_2O}}{p_{H_2}}}$

$T(^{O}K)$	k $\left(\frac{\text{mol C}}{\text{s}\cdot\text{atm.}\cdot\text{gNiO}}\right)$	a
1143	128×10^{-8}	.0676
1168	356 "	.220
1193	561 "	.0389

Note: According to Bodrov (1964), a = 0.2 at $1173^{O}K$

SECTION 5.6: CONCLUSIONS

The Na_2O-P_2O_5-NiO system exhibits a catalytic activity for the CH_4-H_2O reaction considerably higher than the other salt systems tried. This activity is present at low H_2O to H_2 (or H_2O to CH_4) ratios, conditions under which the nickel is present in metallic form.

Under oxidizing conditions, the sodium metaphosphate - sodium pyrophosphate molten glass dissolves up to about 16 wt.% NiO as borne out by electron microprobe and XRD analysis. Under a reducing atmosphere, NiO is converted to Ni at the liquid-gas interface. As the amount of metal Ni increases, the rate of the CH_4-H_2O reaction increases until all of the nickel has been reduced to the metal form. Subsequent agglomeration of the metal causes a slow decline in the reaction rate. During transitions from oxidating to reducing environments, the reaction

$$2NiO + CH_4 \rightarrow 2Ni + CO_2 + 2H_2 \qquad (5.6.1)$$

contributes to the rate of CO_x production.

The equilibrium ratio p_{H_2O}/p_{H_2} for the reaction

$$NiO + H_2 \rightarrow Ni + H_2O \qquad (5.6.2)$$

determines the critical operating condition between the catalyzed and the uncatalyzed regime. At 1173^oK $(p_{H_2O}/p_{H_2})_{eq} = 141$.

The rate due to Ni is proportional to the weight of Ni in (or NiO originally added to) the reactor, if agglomeration process characteristics and reactor history are held constant.

A model of the type:

$$\frac{\left(r_{CO_x}\right)_{Ni}}{W^{o}_{NiO}} = \frac{k\, p_{CH_4}}{1+a\,\frac{p_{H_2O}}{p_{H_2}}} \qquad (5.6.3)$$

was used to fit the data satisfactorily. It predicts the drop in the rate at high p_{H_2O}/p_{H_2} values. The rate constant, k, increases with temperature as expected.

CHAPTER SIX

DETAILED ANALYSIS OF METHANE STEAM REFORMING IN A Na_2O-P_2O_5-NiO MELT

SECTION 6.0: GENERAL

The experimental results exhibit considerable scatter. Among the causes of this scatter are elutriation of carbon deposits (Section 3.4) and the slow reduction of NiO from the melt (Section 5.1). In spite of this scatter, we have been able to carry out simple calculations to interpret the experimental results.

In the following sections, an estimation of the diffusion coefficient of NiO through the melt is presented. The extent of the water-gas shift reaction in this system is discussed and related to the extent of the steam reforming reaction. The exposed nickel surface area is calculated in order to compare the rate per unit surface area to previous experimental results. Finally, the individual rate expressions for pyrolysis, $\left[-r_{CH_4}\right]_{BASE}$, and steam reforming, $\left[r_{CO_x}\right]_{BASE}$ and $\left[r_{CO_x}\right]_{Ni}$ obtained by data fitting, are used to describe the CH_4-H_2O reaction in the composite system Na_2O-P_2O_5-NiO.

SECTION 6.1: REDUCTION OF NiO FROM THE MELT. DIFFUSION VS. REACTION CONTROL

The transients in CO_x formation during changes in reactor conditions (oxidizing vs. reducing atmosphere) are examined in Section 5.1 and Appendix III. It is assumed there that the entire amount of dissolved NiO can instantaneously participate in the reactions with CH_4:

$$NiO(melt)+CH_4(g)\rightarrow CO(g)+2H_2(g)+Ni(s) \qquad (6.1.1)$$

$$2NiO(melt)+CH_4(g)\rightarrow CO_2(g)+2H_2(g)+2Ni(s) \qquad (6.1.2)$$

$$4NiO(melt)+CH_4(g)\rightarrow CO_2(g)+2H_2O(g)+4Ni(s) \qquad (6.1.3)$$

The diffusion through the melt was implicitly assumed to be fast, with the reaction at the surface being the controlling step. The only restriction applied to the reaction of NiO (melt) is that the rate constant k_{1_S} be less than k_{1_W}, the rate for NiO(s), the undissolved oxide (see equations 5.1.1, 5.1.2 and 5.1.3). Under these assumptions, the results of Run 39.T1(1), a first reduction experiment, and Run 39.T1(2), a second reduction experiment, presented in Figs. 5.1.3 and 5.1.4 respectively, were used to calculate k_{1_S} and k_{1_W}. The amounts of NiO, W^S_{NiO} and Ni, W_{Ni}, at each time interval were calculated assuming that reactions 6.1.1, 6.1.2 and 6.1.3 were taking place. Moreover, the steam reforming of methane was assumed to be taking place on the newly formed Ni at the $\left\{r_{CO_x}\right\}_{Ni}$ rate. Table 6.1.1 presents the data used and the calculated Ni amounts up to the establishment of a steady state (end of NiO reduction). The calculated amounts of Ni at steady state agree well with the added amount of NiO, W^o_{NiO}. Assuming first order

TABLE 6.1.1

(a) First reduction of an ACT Reactor Containing $Na_2O-P_2O_5-NiO$.

Run 39.T1(1) $T = 1193^{O}K$ $\dot{n}_T = 4.3 \times 10^{-5}$ mol/s

$y^{O}_{H_2O} = 0.13$ $W^{O}_{NiO} = 0.38g = 507 \times 10^{-5}$ mol NiO

$t - t_o$ (min)	CO (% of permanent gas flow)	CO_2 (% of permanent gas flow)	$(W_{Ni})_{calc.}$ (mol)
0	0.00	0.00	0
6	0.17	0.00	1.13×10^{-5}
11	0.51	0.24	7.43 "
15	0.79	0.77	21.44 "
27	1.16	1.34	96.87 "
37	0.98	1.10	151.39 "
47	0.67	0.80	187.47 "
57	0.64	0.76	214.56 "
68	0.67	0.72	241.20 "
79	0.82	0.72	256.68 "
89	1.06	0.72	278.30 "
102	1.75	0.78	307.03 "
112	3.21	0.94	332.85 "
122	4.18	0.84	374.01 "
132	4.00	0.70	408.66 "
142	3.98	0.64	428.28 "
152	4.48	0.69	448.28 "
163	4.48	0.66	471.56 "
178	4.28	0.58	487.85 "
194	4.38	0.57	497.28 "
205	4.53	0.55	502.61 "
221	4.60	0.54	509.24 "
309	4.15	0.45	522.25 "
314	4.11	0.47	522.25 "
330	3.76	0.36	522.25 "

TABLE 6.1.1(Cont.)

(b) Second Reduction of an ACT Reactor Containing $Na_2O-P_2O_5-NiO$.

Run 39.T1(2) $T = 1193^{O}K$ $\dot{n}_T = 4.3 \times 10^{-5}$ mol/s

$y^{O}_{H_2O} = 0.12$ $W^{O}_{NiO} = 0.38g = 507 \times 10^{-5}$ mol NiO

$t - t_o$ (min)	CO (%of permanent gas flow)	CO_2 (%of permanent gas flow)	$(W_{Ni})_{calc.}$ (mol)
0	0.00	0.00	0
5	4.20	0.02	23.53×10^{-5}
14	2.36	0.35	91.34 "
23	4.12	0.51	153.41 "
32	4.80	0.54	230.13 "
43	5.24	0.53	317.69 "
52	5.38	0.52	375.71 "
70	5.21	0.47	463.52 "
82	5.10	0.45	491.00 "
99	4.80	0.43	509.81 "
110	4.67	0.41	512.57 "
123	4.51	0.38	512.57 "
137	4.32	0.37	512.57 "
153	4.23	0.36	512.57 "
163	4.11	0.34	512.57 "
182	4.20	0.34	512.57 "
192	4.40	0.35	512.57 "
208	4.43	0.35	512.57 "

reactions, the rate constants were calculated to be:

$$k_{1_S} = 3.5 \times 10^{-4} \ s^{-1} \quad \text{(first reduction expt.)}$$

$$k_{1_W} = 8.5 \times 10^{-4} \ s^{-1} \quad \text{(second reduction expt.)}$$

These data support the assumption that $k_{1_W} > k_{1_S}$.

An attempt was made to calculate the diffusion coefficient, $D_{NiO\text{-}Melt}$, in order to compare it with the observed rate constant, k_{1_S}. The Nernst equation for the diffusion coefficient of electrolytes in aqueous solutions is (Welty, 1969):

$$D_{AB} = \frac{(1/n^+ + 1/n^-)\ RT}{(1/\lambda_+^o + 1/\lambda_-^o)\ F^2} \qquad (6.1.4)$$

where n^+, n^- are the ionic valences, λ_+^o, λ_-^o are the ionic conductances at infinite dilution and F is Faraday's constant. This gave an estimate of 3×10^{-5} cm^2/s for the diffusion coefficient of NiO in $(NaPO_3)_7$ (a composition approximating the molten eutectic) at 1200^oK. Even though the melt molecules are large, the temperature is high enough for D_{AB} to have the same order of magnitude as the diffusivity of aqueous electrolytes at room temperature. The correlation of Wilke and Chang (Danckwerts, 1970) was also used. $D_{NiO\text{-}Melt}$ was calculated to be 1×10^{-5} cm^2/s at 1200^oK. Neither the Nernst equation nor the Wilke-Chang correlation are appropriate for the present case, but they were used as first estimates. It is seen that D_{AB} is estimated to be of one order of magnitude less than k_{1_S}. Therefore, the diffusion of NiO through the melt is important in the reduction process.

The reduction process can be modeled by assuming that NiO

diffuses through a stagnant liquid (melt) around the rising bubbles at the surface of which it is reduced to metallic nickel. The assumption of an immobile melt is based on its high viscosity in the presence of NiO (see Section 2.1 and subsection 5.2.2). If the melt is assumed to be mobile, diffusional limitations would be less important because of surface renewal. The gaseous reactant, CH_4, is assumed to be insoluble in the melt. The diffusion of NiO in the melt is described by:

$$D \cdot \frac{\partial^2 c}{\partial x^2} = \frac{\partial c}{\partial t} \ , \ 0 \leq x \leq 1 \qquad (6.1.5)$$

where D is the diffusion coefficient of NiO in the melt and l is the thickness of the film. The boundary x = 0 corresponds to the crucible wall and x = l is the melt-gas interface. The boundary and initial conditions are:

$$c = c_o, \ 0 \leq x \leq 1, \ t = 0 \qquad (6.1.6)$$

$$D \frac{\partial c}{\partial x} = -k_s c, \qquad x = 1 \qquad (6.1.7)$$

$$c \text{ is bounded for all } t \qquad (6.1.8)$$

Condition (6.1.7) states that the reaction at the surface is first order with respect to NiO. The rate constant k_s has units of cm/s. Equation (6.1.5) with its boundary and initial conditions, (6.1.6) - (6.1.8), can be solved by the Laplace transform method. The solution is (Crank, 1956):

$$\frac{c_o - c}{c_o} = 1 - \sum_{n=1}^{\infty} \frac{2L\cos(\frac{\beta_n x}{l})\exp(\frac{-\beta_n^2 Dt}{l^2})}{(\beta_n^2 + L^2 + L)\cos\beta_n} \qquad (6.1.9)$$

where the β_n's are the positive roots of $\beta \tan \beta = L$ (6.1.10)

and $L = \frac{k_s l}{D}$ (6.1.11)

L is the dimensionless variable expressing the relative importance of reaction vs. diffusion. The total amount of NiO (melt) leaving the film as Ni(s) up to time t, $W_{Ni}(t)$, can be expressed as a fraction of W_{NiO}^{os} by:

$$\frac{W_{Ni(t)}}{W_{Ni}^{os}} = 1 - \sum_{n=1}^{\infty} \frac{2L^2 \exp(-\frac{\beta_n^2 Dt}{l^2})}{\beta_n^2(\beta_n^2 + L^2 + L)} \qquad (6.1.12)$$

The reaction rate is obtained by differentiating (6.1.12). This rate is maximum at t = 0 and gradually declines as the surface concentration of NiO drops. This behavior partly explains the first maximum in r_{CO_x} observed in Figs. 5.1.2 and 5.1.3, presenting first reduction results. The different behavior shown in a second reduction experiment, Fig. 5.1.4, must be explained by the presence of a large quantity of undissolved NiO, W_{NiO}^{ow}.

The observed first order rate incorporates the effects of diffusion of NiO through the melt and the surface reaction rate. Using a resistances-in-series argument, we obtain

$$\frac{1}{k_s} + \frac{l}{D} = \frac{a_s}{k_{l_s}} \qquad (6.1.13)$$

where a_s is the melt surface to volume ratio for an ACT reactor. For a bubble column, a_s is at most 10 cm^{-1} (Kenney, 1975). Assuming a melt film on the walls of an ACT reactor, a is calculated to be 5 cm^{-1} (see subsection 3.1.1 for reactor dimensions). Since k_{l_s} is about 3.5×10^{-4} s^{-1} at 1193°K and l is about 0.1 cm, D must be at least 7×10^{-6} cm^2/s. This is of the same order of magnitude as the estimates of D presented above. If the melt film is not assumed immobile, or if bubbling

takes place, mass transfer is faster and D must be assumed less than 7×10^{-6} cm^2/s to explain the observed behavior. According to equation (6.1.13) and the value of k_{l_s}, k_s must be at least 7×10^{-5} cm/s, independent of the rate of mass transfer.

Rostrup-Nielsen (1975) measured the rate of sintering for supported Ni catalysts. Using his data and assuming a first order process, the rate of sintering is calculated to be 2.1×10^{-7} s^{-1} at $973^{o}K$ and 3.3×10^{-7} s^{-1} at $1073^{o}K$. Extrapolating these results to $1173^{o}K$, the midpoint of the temperature range employed in our experiments, the rate of Ni sintering is estimated to be 5.3×10^{-7} s^{-1}. This is about three orders of magnitude less than the observed rate of reduction of NiO from the melt, k_{l_s}. Therefore, the assumption of slow sintering made in Section 5.1 and Appendix III is justified.

SECTION 6.2: APPROACH TO WATER-GAS SHIFT EQUILIBRIUM

6.2.1 Results

Table 6.2.1 presents water-gas shift data for methane steam reforming in ACT reactors containing Na_2O-P_2O_5-NiO. The experimental water-gas shift ratio is compared to the equilibrium constant of the reaction, $(K_p)_{w.g.s.}$, by means of the ratio β:

$$\beta = \frac{(p_{CO_2})_{exp.}(p_{H_2})_{exp.}}{(p_{CO})_{exp.}(p_{H_2O})_{exp.}} \cdot \frac{1}{(K_p)_{w.g.s.}} \qquad (6.2.1)$$

Since $\beta<1$ for all the experiments presented, the water-gas shift reaction was not at equilibrium. Another variable presented in Table 6.2.1 is the conversion $X_{s.r.}$ of the steam reforming reaction. $X_{s.r.}$ was calculated on the basis of methane converted, if $p_{CH_4}<p_{H_2O}$, and on the basis of water converted if $p_{CH_4}>p_{H_2O}$. In general, the data show that β increases with $X_{s.r.}$

6.2.2 Discussion

Methane steam reforming is accompanied by the water-gas shift reaction:

$$CO + H_2O \rightleftarrows CO_2 + H_2 \quad \Delta G^{o}_{1200^{o}K} = + 0.741 \text{ kcal/mol} \qquad (1.2.7)$$

The equilibrium constant, $(K_p)_{w.g.s}$, is about 1 in the range of 800 - 1000^{o}C. The data of Bodrov (1964) were close to equilibrium, whereas Ross (1973) observed that equilibrium was not attained. In a review of steam reforming, Van Hook (1980) proposed a correlation between methane conversion and the approach to equilibrium of the water-gas shift reaction. Fig. 6.2.1 shows the correlation and the data obtained by various

TABLE 6.2.1

WATER-GAS SHIFT IN ACT REACTORS

SALT: $Na_2O-P_2O_5-NiO$

(a) T = 1143°K $(K_P)_{w.g.s.} = 0.87$

Run	$\dot{n}_T$(mol/s)	$\frac{p_{CO_2} p_{H_2}}{p_{CO} p_{H_2O}}$	β	$X_{s.r.}$(%)
38.T1(4)	11.9×10^{-5}	0.00	0	0.1
38.T1(5)	6.8 "	0.00	0	0.1
38.T1(6)	8.6 "	0.00	0	0.4
38.T1(7)	4.6 "	0.00	0	1.4
38.T1(8)	4.0 "	0.11	0.13	24.3
38.T1(9)	7.8 "	0.11	0.13	20.2
38.T1(10)	7.8 "	0.03	0.03	13.7

(b) T = 1168°K $(K_P)_{w.g.s.} = 0.81$

Run	$\dot{n}_T$(mol/s)	$\frac{p_{CO_2} p_{H_2}}{p_{CO} p_{H_2O}}$	β	$X_{s.r.}$(%)
38.T2(1)	8.2×10^{-5}	0.00	0	0.3
38.T2(2)	15.7 "	0.00	0	0.1
38.T2(3)	11.0 "	0.00	0	0.2
38.T2(4)	7.6 "	0.00	0	0.2
38.T2(5)	4.5 "	0.08	0.10	24.3
38.T2(6)	8.2 "	0.06	0.07	23.5
38.T2(7)	3.8 "	0.07	0.09	50.5
38.T2(8)	7.6 "	0.07	0.09	45.9
38.T2(9)	7.4 "	0.34	0.42	63.8
38.T2(10)	9.5 "	0.04	0.05	26.6
38.T2(11)	7.6 "	0.13	0.16	48.0
38.T2(12)	15.3 "	0.08	0.10	17.6

TABLE 6.2.1 (Cont.)

(c) $T = 1193^{o}K$ $(K_P)_{w.g.s.} = 0.73$

Run	$\dot{n}_T$(mol/s)	$\frac{p_{CO_2} p_{H_2}}{p_{CO}\ p_{H_2O}}$	β	$X_{s.r.}$(%)
37.T(1)	6.3×10^{-5}	0.01	0.01	0.8
37.T(2)	16.1 "	0.00	0	0.1
37.T(3)	8.8 "	0.00	0	0.3
37.T(4)	4.7 "	0.08	0.11	23.7
37.T(5)	3.8 "	0.53	0.71	52.8
37.T(6)	5.0 "	0.06	0.08	13.9
37.T(7)	4.1 "	0.11	0.15	20.2
39.T(1)	4.2 "	0.16	0.21	32.1
39.T(2)	4.2 "	0.18	0.24	36.6

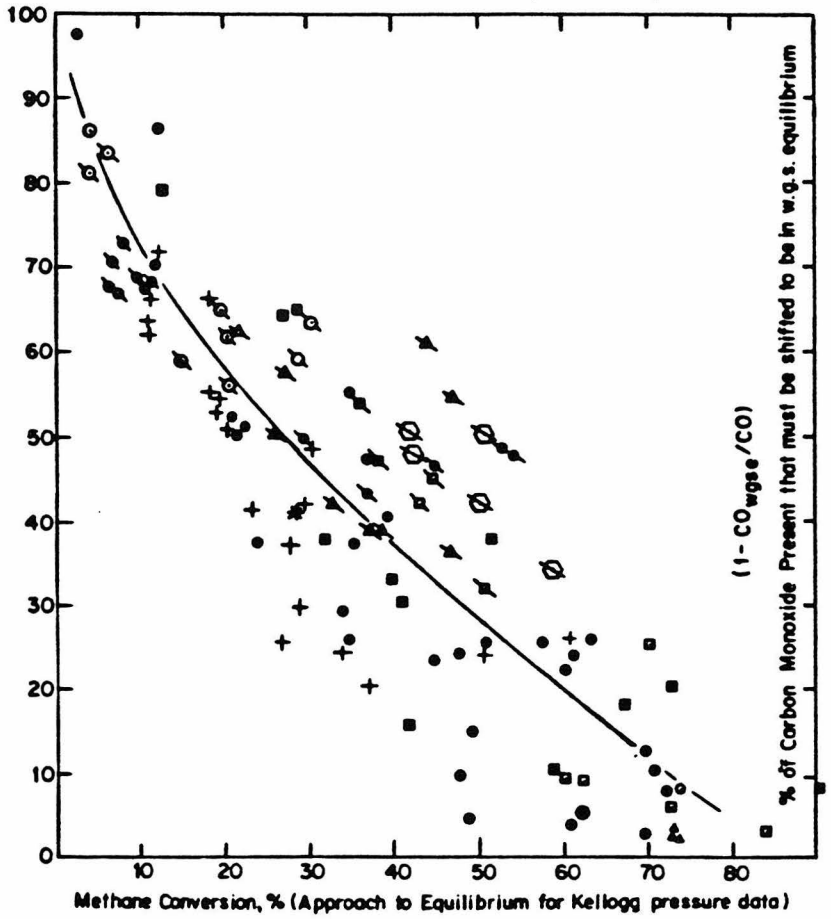

FIG. 6.2.1: WATER-GAS SHIFT CONVERSION VS. METHANE CONVERSION (Van Hook, 1980)

investigators. The proposed relation is reasonable, implying that at long residence times (high CH_4 conversion), the approach to shift equilibrium is also closer. The data scatter about the correlation curve a great deal because of the great variety of experimental conditions and catalysts used. The variable used by Van Hook to indicate approach to water-gas shift equilibrium is $1-CO_{w.g.s.e.}/CO$, or % of carbon monoxide present that must be shifted to be in w.g.s. equilibrium. This variable is equivalent to:

$$1 - CO_{w.g.s.e.}/CO = 1 - \frac{(K_{w.g.s.})_{exp.}}{(K_p)_{w.g.s.}} = 1 - \beta \qquad (6.2.2)$$

$$\text{where } (K_{w.g.s.})_{exp.} = \frac{(p_{CO_2})_{exp.}(p_{H_2})_{exp.}}{(p_{CO})_{exp.}(p_{H_2O})_{exp.}} \qquad (6.2.3)$$

The data of Table 6.2.1 follow the direction of the correlation presented in Fig. 6.2.1 but generally lie above the curve. Evidently, the environment of molten $Na_2O-P_2O_5-NiO$ is less active for water-gas shift than other methane steam reforming catalytic systems. The water-gas shift reaction is catalyzed by Fe_2O_3, thorium oxide (Nebergall, 1968), Cu-Zn, or Co-Mo-alkali metal catalysts (Newsome, 1980). In the present system, Fe_2O_3 is contained in mullite MV-30 to an extent of 0.500 wt. % (see Table 3.1.2). This oxide was present as a solid in the walls of ACT reactors and was also dissolved in the melt (see Fig. 5.2.9).

SECTION 6.3: COMPARISON OF RATE WITH PREVIOUS WORK

Most previous investigations of methane steam reforming were conducted at lower temperatures. The methane reforming reaction becomes thermodynamically favorable ($K_p \geq 1$) at about 620°C (JANAF, 1971). Therefore, if a high surface area catalyst is available, high CH_4 conversions can be obtained at relatively low temperatures. As a result, most previous experimental work has been performed at temperatures between 600° and 800°C (Akers, 1955; Bodrov, 1968; Likins, 1970; Ross, 1973). However, some studies have been performed with Ni foil in the temperature range 800° to 1000°C, the same as the one used in the present study (Fujimoto, 1933; Bodrov, 1964).

Bodrov (1964) reported a rate constant on Ni foil of 533×10^{-8} mol $CH_4/(s \cdot atm\ CH_4 \cdot cm^2 Ni)$ at 1173°K. The activation energy was calculated to be E = 31 kcal/mol. In order to compare this rate constant to the k values (mol $CH_4/(s \cdot atm\ CH_4 \cdot gNiO)$ presented in Table 5.5.1, the surface to volume ratio of the Ni suspended in the melt has to be estimated.

It can be shown that for a catalyst suspended in a bubbling liquid the catalyst surfact to melt volume ratio is independent of catalyst particle size. It depends only on the volume fraction of the melt occupied by the catalyst and on the surface to volume ratio of the bubble column. Let f_v be the volume fraction occupied by the catalyst in a melt of volume V. If the melt volume is intersected by a surface, let the fraction of this surface occupied by catalyst be f_s. Allowing many such

parallel surfaces to intersect the melt, we can compute the volume of catalyst in the melt by:

$$V_{catalyst} = \lim_{(\Delta l)_i \to 0} \sum_i (f_s)_i A_i (\Delta l)_i \qquad (6.3.1)$$

where $(f_s)_i$ is the catalyst surface fraction of surface i, A_i is the area of surface i in the melt and $(\Delta l)_i$ is the distance between two adjacent surfaces i and i + 1. Equation (6.3.1) assumes plane surfaces. This is not a necessary assumption; the rule to be proved is valid for any surface. In any case, for particles which are small in comparison to the radius of curvature of the surface, the surface can be considered to be plane. Defining an average catalyst surface fraction, $(f_s)_{avg.}$, by:

$$(f_s)_{avg.} = \frac{\lim_{(\Delta l)_i \to 0} \sum_i (f_s)_i A_i (\Delta l)_i}{\lim_{(\Delta l)_i \to 0} \sum_i A_i (\Delta l)_i} \qquad (6.3.2)$$

Equation (6.3.1) can be written as:

$$V_{catalyst} = (f_s)_{avg.} \cdot \lim_{(\Delta l)_i \to 0} \sum_i A_i (\Delta l)_i \qquad (6.3.3)$$

or

$$V_{catalyst} = (f_s)_{avg.} \; V \qquad (6.3.4)$$

$$(f_s)_{avg.} = \frac{V_{catalyst}}{V} = f_v \qquad (6.3.5)$$

Therefore, the average catalyst surface fraction is equal to the catalyst volume fraction. This can be applied to the bubble surfaces, assuming that the catalyst does not aggregate at the bubble surface preferentially, or, equivalently, that the catalyst is sufficiently wetted by the melt (see subsection 5.2.3). If a_s is the surface to volume ratio of the bubble column, the exposed catalyst surface is approximately:

$$A_{catalyst} \simeq (a_s V) f_V = a_s V_{catalyst} \qquad (6.3.6)$$

If ρ_c is the catalyst particle density, then:

$$\frac{A_{catalyst}}{W_{catalyst}} \simeq \frac{a_s V_{catalyst}}{\rho_c V_{catalyst}} = \frac{a_s}{\rho_c} \qquad (6.3.7)$$

Since the catalyst particles have a finite volume, their exposed area inside the bubble is larger than the area of intersection with the bubble surface by a certain factor. For spherical particles of radius r, which is small in comparison to bubble size, this factor is:

$$\frac{\text{avg. exposed area}}{\text{avg. area of intersection}} = \frac{\frac{1}{2}(4\pi r^2)}{2/3\ \pi r^2} = 3 \qquad (6.3.8)$$

For particles of other shapes, this factor is different from 3. If the contact angle between melt and catalyst particles is θ then this factor is $2/(1+\cos\theta)$. Using (6.3.7), (6.3.8) becomes:

$$\frac{A_{catalyst}}{W_{catalyst}} \simeq \frac{3a_s}{\rho_c} \qquad (6.3.9)$$

It was assumed that the Ni particles originating from NiO reduction were approximately spherical. For the bubble column, a_s was taken as 5 cm^{-1} as in Section 6.1. Hence,

$$\frac{\text{Exposed Ni area}}{\text{Total Ni wt.}} = 1.68\ cm^2/gNi \qquad (6.3.10)$$

Using this conversion factor, the rate constant per unit surface area was calculated from the values of Table 5.5.1. The values for this specific rate constant are presented in Table 6.3.1, along with values calculated from Bodrov's data (1964). The two sets of results are of the same order of magnitude. It should be noted that the activity of Ni catalysts is very much affected by the history of the catalyst, leading to uncertainties in the prediction of the rate. Freshly reduced catalysts

TABLE 6.3.1

Comparison of Rate with Previous Work

T (^{o}K)	k (Table 5.5.1) $\frac{\text{mol } CH_4}{s \cdot atm\ CH_4 \cdot gNiO}$	k^* $\frac{\text{mol } CH_4}{s \cdot atm\ CH_4 \cdot cm^2\ Ni}$	k^* (Bodrov, 1964) $\frac{\text{mol } CH_4}{s \cdot atm\ CH_4 \cdot cm^2 Ni}$
1143	128×10^{-8}	97×10^{-8}	376×10^{-8}
1168	356 "	269 "	504 "
1173	---	---	533 "
1193	561 "	424 "	666 "

exhibit high activity which declines with time (deactivation by coke deposits). Catalysts exposed to a high temperature and operated at a lower temperature also exhibit higher activity which declines with time (Bodrov, 1964). Supported catalysts, e.g. Ni/Al_2O_3, tend to form spinels ($NiAl_2O_4$) which are reduced to Ni more slowly than NiO is (Ross, 1973). Therefore, their activity is dependent on the length of operating time. In the present study, the catalyst was subjected to frequent oxidation/reduction cycles. Moreover, the Na_2O-P_2O_5-NiO melt is analogous to the spinel of supported catalysts and is reduced more slowly than NiO (s) (see Section 6.1). Hence, in view of the experimental scatter, the agreement between the two sets of results presented in Table 6.3.1 is considered good. Another cause of data scatter is the existence of non-spherical particles and of large Ni particles (up to a few millimeters in size; see Section 5.2) for which the derivation of surface to volume ratio for a suspended catalyst presented above is not strictly applicable.

SECTION 6.4: REACTOR MODELING

The reactions occurring during methane steam reforming in an ACT reactor, containing Na_2O-P_2O_5-NiO, at a steady state are:

(a) methane pyrolysis, rate = $\left(-r_{CH_4}\right)_{BASE}$;

(b) methane steam reforming

- on crucible walls and salt surfaces,

  rate = $\left(r_{CO_x}\right)_{BASE}$,

- on the Ni surface, rate = $\left(r_{CO_x}\right)_{Ni}$;

(c) the water-gas shift reaction.

For the pyrolysis reaction, the results presented in Tables 3.3.5, 3.3.6, and 3.3.7 can be fitted by the rate expression

$$\frac{\left(-r_{CH_4}\right)_{BASE}}{p_{CH}} = 4.66\times10^{+5}\ \exp\left(\frac{-62{,}000(cal)}{RT}\right)\frac{mol\ CH_4}{s\cdot atm CH_4} \qquad (6.4.1)$$

The rate of steam reforming in the absence of Ni, $\left(r_{CO_x}\right)_{BASE}$, is calculated from the data presented in Fig. 4.2.1 as

$$\frac{\left(r_{CO_x}\right)_{BASE}}{p_{CH_4}} = 4.65 \times 10^{+4} \exp\left(\frac{-62{,}000(cal)}{RT}\right)\frac{mol\ C}{s\cdot atm\ CH_4} \qquad (6.4.2)$$

This value of $\left(r_{CO_x}\right)_{BASE}$ takes into account in an average way the negative effect of p_{H_2O} on the rate (Section 4.2). It should be noted that $\left(r_{CO_x}\right)_{BASE}/\left(-r_{CH_4}\right)_{BASE} \simeq 0.1$, independent of T. This suggests that in the absence of Ni(s) the methane-steam reaction is carried out via the pyrolysis of CH_4 to carbonaceous matter and the subsequent reaction of this matter with steam. The factor 0.1 is close to the fraction x = 0.13 of methane cracking products that are not elutriated, presented in

Section 3.4. The carbon that is not elutriated eventually reacts with H_2O to yield carbon oxides at the $\left[r_{CO_x}\right]_{BASE}$ rate. This closes the carbon mass balance for a reactor at steady state.

An estimate of $\left[r_{CO_x}\right]_{Ni}$, the additional steam reforming rate due to Ni(s), can be obtained by using the values of the specific rate constant presented in Table 6.3.1. $\left[r_{CO_x}\right]_{Ni}$ has the form:

$$\left[r_{CO_x}\right]_{Ni} = \frac{k^* \cdot p_{CH_4} \cdot A_{Ni}}{1 + a \frac{p_{H_2O}}{p_{H_2}}} \qquad (6.4.3)$$

where A_{Ni} is the exposed Ni area (see Section 6.3).

As far as the water-gas shift reaction is concerned, its extent can be correlated with the extent of the reforming reaction in the manner proposed by Van Hook (1980) and discussed in Section 6.2.

In order to write a differential equation for the reactor, the gases are assumed to be flowing under plug flow conditions through a tube. The melt and metallic Ni are assumed to form an immobile coating on the interior of the tube. Under this assumption, the rate of steam reforming at any point along the reactor is:

$$r_{CO_x}(z) = \left[r_{CO_x}\right]_{BASE}(z) + \left[r_{CO_x}\right]_{Ni}(z) \qquad (6.4.4)$$

where z is the axial coordinate of the tubular reactor, $0 \leq z \leq L$, L being the length of the reactor. Equation (6.4.4) can be written as:

$$v_{avg.}\frac{dp_{CH_4}(z)}{dz} = -p_{CH_4}(z)\cdot 4.65\times10^4\cdot\exp\left(\frac{-62,000}{RT}\right) - \frac{\overset{*}{k}(T)\cdot p_{CH_4}(z)\cdot A_{Ni}}{1 + a\,\frac{p_{H_2O}(z)}{p_{H_2}(z)}} \qquad (6.4.5)$$

where $v_{avg.}$ is the average linear gas velocity through the reactor and $p_{H_2O}(z)$ and $p_{H_2}(z)$ are related to $p_{CH_4}(z)$ stoichiometrically. Equation (6.4.5) can be integrated analytically to provide the methane conversion at any point z along the reactor. The major contribution to the overall rate comes from the second term at the right. At low values of p_{H_2}, this term increases with conversion exhibiting an autocatalytic effect.

Commercial methane steam reformers operate at high steam to carbon ratios (10 to 20) and high conversions. Close to the reactor inlet the p_{H_2O}/p_{H_2} ratio is greater than the equilibrium constant of the NiO-H_2 reduction, reaction (5.6.2). However, as H_2 is being produced by the uncatalyzed CH_4-H_2O reaction, eventually p_{H_2O}/p_{H_2} becomes less than the equilibrium constant. Since $(p_{H_2O}/p_{H_2})_{eq.}$ of reaction (5.6.2) is about 100-200 for T = 600-1000°C, this change occurs at low methane conversions. The conversion at the change-over point is about:

$$\frac{H_2 \times 1/3}{CH_4} = \frac{(\text{Steam} \times 1/100)}{\text{Methane}} \times 1/3 = (S\div C)\times(0.33)\% \qquad (6.4.6)$$

where (S÷C) is the steam to carbon ratio. Since the reaction is carried out commercially to high conversion (∿90%), the high steam to carbon ratio is not an obstacle to the attainment of this conversion. High steam to carbon ratios are employed to prevent coke deposition on the catalyst.

CHAPTER SEVEN

CONCLUSION

SECTION 7.1: SUMMARY OF RESULTS AND DISCUSSION

This study examined the pyrolysis of methane and the reaction of methane with steam in ceramic reactors in the absence and presence of the molten salt mixtures $Na_2O-P_2O_5$, $K_2O-P_2O_5$, $Na_2O-P_2O_5-V_2O_5$ and $Na_2O-P_2O_5$-NiO.

The pyrolysis reaction was found to be unaffected by the presence of any of the salt systems. The observed reaction rate is about the same as that predicted for homogeneous pyrolysis (see Fig. 3.3.2). The observed activation energy was 62 kcal, less than the activation energy of the homogeneous reaction of 79 kcal (Kassel, 1932; Steacie, 1954). This could indicate a compensation effect in the calculation of E_A and the frequency factor, or more probably, initiation of the reaction on a surface, that of the ceramic or the molten salt. The major product of CH_4 pyrolysis is H_2. Other products are C_2H_2, C_2H_4, other unsaturated hydrocarbons, tars and coke. It was found (see Section 3.4) that about 87% (=1-x) of the carbon in the pyrolysis products is immediately carried out of the reactor by the gas. The rest forms a carbon inventory which in turn is elutriated at a rate of about $2.2 \times 10^{-4} s^{-1} (=k_e)$. A steady state carbon inventory is thus established by the balance of carbon formation and elutriation. The rate of CH_4 pyrolysis, calculated from the data, is:

$$\frac{\left(-r_{CH_4}\right)_{BASE}}{p_{CH_4}} = 4.66 \times 10^5 \exp\left(\frac{-62{,}000}{RT}\right) \frac{\text{mol } CH_4}{s \cdot \text{atm } CH_4} \qquad (7.1.1)$$

The rate of the steam-methane reaction in blank mullite

reactors is not significantly different from that in reactors containing $Na_2O-P_2O_5$, $K_2O-P_2O_5$, $Na_2O-P_2O_5-V_2O_5$, or $Na_2O-P_2O_5$-NiO (the last under oxidizing conditions). The rate is calculated to be:

$$\frac{\left(r_{CO_x}\right)_{BASE}}{p_{CH_4}} = 4.65 \times 10^4 \exp\left(\frac{-62,000}{RT}\right) \frac{\text{mol C}}{\text{s}\cdot\text{atm } CH_4} \qquad (7.1.2)$$

The ratio $\left(r_{CO_x}\right)_{BASE}/\left(-r_{CH_4}\right)_{BASE}$ is approximately 0.1, independent of temperature. The $\left(r_{CO_x}\right)_{BASE}/\left(-r_{CH_4}\right)_{BASE}$ ratio is close to the retention (non-elutriation) factor x ($\simeq$0.13), which suggests that the CH_4-H_2O reaction does not proceed directly but via the pyrolysis of methane and the subsequent reaction of the coke formed.

Under reducing conditions, the NiO dissolved in the $Na_2O-P_2O_5$ melt is reduced to Ni(s) and this metallic nickel catalyzes the methane steam reforming reaction. The rate due to Ni can be described by the Bodrov (1964) model:

$$\left(r_{CO_x}\right)_{Ni} = \frac{\overset{*}{k}\cdot p_{CH_4}\cdot A_{Ni}}{1 + a\,\frac{p_{H_2O}}{p_{H_2}}} \qquad (7.1.3)$$

The values of $\overset{*}{k}$, A_{Ni} and a are presented in Sections 5.5 and 6.3. The exposed Ni area, A_{Ni}, is approximately proportional to the weight of Ni in the reactor. Electron microscope and electron microprobe analysis studies (subsection 5.2.3) suggest that metallic Ni is wetted by the melt, so that the Ni particles are dispersed in the bulk of the melt. Ni is exposed to the reactants on the surface of bubbles. The exposed Ni area per unit weight of Ni is estimated to be 1.68 cm^2/g.

The transition from an oxidizing to a reducing reactor atmosphere is controlled by the equilibrium constant, $(p_{H_2O}/p_{H_2})eq.$, of the reaction:

$$NiO + H_2 \rightarrow Ni + H_2O \qquad (7.1.4)$$

which is in the range of 100 to 200 for T = 600-1000°C. If the feed to the reactor consists of CH_4 and H_2O alone, the part of the reactor close to the inlet will contain NiO. H_2 is produced by the uncatalyzed CH_4-H_2O reaction and, eventually, p_{H_2O}/p_{H_2} becomes less than $(p_{H_2O}/p_{H_2})eq$. From that point on, nickel exists as Ni(s) and methane steam reforming is carried out at the high $\left(r_{CO_x}\right)_{Ni}$ rate. If a small amount of H_2 or products are recycled, reducing conditions will prevail throughout the reactor.

SECTION 7.2: STEAM REFORMING APPLICATIONS OF NICKEL-CONTAINING MOLTEN SALT SYSTEMS

Conventional reforming catalysts are composed of Ni dispersed on a porous support, e.g. Ni/Al_2O_3, Ni/MgO, $Ni/MgAl_2O_4$, etc. Sometimes, alkali or alkaline earth compounds are included in the formulation to minimize coking. Noble metals such as Pt, Pd, Ru, Rh are also used in place of Ni (Rostrup-Nielsen, 1975). As was seen in Section 1.3, such catalysts are not very well adapted to heavy crude and residual oil feeds. The heavy metal (Ni and V) and sulfur content of these feeds shortens catalyst life and makes regeneration difficult.

A reactor containing metallic Ni suspended in a molten salt can be used in steam reforming as was demonstrated in the present study. In the molten salt environment, nickel exhibits the same catalytic activity as Ni foil (see Section 6.3). An alkali containing melt controls coking in the same manner as the alkaline promoters of solid catalysts. An obvious disadvantage of this system is the low surface to weight ratio of nickel. This ratio is about 1.68 cm^2/g for this system vs. 45 cm^2/g for a Ni foil 0.05 mm thick and 10 m^2/g for supported nickel catalysts (Rostrup-Nielsen, 1975). Other disadvantages of this system are corrosion and handling problems associated with molten salts. Therefore, a molten-salt-suspended Ni catalyst is not recommended to steam reform light hydrocarbons. In the case of residual oil, however, this novel steam reforming system deserves further consideration.

The Ni and V content of residual oil should not affect system performance. Nickel derived from the feed will behave just as nickel added to the reactor as a catalyst. During the process of redissolution (oxidation to NiO and dissolution by the melt) all nickel will become indistinguishable as to origin. Vanadium will follow the same cycle of oxidation and reduction as nickel. Sulfur will be captured by the melt in the form of sulfides; some H_2S adsorption on Ni will also occur. An equilibrium of the type

$$S^{=}\ (melt) \rightleftarrows H_2S/Ni(s) \rightleftarrows H_2S(g) \qquad (7.2.1)$$

will be established. If the melt and the catalyst have to be regenerated, sulfur can be removed as H_2S or SO_2. Vanadium can be removed by selective precipitation from a bleed stream. Regeneration can be applied at fixed time intervals or by continuous removal and treatment of melt and catalyst in other vessels. The sequence of oxidation and reduction subjects nickel to dissolution into and precipitation from the melt. In this way, the Ni(s) surface remains relatively uncontaminated by coke, sulfur and vanadium.

SECTION 7.3: RECOMMENDATIONS FOR FUTURE WORK

Steam reforming reactions can be carried out in the catalytic system presented here. Its advantageous use is seen to be in the steam reforming of residual oil and heavy crude fractions. Therefore, this application of the system should be demonstrated first.

Residual oil steam reforming runs should be performed to establish the catalytic activity of Ni suspended in a molten salt under these conditions. The rate of steam reforming and evolution of sulfur compounds should be observed as a function of time to detect any poisoning of Ni by S and the heavy metals present in crude. Regeneration should consist of a flow of steam or H_2 and H_2O to promote H_2S desorption. Air flow could also be used to complete carbon burn-off. The formation of alloys of Ni with V or other metals contained in the oil and their effect on activity should be investigated. Electron microprobe analysis can determine the distribution of V in the melt and in the Ni particles.

The catalytic activity of different salts on the steam carbon reaction during steam reforming can be determined by mode (b) experiments (Section 3.2). The results can be interpreted using the analysis presented in Section 3.4 for elutriation. In this case, the carbon inventory is increased by coking and diminished by elutriation (rate constant k_e, s^{-1}) and, additionally, by the steam carbon reaction (rate constant k_2, s^{-1}).

Finally, an economic study is necessary to determine the costs and benefits of this system. The higher cost of solid supported catalysts should be weighed against the cost of molten salt operation.

REFERENCES

REFERENCES

Akers, W.W., Camp, D.P., AIChE J., 1, 471 (1955).

Birks, L.S., Electron Probe Microanalysis, Interscience, New York, 1971.

Blayden, H.E., Riley, H.L., Shaw, F., Fuel,22, 64 (1943).

Bodrov, N.M., Apel'baum, L.O., Temkin, M.I., "Kinetics of the Reaction of Methane with Steam on the Surface of Nickel", Kinetika i Kataliz, 5 (4), pp. 696-705, July-August (1964).

Bodrov, I.M., Apel'baum, L.D., Temkin, M.I., Kinetika i Kataliz, 9, 877 (1968).

Cover, A.E., Schreiner, W.C., Skaperdas, G.T., "Kellogg's Coal Gasification Process", CEP 69, 31 (1973).

Crank, J., The Mathematics of Diffusion, Oxford University Press, London, 1956.

Danckwerts, P.V., Gas-Liquid Reactions, McGraw-Hill, New York, 1970.

Duecker, W.W., West, J.R., "Manufacture of Sulfuric Acid", Am. Chem. Soc. Monograph Series No. 144, Reinhold, New York, 1959.

Dugan, J.J., Higgins, J.P., "Hydrocarbon Cracking in a Regenerable Salt Medium Bath", U.S. Pat. 3,852,188, December(1974)

Eakman, J.M., Wesselhoft, R.D., Dunkleman, J.J., Vadovic, C.J., "Gasifier Operation and Modeling in the Exxon Catalytic Coal Gasification Process", Coal Processing Technology, 6 , CEP Technical Manual, p. 146. AIChE (1980).

Electric Power Research Institute, "Evaluation of Coal Conversion Processes to Provide Clean Fuels," EPRI 206-0-0, October, 1974.

Electric Power Research Institute, "Assessment of Fuel Processing Alternatives for Fuel Cell Power Generation", EPRI 919-1, September, 1977.

Fujimoto, H., J. Soc. Chem. Ind. Jpn., Suppl.,36, 147-148 (1933).

Green, C.R., Biasca, F.E., Pell, M., Struck, R.T., Zielke, C.W., "Gasoline from Coal via Molten Zinc Chloride Hydrocracking", Coal Processing Technology, 6, CEP Technical Manual, p. 102. AIChE (1980).

Haraguchi, T., Nakashio, F., Sakai, W., "Kinetics of the Pyrolysis of Propane-Propylene Mixtures", in "Industrial and Laboratory Pyrolyses", ACS Symposium Series No. 32, p. 99. American Chemical Society, Washington, D.C. (1976).

Harbison-Walker, "The Handbook of Castable Refractories", p. 23, Bulletin 5M-REV877, Harbison-Walker Refractories, Dresser Industries, Pittsburgh, PA, 1977.

Hering, S.V., Flagan, R.C., Friedlander, S.K., "Design and Evaluation of New Low-Pressure Impactor. I", Env. Sci. and Tech., 12, 667 (1978).

Hering, S.V., Flagan, R.C., Friedlander, S.K., "Design and Evaluation of New Low-Pressure Impactor. II", Env. Sci. and Tech., 13, 184 (1979).

"JANAF Thermochemical Tables", 2nd Ed., NSRDS-NBS 37, 1971.

Johnson, J.L., "The Use of Catalysts in Coal Gasification," Catal. Rev, 14, 131 (1976).

Kaffes, N.A., Ph.D. Candidacy Report, p. 9. Chem. Eng. Dept., CIT, Pasadena, CA, 1977.

Kassel, L.S., J. Am. Chem. Soc., 54, 3949 (1932).

Kenney, C.N., "Molten Salt Catalysis of Gas Reactions", Catal. Rev. 11, 197 (1975).

Kohl, A.L., Slater, M.H., Miller, K.J., "Status of the Molten Salt Coal Gasification Process". Presented at GRI/AGA/DOE/ IGU 10th Synthetic Pipeline Gas Symposium, Chicago, IL. October 30, 1978.

Kohl, A.L., Slater, M.H., Hsia, P.R., "Operation of the Molten Salt Coal Gasification Process Development Unit". Paper presented at the 7th Energy Technology Conference and Exposition, Washington, D.C., March, 1980.

Le Francois, P.A., Barclay, K.M., Skaperdas, G.T., "Bench Scale Studies of the Kellogg Coal Gasification Process", ACS Advances in Chemistry Series No. 69, 1967.

Likins, M.R., Jr., Ph.D. Thesis, University of Louisville, 1970.

Mah, A.D., Pankratz, L.B., "Contributions to the Data on Theoretical Metallurgy. XVI. Thermodynamic Properties of Nickel and its Inorganic Compounds", U.S. Bureau of Mines, NTIS Bulletin 668, PB-252 194, 1976.

McClune, W.F., Managing Ed., Powder Diffraction File, Alphabetical Index, Inorganic Compounds, 1978, Publication SMA-28. JCPDS, International Center for Diffraction Data, Swarthmore, PA, 1978.

McDanel Refractory Company, "McDanel Mullite and Alumina Tubes," Catalog effective 5/1/79. McDanel Refractory Company, Beaver Falls, PA, 1979.

McKee, D.W., Chatterji, D., Carbon,16 (1), 53 (1978).

McKee, D.W., "The Catalyzed Gasification Reactions of Carbon", Chem. and Phys. of Carbon, 16, 1 (1981).

Nahas, N.C., Gallagher, J.E. Jr., "Catalytic Gasification Predevelopment Research". Presented at the 13th Intersociety Energy Conversion Engng. Conference, August, 1978.

Nebergall, W.H., Schmidt, F.C., Holtzclaw, H.F. Jr., College Chemistry with Qualitative Analysis, 3rd Ed., Heath, Lexington, MA, 1968.

Newsome, D.S., "The Water-Gas Shift Reaction", Catal. Rev.-Sci. Eng., 21 (2), 275-318 (1980).

Ross, J.R.H., Steel, M.C.F., "Mechanism of the Steam Reforming of Methane Over a Coprecipitated Nickel-Alumina Catalyst", J. Chem. Soc. Faraday Trans. 1,69, 10 (1973).

Rostrup-Nielsen, J.R., Steam Reforming Catalysts . Danish Technical Press, Copenhagen, Denmark, 1975.

Steacie, E.W.R., "Atomic and Free Radical Reactions", ACS Monograph Series No. 125, v. 1, p. 128. Reinhold, New York, (1954).

Taylor, H.S., Neville, H.A., J. Amer. Chem. Soc. 43, 2055 (1921).

Trilling, C.A., "Mass and Heat Balance for Coal Gasification by Atomics International's Molten Salt Gasification Process". ACS Fuel Chemistry Div., 173rd National Meeting, New Orleans, March, 1977. Preprint 22, 185 (1977).

Trimm, D.L., "The Formation and Removal of Coke from Nickel Catalyst", Catal. Rev.-Sci. Eng., 16 (2), 155 (1977).

Van Hook, J.P., "Methane-Steam Reforming", Catal. Rev.-Sci. Eng., 21 (1), 1-51 (1980).

Van Wazer, J.R., Phosphorus and its Compounds. Interscience, New York, 1958.

Veraa, M.J., Bell, A.T., LBL-4498, Lawrence Berkeley Laboratory, University of California, Berkeley, 1976.

Walker, P.L., Jr., Shelef, M., Anderson, M.A., "Catalysis of Carbon Gasification", Chemistry and Physics of Carbon, v. 4, (1968).

Welty, J.R., Wicks, C.E., Wilson, R.E. Fundamentals of Momentum, Heat and Mass Transfer, Wiley, New York, 1969.

Wen, W.-Y., "Mechanisms of Alkali Metal Catalysis in the Gasification of Coal, Char or Graphite", Catal. Rev.-Sci. Eng., 22 (1), 1-28 (1980).

Wilks, K., Samuels, E., Gardner, N., "The Gasification of Coal Chars". Master's Thesis of K. Wilks, Case Western Reserve University, 1974.

Willson, W.A., et al., "Alkali Carbonate and Nickel Catalysis of Coal-Steam Gasification". In "Coal Gasification", ACS Adv. in Chem. Series, 131, 203 (1974).

Yoshida, F., Akamatsu, K., Hara, N., "Apparatus for Continuously Decomposing Hydrocarbons in a Heating Medium Bath". U.S. Patent No. 3,729,297, April (1973).

OTHER REFERENCES

Astarita, G., Mass Transfer with Chemical Reaction, Elsevier, Amsterdam, 1967.

Gavalas, G. R., "Gasification of Residual Oil in Molten Phosphates", Research Proposal to Department of Energy, (1978).

Glueck, A.R., "Molten Salt Processes for Sulfur Emission Control", CEP, 69, 3, 56 (1973).

Janz, G. J., Molten Salts Handbook, Academic Press, New York, 1967.

Janz, G. J., et al., "Molten Salts, Volume 1: Electrical Conductance, Density and Viscosity Data", National Bureau of Standards, NSRDS-NBS 15, October, 1968.

Janz, G. J., Dijkhuis, C. G. M.,"Molten Salts, Volume 2: Electrochemistry, Surface Tension Data", National Bureau of Standards, NSRDS-NBS 28, August, 1969.

Lumsden, J., Thermodynamics of Molten Salt Mixtures, Academic Press, New York, 1966.

Scarrah, Warren P., "Hydrocracking Montana Coals Through the Use of Massive Quantities of Molten Salt Catalysts", Ph.D. Thesis, University of Montana, Diss. Abstr. Inter. B 1973, 34 (5), 2005 (1973).

Tien, T. Y., Hummel, F.A., "The System SiO_2-P_2O_5", J. Am. Ceram. Soc., 45, 422 (1962).

Turkdogan, E.T., Maddocks, W.R., "Phase Equilibrium Investigations of the Na_2O-P_2O_5-SiO_2 Ternary System", J. Iron Steel Inst., London, 172, 1 (1952).

Van der Hoeven, B.J.C. Chemistry of Coal Utilization, H. H. Lowry, Ed., p. 1603-1606, Wiley, New York, 1945.

APPENDICES

APPENDIX I

DISCUSSION OF THE TEMPERATURE GRADIENT IN THE REACTORS

One difficulty encountered with the experimental system was that the reactors were not isothermal. The lower section, the hottest one, was more closely isothermal with a shallow temperature gradient. The top section was much cooler and a negligible extent of reaction took place there. Fig. A1 presents a typical temperature profile for an ACT reactor. Profiles were not significantly different under pyrolysis or CH_4-H_2O reforming conditions. To reduce the data from such reactors, an effective temperature method was used. Methane pyrolysis has a high activation energy, E_A = 79kcal/mol for the homogeneous reaction (Steacie, 1954). According to Haraguchi (1976), if E_A > 30kcal, then the maximum temperature in the reactor is the effective temperature, i.e., all of the reaction can be assumed to take place at the maximum temperature. To check this for the ACT reactors, the activation energy, E_A, and the frequency factor, A, of the Arrhenius rate expression:

$$k = A \exp(-E_A/RT) \qquad (A.1.1)$$

were computed by a numerical technique using the observed temperature gradients. The reactor is divided into segments of equal length (Δl=1 in) in each of which the temperature is measured. Let Tij be the temperature of the i-th segment in the j-th experiment and let kj be the experimental value of the rate constant in the j-th experiment. Then A and E_A are determined by minimizing the quantity:

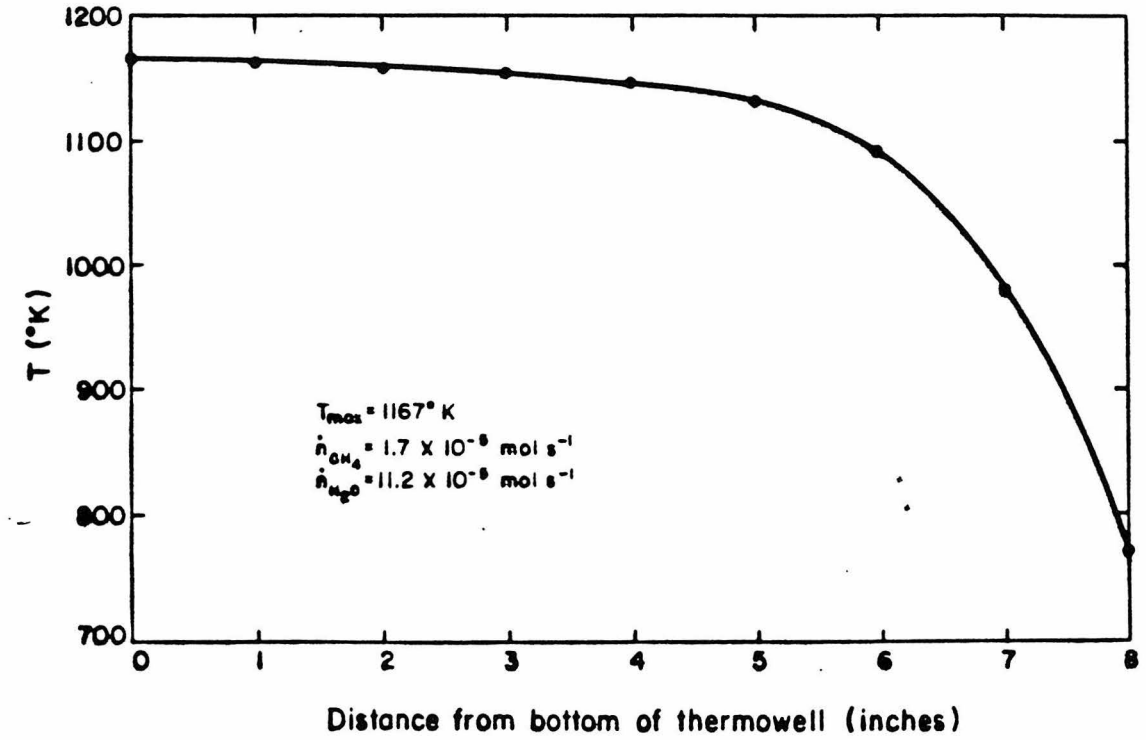

FIG. A1: TEMPERATURE PROFILE IN REACTOR ACT 5

$$J = \sum_j \left(k_j - A f_j(E_A) \right)^2 \qquad (A.1.2)$$

where

$$f_j(E_A) = (1/L) \int_0^L \exp\{- \frac{E_A}{RT_j(z)}\} \cdot \frac{T_{max}}{T_j(z)} \, dz \qquad (A.1.3)$$

L is the length of the reactor, and T_{max} is the maximum temperature in the reactor. The function $f_j(E_A)$ is evaluated numerically using the temperature profile, T_{ij}. Setting the derivative of J w.r.t. A equal to zero, it is obtained that

$$A = \frac{\sum_j k_j f_j(E_A)}{\sum_j f_j^2(E_A)} \qquad (A.1.4)$$

This expression is inserted in (A.1.2) to obtain J as a function of E_A only. The latter function is minimized with respect to E_A.

Table A1 presents the conditions of two methane pyrolysis experiments. The temperature profiles, along with the conversion to H_2 are listed. Assuming that the maximum temperature is the effective one, the activation energy is calculated to be:

$$E_{A1} = \frac{\ln(4.86/0.97) \times 1.987}{\frac{1}{1107} - \frac{1}{1167}} = 68.9 \text{ kcal/mol}$$

This estimate can be improved by correcting for the dilution of CH_4 concentration because of RT expansion:

$$E_{A_2} = \frac{\ln (4.86 \times 1167)/(0.97 \times 1107)) \times 1.987}{\frac{1}{1107} - \frac{1}{1167}} = 71.2 \text{kcal/mol}$$

Finally, the numerical procedure presented above can be used to obtain a better estimate of E_A:

$$E_{A_3} = 66.3 \text{kcal/mol}$$

TABLE A1

METHANE PYROLYSIS: EFFECT OF TEMPERATURE PROFILE

No Salt

Run	5.2	5.4
T_{max}, ^{o}K	1107	1167
$\dot{n}_{CH_4}$, mol/s	3.7×10^{-5}	3.7×10^{-5}
Inches from Bottom of Crucible		
0	$1107^{o}K$	$1167^{o}K$
1	1103	1164
2	1100	1160
3	1093	1156
4	1085	1147
5	1060	1133
6	1001	1096
7	847	981
8	629	771
H_2 at Outlet:	0.97%	4.86%

Therefore, the difference between E_{A_1}, the simplest estimate and E_{A_3}, the result of the numerical procedure is quite small, only 2.3kcal. Considering the magnitude of E_A, about 66.6kcal/mol, and the data scatter, it was decided to use the simplest method, estimating E_{A_1}, in data reduction.

APPENDIX II

ESTIMATION OF MASS TRANSFER IN THE PYROLYSIS AND STEAM REFORMING REACTIONS

If the methane pyrolysis or the steam reforming reactions were catalyzed by the salt surface or the reactor wall, the observed rate of reaction would result from two distinct steps:

(a) gas phase mass transfer of methane to the salt surface, or the reactor wall surface, and

(b) surface reaction.

The effect of mass transfer limitations on the observed kinetic data can be determined by estimating the rate of mass transfer. This rate can be estimated by assuming that methane is flowing in an annular space. This approximates the situation of methane bubbling through the salt and flowing past a liquid salt film and the reactor walls in the annular spaces. The rate of mass transfer, $r_{m.t.}$, is:

$$r_{m.t.} = k_{m.t.} \cdot A \cdot \Delta C \qquad (A.2.1)$$

where $k_{m.t.}$ = mass transfer coefficient, cm/s

A = surface area of reactor walls, cm^2

ΔC = driving force for mass transfer to the wall, mol/cm^3

For Run 2.7 (Table 3.3.6) the following data were obtained:

temperature: $1256^{o}K$

total pressure: 1.1 atm.

total flow rate: 9.0×10^{-5} mol/s

reactor wall area: 205 cm^2

concentration of feed methane: 9.63×10^{-6} mol/cm^3

rate of methane pyrolysis: 782.3×10^{-8} mol/s

To determine which correlation to use for the estimation of $k_{m.t.}$, the Reynolds number, Re, is needed. Using the equivalent hydraulic radius of the annulus, $R_{eq} = R_o - R_i$, Re is found to be 1.45, well inside the laminar range. Using the Chilton-Colburn analogy (Welty, 1969):

$$j_H = j_D \qquad \text{(A.2.2)}$$

$$\text{or } \frac{h}{\rho v_{avg} c_p} Pr^{2/3} = \frac{k_{m.t.}}{v_{avg.}} Sc^{2/3} \qquad \text{(A.2.3)}$$

For the heat transfer coefficient, h, in laminar flows, the Seider and Tate correlation is applicable:

$$\frac{h\ Deq}{k_{cond}} = 1.86(Re.\ Pr.\ \frac{Deq}{L})^{1/3} (\frac{\mu_b}{\mu_w})^{0.14} \qquad \text{(A.2.4)}$$

This way, $k_{m.t.}$ is calculated to be 6.79cm/s. If there were mass transfer limitations, the concentration of methane at the wall would be negligible. Then, $r_{m.t.}$ is:

$r_{m.t.} = (6.79 cm/s)(205 cm^2)(9.63 \times 10^{-6} mol/cm^3)$

$r_{m.t.} = 1.34 \times 10^{-2}$ mol/s

Therefore, $r_{m.t.} >> r = 782.3 \times 10^{-8}$ mol/s (observed fate of methane pyrolysis), and mass transfer is not limiting.

The above discussion is not concerned with mass transfer inside the bubbles. However, there the recirculating gas flow pattern would enhance mass transfer even more.

APPENDIX III

FURTHER DISCUSSION OF TRANSIENTS IN THE RATE OF CO_x FORMATION

The rate of carbon oxide formation as a function of time, in a reactor containing Na_2O-P_2O_5-NiO, is, according to equation (5.1.8):

$$\left[r_{CO_x}\right] = r_{CO_x\ BASE} + k_{Ni}p_{CH_4}\left[W_{NiO}^{os} + W_{NiO}^{ow}\right]\frac{MW(Ni)}{MW(NiO)} +$$
$$+ W_{NiO}^{os}\left[k_{1s} - k_{Ni}\frac{MW(Ni)}{MW(NiO)}\right]\exp\left[-\nu k_{1s}p_{CH_4}t\right] +$$
$$+ W_{NiO}^{ow}\left[k_{1w} - k_{Ni}\frac{MW(Ni)}{MW(NiO)}\right]\exp\left[-\nu k_{1w}p_{CH_4}t\right]$$

Therefore, depending on the values of the different parameters, the mode of approach to the steady-state can be:

(a) constant increase to the steady-state value;

(b) constant decline to the steady-state value;

(c) a local extremum in the rate.

The slow decline in the rate because of agglomeration is not dealt with here because it is a much slower process.

Examining the transient term:

$$r_{CO_x}(t)_{transient} = W_{NiO}^{os}\left[k_{1s} - k_{Ni}\frac{MW(Ni)}{MW(NiO)}\right]\exp\left[-\nu k_{1s}p_{CH_4}t\right] +$$
$$+ W_{NiO}^{ow}\left[k_{1w} - k_{Ni}\frac{MW(Ni)}{MW(NiO)}\right]\exp\left[-\nu k_{1w}p_{CH_4}t\right] \qquad (A.3.1)$$

and taking the derivative with respect to time:

$$\frac{d}{dt}\ r_{CO_x}(t)_{transient} =$$
$$= W_{NiO}^{os}\left[k_{1s} - k_{Ni}\frac{MW(Ni)}{MW(NiO)}\right]\exp(-\nu k_{1s}p_{CH_4}t)(-\nu k_{1s}p_{CH_4}) +$$
$$+ W_{NiO}^{ow}\left[k_{1w} - k_{Ni}\frac{MW(Ni)}{MW(NiO)}\right]\exp(-\nu k_{1w}p_{CH_4}t)(-\nu k_{1w}p_{CH_4}) \qquad (A.3.2)$$

For a local extremum in the rate, dr/dt = 0 and:

$$\exp\left[\nu(k_{1s}-k_{1w})p_{CH_4}t\right] = \frac{W_{NiO}^{os}}{W_{NiO}^{ow}} \cdot \frac{k_{1s}\left[k_{Ni}\frac{MW(Ni)}{MW(NiO)} - k_{1s}\right]}{k_{1w}\left[k_{1w}-k_{Ni}\frac{MW(Ni)}{MW(NiO)}\right]} \qquad (A.3.3)$$

Since the left-hand side of (A.3.3) is positive, it must be:

$$\frac{\left[k_{Ni}\frac{MW(Ni)}{MW(NiO)} - k_{1s}\right]}{\left[k_{1w}-k_{Ni}\frac{MW(Ni)}{MW(NiO)}\right]} > 0$$

or,

$$k_{Ni}\left[\frac{MW(Ni)}{MW(NiO)} - k_{1s}\right]\left[k_{1w}-k_{Ni}\frac{MW(Ni)}{MW(NiO)}\right] > 0 \qquad (A.3.4)$$

There are two possibilities:

(a) $k_{Ni}\frac{MW(Ni)}{MW(NiO)} > k_{1s}$

and $k_{1w} > k_{Ni}\frac{MW(Ni)}{MW(NiO)}$

and therefore, $k_{1w} > k_{Ni}\frac{MW(Ni)}{MW(NiO)} > k_{1s}$ (A.3.5)

or

(b) $k_{Ni}\frac{MW(Ni)}{MW(NiO)} < k_{1s}$

and $k_{1w} < k_{Ni}\frac{MW(Ni)}{MW(NiO)}$

and, therefore,

$$k_{1w} < k_{Ni}\frac{MW(Ni)}{MW(NiO)} < k_{1s} \qquad (A.3.6)$$

But, since W_{NiO}^{w} is exposed and more accessible to CH_4 than W_{NiO}^{s} which is dissolved in the melt, we must have $k_{1w} > k_{1s}$ and (A.3.5) is the applicable condition. Also, in equation (A.3.3), the condition $k_{1w} > k_{1s}$ makes the L.H.S. less than one, therefore:

$$\frac{W_{NiO}^{os}}{W_{NiO}^{ow}} \cdot \frac{k_{1s}}{k_{1w}} \cdot \frac{k_{Ni}\frac{MW(Ni)}{MW(NiO)} - k_{1s}}{k_{1w}-k_{Ni}\frac{MW(Ni)}{MW(NiO)}} < 1 \qquad (A.3.7)$$

Conditions (A.3.5) and (A.3.7) are necessary and sufficient for a local extremum in r_{CO_x} for $t > 0$.

NOMENCLATURE

NOMENCLATURE

a parameter in Bodrov model, dimensionless

a_p coke deposition kinetic constant, $(mol)^2/s$

a_s ratio of melt surface to melt volume for an ACT reactor, cm^{-1}

a_μ preexponential coefficient for viscosity, poise

$A_{catalyst}$ catalyst surface area, cm^2

A_i area of surface i in the melt, cm^2

ACT Annular Crucible and Tube reactor

c concentration, g/cm^3

c_o initial concentration, g/cm^3

(CH_4) methane concentration, mol/cm^3

CO_x carbon oxides, CO and CO_2

d density, g/cm^3

D diffusion coefficient, cm^2/s

D_{AB} diffusion coefficient of A in B, cm^2/s

$D_{NiO\text{-}Melt}$ diffusion coefficient of NiO in the melt, cm^2/s

E Arrhenius activation energy, kcal/mol

E_a apparent Arrhenius activation energy, kcal/mol

f_s catalyst surface frastion, dimensionless

$(f_s)_i$ catalyst surface fraction of surface i, dimensionless

f_v catalyst volume fraction, dimensionless

F Faraday's constant, coulombs/equivalent

k reaction rate constantin Bodrov model, mol C/(s·atm·CH_4.g NiO)

k^* reaction rate constant in Bodrov model, mol C/(s.atm CH_4. cm^2Ni)

k_e rate constant for elutriation, s^{-1}

k_m methane pyrolysis kinetic constant, cm^3/s

k_m^1 kinetic constant for homogeneous methane pyrolysis, s^{-1}

k_{Ni} rate constant of steam reforming on metallic nickel, mol C/(s.atm CH_4.g Ni)

k_s rate constant, cm/s

k_{ls} rate constant for the reduction of NiO dissolved in the melt, mol C/(s.atm CH_4.g NiO)

k_{lw} rate constant for the reduction of NiO not dissolved in the melt, mol C/(s.atm CH_4.g NiO)

K_{eq} equilibrium constantof the NiO reduction reaction by H_2, dimensionless

K_h equilibrium constant for salt hydrolysis

$(K_p)_{w.g.s.}$ equilibrium constant of the water-gas shift reaction, dimensionless

l melt film thickness, cm

L dimensionless group, $k_s l/D$

m stoichiometric coefficient, dimensionless

n stoichiometric coefficient, dimensionless

n^+, n^- ionic valences, dimensionless

n_i mass of species i, mol

$\dot{n}_i$ flowrate of species i, mol/s

$\dot{n}_{i,in}$ flowrate of species i at reactor inlet, mol/s

$\dot{n}_T$ total gas flowrate through reactor, mol/s

$\bar{p}$ degree of phosphate polymerization, dimensionless

p_i partial pressure of species i, atm

p_i^o partial pressure of species i at reactor inlet, atm

P total pressure, atm

r radius, cm

$-r_{CH_4}$ methane pyrolysis rate, mol C/s

$(-r_{CH_4})_{BASE}$ rate of methane consumption in the absense of Ni or NiO, mol C/s

r_{CO_x} rate of carbon oxide formation, mol C/s

$(r_{CO_x})_{BASE}$ rate of CO_x formation from methane-steam reforming in the absense of Ni or NiO, mol C/s

$(r_{CO_x})_{Ni}$ rate of methane steam reforming on Ni, mol C/s

R universal gas constant, cal/(mol.^oK)

R_{Ni} rate of methane-steam reforming on Ni per unit mass of added NiO, normalized for p_{CH_4}, mol C/(s.atm$^{\sim}CH_4$.g NiO)

t time, min

t_{run} time elapsed since beginning of experiment, min

t_o time at beginning of experiment, min

T absolute temperature, ^oK

$T_{S.G.}$ steam generator temperature, ^oC

V melt volume, cm^3

$V_{catalyst}$ catalyst volume, cm^3

w.g.s. water gas shift

w.g.s.e. water gas shift equilibrium

$W_{catalyst}$ catalyst weight, g

W_{Ni} amount of metallic Ni in the reactor at any time t, g

W^{s}_{NiO} amount of NiO dissolved in the melt at any time t, g

W^{os}_{NiO} amount of NiO initially in the reactor and originally dissolved in the melt, g

W^{w}_{NiO} amount of NiO in the reactor not dissolved in the melt at any time t, g

W^{ow}_{NiO} amount of NiO initially in the reactor and originally not dissolved in the melt, g

W^{o}_{NiO} amount of NiO initially in the reactor, g

x instantaneous fraction of pyrolysis carbon retained in the reactor, dimensionless

$X_{S.R.}$ extent of the methane-steam reforming reaction, dimensionless

y^{o}_{i} mole fraction of species i at reactor inlet, dimensionless

Greek letters

β extent of water-gas shift reaction, dimensionless

β_n n-th positive root of $\beta_n \tan\beta_n = L$

γ surface tension, dyne/cm

ΔG^{o}_{T} standard Gibbs free energy of reaction at temperature T, kcal/mol

ΔH^{o}_{T} standard enthalpy of reaction at temperature T, kcal/mol

$(\Delta l)_i$ distance between the adjacent surfaces i and i+1, cm

θ contact angle between melt and catalyst particles, degrees

λ^{o}_{+}, λ^{o}_{-} ionic conductances at infinite dilution, $cm^2/(ohm \cdot equivalent)$

μ viscosity, poise

ν stoichiometric constant relating changes in NiO and CO_x during the reduction of NiO by CH_4, dimensionless

ρ_c catalyst particle density, g/cm^3